# FINITE ELEMENT MODELING OF NONRECTANGULAR REINFORCED CONCRETE STRUCTURAL WALLS

by

Nihan Bilgin

B.S., Civil Engineering, Boğaziçi University, 2018

Submitted to the Institute for Graduate Studies in
Science and Engineering in partial fulfillment of
the requirements for the degree of
Master of Science

Graduate Program in Civil Engineering
Boğaziçi University
2021

# ACKNOWLEDGEMENTS

First and foremost, I would like to express my sincere gratitude to my thesis supervisor Professor Kutay Orakçal for his invaluable guidance, endless patience, and support throughout my studies. I am also very grateful for his support for my PhD applications and always answering my questions.

I would like to express my special thanks to Assistant Professor M. Fethi Güllü for helping me with my thesis and having the patience to answer my questions.

I would also like to express my thanks to Professor Serdar Soyöz and Professor Hilmi Luş for always supporting me and their valuable guidance and suggestions throughout my graduate studies at Boğaziçi University. I would like to express my gratitude to Professor Serdar Soyöz and Professor Alper İlki for participating in my thesis jury.

I am grateful to Boğaziçi University Department of Civil Engineering and Boğaziçi University Foundation (BÜVAK) for the financial support they provided through Mete A. Sözen Scholarship in Structural and Earthquake Engineering.

Lastly, none of this would be possible without the support of my parents. I am very thankful to my parents for the endless love, support, and encouragement they have given me my whole life. They always give me the courage to move on and do everything I would like to do without hesitation.

# ABSTRACT

## FINITE ELEMENT MODELING OF NONRECTANGULAR REINFORCED CONCRETE STRUCTURAL WALLS

This study employs and extends the Fixed-Angle-Strut Finite Element (FSAFE) model towards simulating the hysteretic response of the nonrectangular reinforced concrete structural walls subjected to multidirectional lateral loading. The FSAFE model, which was previously developed and validated for planar walls, is a relatively simple finite element model formulation based on a fixed crack angle modeling approach for concrete. The model also incorporates constitutive relationships for shear-aggregate interlock behavior along crack surfaces, and dowel action on reinforcing steel bars. Within the scope of this study, the FSAFE model formulation is extended to walls with nonrectangular cross-sections. As well, a new solution strategy is developed in order to enable nonlinear analysis of such walls under biaxial lateral loading conditions. Furthermore, the model is improved by incorporating reinforcement buckling behavior into its formulation. Model predictions are compared with experimental data on four densely instrumented U-shaped walls specimens available in the literature, at various global and local response levels. The U-shaped wall specimens investigated differ in terms of the loading scheme applied during testing (sweep pattern vs. diagonal), as well as the reinforcement configurations (concentrated at boundaries vs. distributed along web), axial load ratios, and reinforcement ratios. Comparison of lateral load vs. top displacement responses of the walls reveals good correlation between the analytical and experimental results. The model well-captures the lateral load capacity and lateral stiffness of the wall specimens, as well as their cyclic response characteristics including pinching behavior, stiffness degradation, and residual displacements. In terms of local deformation responses, including the contribution of flexural and shear deformations to wall top displacements and the distribution of vertical strains across wall base and along wall height, the model provides reasonable estimates for most cases.

# ÖZET

## DİKDÖRTGEN KESİTLİ OLMAYAN BETONARME PERDE DUVARLARIN SONLU ELEMANLAR YÖNTEMİYLE MODELLENMESİ

Bu çalışmada dikdörtgen kesitli olmayan betonarme perdelerin çok yönlü yatay çevrimsel yükleme altındaki davranışlarının modellenmesinde Sabit Payanda Açılı Sonlu Elemanlar (FSAFE) metodu kullanılmıştır ve bu amaç doğrultusunda FSAFE metodunda değişiklikler yapılmıştır. Daha öncesinde geliştirilmiş ve dikdörtgen kesitli perdeler için çalıştığı gösterilmiş olan FSAFE metodu, sabit çatlak açısı yaklaşımını kullanan, görece basit bir formülasyona sahip bir sonlu elemanlar yöntemidir. Bu modelde çatlaklarda agrega kenetlenmesi ve donatıda kama etkisi davranışları da göz önünde bulundurulmuştur. Bu çalışma kapsamında FSAFE formülasyonu, dikdörtgen kesitli olmayan perde duvarları da modelleyecek şekilde genişletilmiştir. Bu tür perdelerin çift yönlü yükleme altında doğrusal olmayan analizini yapabilmek için yeni bir çözüm stratejisi geliştirilmiştir. Buna ek olarak, model formülasyonu, donatı burkulmasını da kapsayacak şekilde geliştirilmiştir. Literatürde bulunan, yoğun bir şekilde ölçüm aletleriyle donatılmış dört adet U şeklinde perdenin deney sonuçları model sonuçlarıyla global ve lokal düzeylerde karşılaştırılmıştır. Bu dört U şeklinde perde duvar, yükleme şekliyle, donatı yerleşimiyle, eksenel yük oranları ve donatı oranlarıyla birbirinden farklılık göstermektedir. Bu perde duvarlar için yatay yük-deplasman karşılaştırmaları, deneysel ve analitik sonuçlar arasında iyi bir korelasyon göstermektedir. Model, perde duvarların yatay yük kapasitesini ve yataydaki rijitliklerini ve aynı zamanda daralma, rijitlik kaybı ve kalıcı deplasman gibi histeretik özelliklerini de iyi bir şekilde yakalayabilmektedir. Eğilme ve kesme deformasyonlarının perdenin tepe deplasmanına katkısı ve düşeydeki birim deformasyonların perde tabanındaki dağılımıyla perde yüksekliği boyunca dağılımlarını da kapsayan lokal deformasyonlar içinse model, çoğu durumda makul düzeyde sonuçlar vermektedir.

# TABLE OF CONTENTS

ACKNOWLEDGEMENTS ..... ii
ABSTRACT ..... iii
ÖZET ..... iv
TABLE OF CONTENTS ..... v
LIST OF FIGURES ..... vii
LIST OF TABLES ..... xii
LIST OF SYMBOLS ..... xiii
LIST OF ACRONYMS/ABBREVIATIONS ..... xviii
1. INTRODUCTION ..... 1
1. 1. General ..... 1
1. 2. Literature Review ..... 2
1.3. Objectives and Scope ..... 10
1.4. Thesis Outline ..... 11
2. CONSTITUTIVE MODEL DESCRIPTION ..... 12
2.1. Overview of Fixed Strut Angle Finite Element (FSAFE) Model ..... 12
2.2. The Fixed Strut Angle Model (FSAM) for RC Panel (Membrane) Behavior ..... 13
2.3. Material Constitutive Relationships ..... 15
2.3.1. Concrete ..... 15
2.3.2. Reinforcing Steel ..... 17
2.3.3. Compression Softening in Concrete ..... 24
2.3.4. Tension Stiffening on Concrete and Steel ..... 24
2.3.5. Biaxial Damage on Concrete ..... 26
2.4. Shear Aggregate Interlock on Crack Surfaces ..... 26
2.5. Dowel Action on Reinforcement ..... 28
2.6. Cyclic Degradation Parameters ..... 29
3. FINITE ELEMENT MODEL DESCRIPTION ..... 30
3.1. General Finite Element Model Formulation ..... 30
3.2. Body Constraints and Supports ..... 34
3.3. Nonlinear Analysis Strategy for Biaxial Loading ..... 36
4. EXPERIMENTAL VALIDATION OF THE MODEL FOR U-SHAPED WALLS . 40

4.1. Test Units ..... 40
4.2. Calibration of the Model for the Wall Specimens ..... 45
4.3. Comparison of Model Responses with Experimental Data ..... 54
4.3.1. Load versus Top Displacement Responses ..... 54
4.3.2. Flexural and Shear Deformation Components ..... 63
4.3.3. Vertical Strain Profiles Along Wall Height ..... 69
4.3.4. Vertical Strain Distribution at the Base ..... 73
5. SUMMARY AND CONCLUSION ..... 81
5.1. Summary ..... 81
5.2. Conclusions ..... 82
5.3. Recommendations for Future Studies ..... 83
REFERENCES ..... 85
APPENDIX A: COPYRIGHT PERMISSIONS FOR THE FIGURES ..... 92

# LIST OF FIGURES

Figure 1.1. Implementation of CSMM into OpenSees (Mo et al., 2008). ..... 5

Figure 1.2. Overview of CSMM for reinforced concrete (Luu et al., 2017). ..... 6

Figure 1.3. (a) Layered membrane section, (b) element global degrees of freedom (Rojas et al., 2016). ..... 7

Figure 1.4. (a) Discretization of walls with shear span ratio of 2, (b) discretization of walls with shear span ratio larger than 2 (Lu and Henry, 2017). ..... 8

Figure 1.5. FSAM: (a) strain field on a panel element, (b) concrete stresses along fixed struts, (c) shear aggregate interlock stresses along cracks, (d) uniaxial stresses in reinforcement, (e) dowel stresses in reinforcement (Kolozvari et al., 2019). ..... 10

Figure 2.1. Uncracked behavior of concrete in the FSAM (Orakcal et al., 2019). ..... 13

Figure 2.2. Behavior of concrete after the formation of first crack in FSAM (Orakcal et al., 2019). ..... 14

Figure 2.3. Behavior of concrete after formation of second crack in FSAM (Orakcal et al., 2019). ..... 15

Figure 2.4. Hysteretic parameters of the concrete model according to Chang and Mander, 1994 (Orakcal, 2004). ..... 16

Figure 2.5. Hysteretic rules for concrete according to Chang and Mander, 1994 (Orakcal, 2004). ..... 17

Figure 2.6. Constitutive model for reinforcing steel according to Menegotto and Pinto, 1973 (Orakcal, 2004). ..... 19

Figure 2.7. Schematic representation of monotonic compression envelope for the reinforcing steel model incorporating buckling. ..... 20

Figure 2.8. Hysteretic rules for the reinforcing steel constitutive model incorporating buckling..... 23

Figure 2.9. Average stress-strain relationship by Belarbi and Hsu (1994) for concrete in tension (Orakcal, 2004). ..... 25

Figure 2.10. Average stress-strain relationship by Belarbi and Hsu (1994) for reinforcing bars embedded in concrete (Orakcal, 2004)..... 25

Figure 2.11. Shear aggregate interlock on crack surfaces (Gullu, 2019)..... 28

Figure 2.12. Dowel action behavior (Gullu, 2019). ..... 28

Figure 3.1. Displacement along nodal DOFs in FSAFE model (Gullu, 2019). ..... 30

Figure 3.2. FSAFE model element: (a) forces along nodal DOF, (b) equilibrium of nodal forces and average stresses (Gullu, 2019). ..... 31

Figure 3.3. Model meshing for a U-shaped reinforced concrete wall. ..... 32

Figure 3.4. Global DOFs in a U-shaped wall. ..... 33

Figure 3.5. Numbering of the model elements. ..... 33

Figure 3.6. U-shaped wall after assigning body constraints: (a) side view, (b) top view. ... 36

Figure 3.7. The iterative nonlinear analysis solution strategy. ..... 39

Figure 4.1. Cross-sections of the walls and reinforcement layout: (a) TUA, (b) TUB (Beyer et al., 2008)..... 41

Figure 4.2. Test setup (Beyer et al., 2008). ..... 41

Figure 4.3. (a) Name of the wall sections, (b) target top displacement (Beyer et al., 2008). ..... 42

Figure 4.4. Instrumentation of TUA and TUB (Beyer et al., 2008). ..... 42

Figure 4.5. TUC and TUD: (a) cross-section and reinforcement layout, (b) elevation (Constantin and Beyer, 2016). ..... 43

Figure 4.6. (a) loading points on the wall segment ; (b) the loading positions (Constantin and Beyer, 2016). ..... 44

Figure 4.7. TUC loading history (Constantin and Beyer, 2016)..... 44

Figure 4.8. Calibrated unconfined and confined concrete models for the web of TUC. ..... 46

Figure 4.9. Load displacement responses of specimen TUA. ..... 55

Figure 4.10. Load displacement responses of specimen TUB..... 57

Figure 4.11. Load displacement responses of specimen TUC. ..... 59

Figure 4.12. Load displacement responses of specimen TUD. ..... 62

Figure 4.13. Contributions of flexural deformations to wall top displacement for specimen TUA. ..... 64

Figure 4.14. Contributions of flexural deformations to wall top displacement for specimen TUB. ..... 65

Figure 4.15. Ratio of flexural deformations to shear deformations for specimen TUC. ..... 67

Figure 4.16. Ratio of flexural deformations to shear deformations for specimen TUD. ..... 68

Figure 4.17. Vertical strain profiles along wall height for specimen TUB. ..... 70

Figure 4.18. Vertical strain profiles along wall height for specimen TUC. ..... 71

Figure 4.19. Vertical strain profiles along wall height for specimen TUD. ..... 72

Figure 4.20. Specimen TUC: vertical strain distribution at wall base at a) position A, b) position B, c) position C, d) position D, e) position E, f) position F, g) position G, h) position H. ..... 73

Figure 4.21. Specimen TUC: shear stress distribution at wall base at: a) position A, b) position B, c) position C, d) position D, e) position E, f) position F, g) position G, h) position H. ..... 75

Figure 4.22. Specimen TUD: vertical strain distribution at wall base at a) position A, b) position B, c) position C, d) position D, e) position E, f) position F, g) position G, h) position H. ..... 77

Figure 4.23. Specimen TUD: shear stress distribution at wall base at: a) position A, b) position B, c) position C, d) position D, e) position E, f) position F, g) position G, h) position H. ..... 79

Figure A.1. Copyrights of Figure 1.1.....92

Figure A.2. Copyrights of Figure 1.2.....93

Figure A.3. Copyrights of Figure 1.3.....94

Figure A.4. Copyrights of Figure 1.4.....95

Figure A.5. Copyrights of Figure 1.5.....96

Figure A.6. Copyrights of Figure 2.1, Figure 2.2, Figure 2.3.....97

Figure A.7. Copyrights of Figure 2.4, Figure 2.5, Figure 2.6, Figure 2.9, and Figure 2.10. .....98

Figure A.8. Copyrights of Figure 2.11, Figure 2.12, Figure 3.1, and Figure 3.2. .....99

Figure A.9. Copyrights of Figure 4.1, Figure 4.2, Figure 4.3, and Figure 4.4. .....100

Figure A.10. Copyrights of Figure 4.5, Figure 4.6, and Figure 4.7. .....101

# LIST OF TABLES

Table 4.1. Number of meshes for each wall specimen. ..... 45

Table 4.2. Parameters for the calibration of the concrete model. ..... 47

Table 4.3. Parameters for concrete in tension. ..... 48

Table 4.4. Parameters for reinforcing steel. ..... 51

Table 4.5. Slenderness ratio calculation for reinforcing bar buckling. ..... 52

# LIST OF SYMBOLS

| | |
|---|---|
| $a_1$ *and* $a_2$ | Experimentally determined parameters that represent the degradation of the curvature within subsequent cycles |
| $A_t$ | Cross sectional area of ties |
| $b$ | Steel strain hardening ratio |
| $\{b_{n1}\}$, $\{b_{n2}\}$ | Reference displacement vector in both loading directions |
| $\{D\}$ | Global displacement vector |
| $d_{bar}$ | Bar diameter |
| $E_b$ | Reduced stiffness for unloading from compression |
| $E_c$ | Elastic modulus of concrete |
| $E_t$ | Elastic modulus of lateral ties |
| $E_{new}$ | New concrete tangent modulus upon return to unloading point on monotonic envelope |
| $E_{pl}$ | Concrete plastic modulus upon unloading from monotonic envelope |
| $E_s$ | Elastic modulus for steel |
| $E_{sec}$ | Concrete secant modulus upon unloading from monotonic envelope |
| $E_0$ | Elastic modulus for steel |
| $E_1$ | Strain hardening modulus for steel |
| $\{F\}$ | Global internal force vector |
| $f_c'$ | Peak concrete compressive strength |
| $f_{cr}$ | Concrete tensile strength |
| $\{F_{ext}\}$ | External force vector |
| $\{F_{I1}\}_I$, $\{F_{I2}\}_i$ | Reference force vector in both loading directions |
| $f_{it}$ | Steel stress corresponding to the strain at the intermediate point |
| $f_{new}$ | New concrete stress upon return to unloading point on monotonic envelope |
| $f_r$ | Concrete stress at point of return to monotonic envelope |
| $f_t$ | Concrete tensile strength |

| | |
|---|---|
| $f_y$ | Yield strength of the bare reinforcing steel bars |
| $f_{un}$ | Concrete stress at unloading point from monotonic curve |
| $\{F_{unb}\}$ | Unbalanced force vector |
| $h$ | Height of the mesh |
| $I_s$ | Moment of inertia of the rebar cross-section |
| $[K]$ | Global stiffness matrix |
| $[K_I]_i$ | Tangent stiffness matrix |
| $k_c$ | Foundation modulus of surrounding concrete |
| $k$ | Normalizing stiffness |
| $k_{eq}$ | Nondimensional average stiffness parameter of lateral ties |
| $k_t$ | Axial stiffness of tie legs along buckling direction |
| $L_{eff}$ | The length along which buckling of the longitudinal reinforcing bars takes place |
| $L/D$ | Slenderness ratio for reinforcing bars |
| $l_e$ | Tie length along the buckling direction |
| $m$ | Number of meshes in the horizontal direction |
| $n$ | Number of meshes in the vertical direction |
| $n$ | Stable buckling mode |
| $n_b$ | Number of longitudinal bars that are prone to simultaneous buckling |
| $n_l$ | Number of tie legs along buckling direction |
| $R$ | Parameter that influences the curvature of the transition curve between the two asymptotes |
| $R_0$ | The value assigned to the parameter R for the initial (or monotonic) loading |
| $r$ | Parameter defining shape of monotonic stress-strain curve for concrete |
| $r_t$ | Shape parameter for the tension envelope |
| $s$ | Spacing between lateral ties |
| $s_x$ | Distance between horizontal reinforcing bars |
| $s_y$ | Distance between vertical reinforcing bars |

| | |
|---|---|
| $[T]$ | Transformation matrix for body constraints |
| $x_{crn}$ | Nondimensional critical strain on concrete tension envelope |
| $x_{crp}$ | Nondimensional critical strain on concrete compression envelope |
| $V_{dow}$ | Dowel force acting on the horizontal and vertical reinforcement |
| $w$ | Width of the mesh |
| | |
| $\alpha$ | Coefficient for steel stress calculation at the intermediate point |
| $\alpha$ | Cyclic degradation parameter |
| $\gamma_{xy}$ | Shear strain |
| $\gamma_{crack}$ | Shear strains along the crack |
| $\{\delta_{I1}\}, \{\delta_{I2}\}$ | Tangent displacement vectors in both loading directions |
| $\Delta$ | Slip deformation |
| $\Delta_{crack}$ | Slip deformation along the crack |
| $\Delta_{max}$ | Maximum slip deformation through the experienced loading history |
| $\Delta_{dow}$ | Dowel deformations acting on the horizontal and vertical reinforcing steel bars |
| $\Delta\lambda_{i,1}, \Delta\lambda_{i,2}$ | Initial load increment in both loading directions |
| $\Delta\delta$ | Displacement increment |
| $\Delta\delta_{n1}, \Delta\delta_{n2}$ | Initial displacement increment in both loading directions |
| $\Delta\delta_R$ | Residual displacement increment |
| $\varepsilon'_c$ | Monotonic strain at peak concrete compressive stress |
| $\varepsilon_x$ | Normal strain in x direction |
| $\varepsilon_y$ | Normal strain in y direction |
| $\varepsilon_{x'}$ | Normal strain transformed to x' direction |
| $\varepsilon_{y'}$ | Normal strain transformed to y' direction |
| $\varepsilon_1$ | Normal strain in principal direction 1 |
| $\varepsilon_2$ | Normal strain in principal direction 2 |
| $\varepsilon_{cr}$ | Peak strain at tensile strength of concrete |
| $\varepsilon_{c0}$ | Concrete strain at which cyclic tension envelope originates |

| | |
|---|---|
| $\varepsilon_0$ | Strain at peak concrete compressive stress |
| $\varepsilon_0$ | Steel strain at peak concrete compressive stress |
| $\varepsilon_i$ | Steel strain at the intermediate point |
| $\varepsilon_m$ | Maximum plastic steel strain |
| $\varepsilon_{max}$ | Absolute maximum strain at strain reversal |
| $\varepsilon_{sh}$ | Steel strain at the starting point of hardening |
| $\varepsilon_{sc}$ | Steel compressive strain |
| $\varepsilon_{st}$ | Steel tensile strain |
| $\varepsilon_{pl}$ | Plastic strain upon unloading |
| $\varepsilon_r$ | Strain at the point of strain reversal |
| $\varepsilon_s$ | Maximum tensile strain at reinforcing steel |
| $\varepsilon_{sc}$ | Current steel strain |
| $\varepsilon_{sh}$ | Steel strain at the starting point of hardening |
| $\varepsilon_t$ | Concrete tensile strain at peak tension stress |
| $\varepsilon_{un}$ | Concrete strain at unloading point from monotonic envelope |
| $\varepsilon_y$ | Strain at monotonic yield point |
| $\lambda_{i,1}$, $\lambda_{i,2}$ | Updated load level in both loading directions |
| $\sigma_{cx}$ | Concrete normal stress in x direction |
| $\sigma_{cx'}$ | Concrete normal stress in x’ direction |
| $\sigma_{cx'A}$ | Concrete normal stress first fixed strut direction |
| $\sigma_{cy}$ | Concrete normal stress in y direction |
| $\sigma_{cy'}$ | Concrete normal stress in y’ direction |
| $\sigma_{cy'B}$ | Concrete normal stress in second fixed strut direction |
| $\sigma_{sx}$ | Reinforcing steel stress in x direction |
| $\sigma_{sy}$ | Reinforcing steel stress in y direction |
| $\sigma_x$ | Total normal stress in x direction |
| $\sigma_y$ | Total normal stress in y direction |
| $\sigma_{c\perp}$ | Compressive stress in concrete in perpendicular direction to the crack |

| | |
|---|---|
| $\sigma_r$ | Steel stress at reversal point |
| $\sigma_{sc}$ | Steel compressive stress |
| $\sigma_{st}$ | Steel tensile stress |
| $\sigma_y$ | Steel yield stress |
| $\sigma_0$ | Steel stress at intersection of elastic and yield asymptotes |
| $\tau_{cxy}$ | Concrete shear stress |
| $\tau_{cx'y'}$ | Concrete shear stress along x'y' direction |
| $\tau_{cx'y'A}$ | Concrete shear stress along first fixed strut direction |
| $\tau_{cx'y'B}$ | Concrete shear stress second first fixed strut direction |
| $\tau_{crack}$ | Shear aggregate interlock stress along crack surface |
| $\tau_{crack,deg}$ | Cyclic degradation parameter in shear aggregate interlock stress |
| $\tau_{xy}$ | Total shear stress |
| $\theta$ | Crack angle |
| $\theta_{rot}$ | Rotation at the crack interface |
| $\theta_{crA}$ | Concrete crack direction A or first strut direction |
| $\theta_{crB}$ | Concrete crack direction B or second strut direction |
| $\rho$ | Steel reinforcement ratio |
| $\xi$ | Absolute strain difference between current asymptote intersection point and the previous maximum or minimum strain reversal point |
| $\eta$ | Friction coefficient |
| $\Sigma\Delta$ | Cumulative slip deformation |

# LIST OF ACRONYMS/ABBREVIATIONS

| | |
|---|---|
| ACI | American Concrete Institute |
| ASCE | American Society of Civil Engineers |
| CSMM | Cyclic Softened Membrane Model |
| DOF | Degree of Freedom |
| DSFM | Disturbed Stress Field Theory |
| FA-STM | Fixed Angle Softened Truss Model |
| FEM | Finite Element Model |
| FSAM | Fixed Strut Angle Model |
| FSAFE | Fixed Strut Angle Finite Element |
| MCFT | Modified Compression Field Theory |
| QLMEDD | Quadrilateral Layered Membrane Element with Drilling Degrees of Freedom |
| RA-STM | Rotating Angle Softened Truss Model |
| RC | Reinforced Concrete |
| SMM | Softened Membrane Model |

# 1. INTRODUCTION

## 1. 1. General

Reinforced concrete structural walls are crucial in improving the lateral stiffness and response characteristics of structures in resist against earthquake and wind induced loadings. Since structural walls provide significant lateral strength, they limit damage and lateral displacements under service level earthquakes, while providing the sufficient ductility capacity to meet inelastic displacement demands under severe earthquakes. Therefore, use of structural walls in seismic zones and tall buildings are very common. Especially with the introduction of performance-based seismic design approach, analytical modeling of reinforced concrete walls has gained importance, since the accuracy in modeling the nonlinear behavior of structural walls are directly linked to their design. Due to their effectiveness in providing lateral strength and the need to use more robust modeling methods for reinforced concrete elements in performance-based analysis and design, understanding and characterizing the hysteretic behavior of reinforced concrete walls is essential.

U-shaped structural walls are a very common design configuration, and they are widely used around elevator shafts, stairs, and utility areas. Unlike rectangular walls, which contribute to the seismic response of a structure by a predominant bending mode in their strong direction, U-shaped walls have biaxial bending modes under seismic excitation. U-shaped walls in a building undergo bending about both principal axes of the wall cross-section. However, most experimental and analytical studies are conducted for rectangular walls under uniaxial lateral loading. Due to the scarcity of experimental results for nonrectangular walls under biaxial loading, sufficient progress in analytical modeling of nonrectangular walls under biaxial lateral loading has not yet been made.

Nonlinear behavior of structural walls can be modeled by using either macroscopic (behavioral) or microscopic (finite element) modeling methodologies. Microscopic modeling approaches are not usually used in performance-based analysis and design, due to increased need for computational power and the complexity of the modeling procedure,

while macroscopic (eg. fiber) modeling approaches are very commonly used. However, commonly used fiber-based models are based on the plane-sections-remain-plane and shear and flexural behaviors are uncoupled assumptions. Therefore, while they yield sufficiently good global results for flexure dominated walls, they cannot capture the experimentally observed shear-flexure interaction in both medium-rise and slender walls. Furthermore, due to the plane-sections-remain-plane assumption, especially for the nonrectangular walls, local responses (e.g., vertical strains) cannot be captured accurately by fiber-based models.

In this study, a relatively simple yet robust finite element modeling approach, referred to as the Fixed-Strut-Angle Finite Element Model (FSAFE, Gullu and Orakcal, 2019) is improved and used to simulate the nonlinear behavior of nonrectangular structural walls under biaxial lateral loading conditions. The constitutive model formulation for reinforcing steel is improved for simulating the buckling behavior of longitudinal reinforcing bars. A novel nonlinear solution strategy is proposed for analysis under biaxial loading conditions. The modified model formulation and the nonlinear analysis strategy is implemented in MATLAB. The model is calibrated for verified against available experimental data for four U-shaped walls tested under biaxial loading.

## 1. 2. Literature Review

Principals of continuum mechanics are used in microscopic modeling approaches. The walls are divided into smaller elements which are connected at their nodes and the nonlinear response is represented by a set of equations. In constitutive panel modeling approach, only the in-plane behavior is considered and typically, each node has two degrees of freedom. These models are supported by testing programs. In this context, various constitutive panel models were proposed for both monotonic (e.g. Vecchio and Collins, 1986; Pang and Hsu, 1995, 1996; Vecchio, 2000; Hsu and Zhu, 2002) and cyclic (Ohmori et al., 1989; Stevens et al., 1991; Palermo and Vecchio, 2003; Mansour and Hsu, 2005; Gérin and Adebar, 2009; Ulugtekin, 2010, Orakcal et al., 2012; Gullu and Orakcal, 2019) loading conditions.

To simulate the monotonic load-deformation behavior of RC panel elements, Mitchell and Collins (1974) introduced Diagonal Compression Field Theory (DCFT). After DCFT,

Vecchio and Collins (1986) conducted a testing campaign and proposed the Modified Compression Field Theory (MCFT). This proposition kept the essential features of the DCFT (e.g., coinciding principal stress and strain directions, perfect bond). Some additional behavioral parameters were also considered (e.g., compression softening, tension stiffening, and shear transfer along crack surfaces).

Mau and Hsu (1986) created a new panel model where they made use of equilibrium, compatibility, and material stress-strain relationships which were basically the same with the MCFT. Boundaries between different failure modes were determined. Mau and Hsu (1987) proposed an improvement to the model they introduced in 1986, by treating the cracked concrete as a new material working in diagonal compression strut directions. Hsu (1988) introduced a new theory, referred to as the Softened Truss Model (STM), based on the equilibrium, compatibility, and material stress-strain relationships where the shear transfer across cracks is represented by tension stiffening relationships rather than formulating the phenomenon discretely.

In 1989, several reversed-cyclic panel tests were conducted as a part of an experimental program at Kajima Institute of Construction Technology. By using the results of this testing program, a new nonlinear cyclic analysis method was introduced by Ohmori et al. (1989). This model incorporates an improved version of stress-strain models used in MCFT where the hysteretic characteristics can be captured, and cyclic behavior can be represented.

Stevens et al. (1991) tested three panel specimens and proposed a new cyclic constitutive panel model according to these panel tests. In the proposed model, a new approach where the principal strain and stress directions do not have to coincide, but the direction of increments should coincide was introduced.

Pang and Hsu (1995) proposed a new constitutive panel model referred to as the Rotating Angle Softened Truss Model (RA-STM). Parameters were introduced to represent compression softening and tension stiffening in addition to considering softening effect on reinforcing bars caused by the dowel action, the kinking effect. A year later, Pang and Hsu

(1996) developed another model named as the Fixed Angle Softened Truss Model (FA-STM). This model used the assumption of coinciding crack direction and principal stresses.

The Softened Membrane Model (SMM) was proposed by Hsu and Zhu (2002). The new model considered the Poisson's effect unlike the FA-STM formulation. In addition, new experimental data indicated that the kinking effect which was discussed in FA-STM was negligible. In 2005, 12 reinforced concrete panels were tested under reversed cyclic loading by Mansour and Hsu (Mansour and Hsu, 2005a). Based on this experimental program, an improvement to SMM was proposed (Masour and Hsu, 2005b). The major improvement is the new cyclic constitutive relationships for concrete and steel.

The Disturbed Stress Field Model (DSFM) was proposed as a new monotonic constitutive panel model by Vecchio (2000). This model does not use the assumption of coinciding principal stresses and strains. Also, these stresses and strains are separated by a "lag" angle while the crack direction follows the principal stress directions. An extension to this model was proposed by Palermo and Vecchio (2003), where the reversed-cyclic behavior was introduced through new hysteretic constitutive models for the materials.

Another constitutive panel model, the one proposed by Gérin and Adebar (2009), uses the combination of equilibrium, compatibility, and constitutive relationships to represent the response. Cracks form to maintain strain compatibility between reinforcement and cracked concrete. Cracks are independent of stresses in concrete which rotates to maintain equilibrium. The model uses average strains to separates the strains due to formed cracks and the strains from the concrete between the cracks. Due to this assumption, the angle of principal concrete stresses can diverge from the angle of principal average strains.

The Fixed Strut Angle Model (FSAM) was proposed by Ulugtekin (2010) and is extended by Orakcal et al. (2012). This constitutive panel model, which adopts a fixed crack approach, was shown to predict the behavior of RC panels under in-plane and reversed-cyclic loading. It is assumed that the orientations of the principal stress and principal strains coincide until the formation of the first crack which is similar to a rotating crack approach; however, after the formation of the cracks, the direction of principal stresses is fixed and

perpendicular to the crack directions while the principal strain continue to change directions. At first, this model assumed zero shear stresses along cracks which means zero shear aggregate interlock. Orakcal et al. (2012) improved this model by implementing a friction based aggregate interlock model. However, the proposed model does not have a dowel action model implemented. The efficiency of the model in simulation RC panel behavior was shown by comparing the model predictions with the experimental results for RC panels with varying reinforcement ratios and loading conditions available in the literature.

Bu using an iterative tangent-stiffness technique under incremental load or displacement, Mo. et al. (2008) integrated the Cyclic Softened Membrane Model (Mansour and Hsu, 2005b), into the open-source computational framework OpenSees developed by Pacific Earthquake Engineering Center (PEER). A module to represent four-node panel element and two more modules related to determination of material stiffness matrix are developed. The nonlinear finite element program developed by using these modules and OpenSees framework is called Simulation of Concrete Structures (SCS). The program was validated by using nine 1/3 scale framed structural walls. Constant axial load and reversed cyclic lateral loading was applied to all specimens. The difference between the test specimens were the axial load ratios and reinforcement ratios. Numerical model in SCS showed that the program can predict the hysteretic behavior of walls with different axial load and reinforcement ratios.

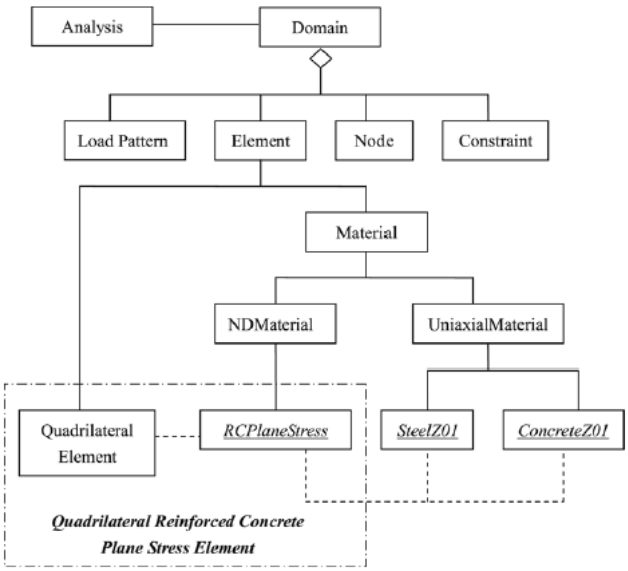


Figure 1.1. Implementation of CSMM into OpenSees (Mo et al., 2008).

Luu et al. (2017) used the CSMM to model the behavior of structures that are subjected to different loading scenarios such as monotonic, reversed-cyclic, and dynamic loading in OpenSees. They employed 8-node curved shell elements this time, and each component had three translational DOFs, two rotational DOFs, and one drilling degree of freedom. The nonlinear solution approach used a Newton-Raphson algorithm. Simulation of Three-Dimensional Concrete Structures (SCS-3D) is the name of the implemented formulation. Experimental data for four panel elements that are subjected to a combination of shear and bending, a RC tank, and a RC shear wall were used to validate the model.

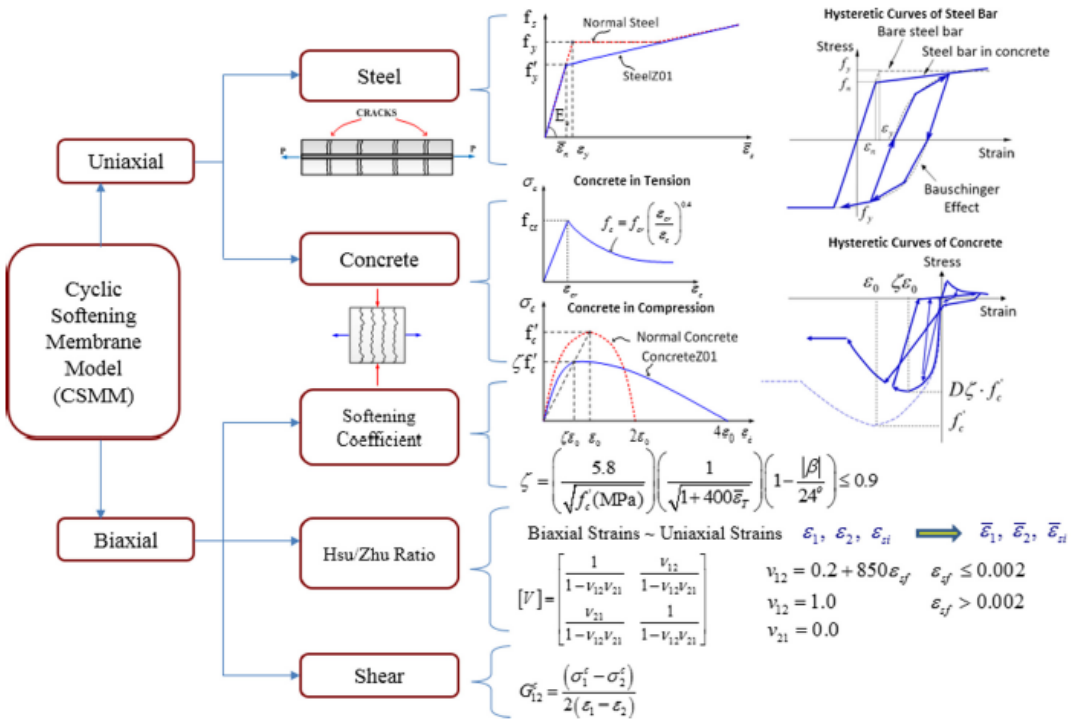


Figure 1.2. Overview of CSMM for reinforced concrete (Luu et al., 2017).

Quadrilateral Layered Membrane Element with Drilling Degrees of Freedom (QLMEDD) was proposed as a novel method for RC structural walls by Rojas et al (2016). This model uses a layered approach with quadrilateral elements with two translational DOFs and one drilling DOF per node. Layered approach allows the modeling of different material properties through the thickness of the walls (e.g. unconfined concrete, confined concrete, reinforcement, etc.). Rotating crack approach is adopted. For concrete, a uniaxial stress-strain relationship in the orientation of principal stress is used to represent the behavior. In

addition, Poisson effect is neglected after cracking due to possible convergence issues. For reinforcement, in addition to a smeared steel material proposed by Menegotto-Pinto (1973), a buckling model by Massone and Moroder (2009) was used in one of the modeled walls. For monotonic and reversed cyclic loading scenarios, the model was validated. Seven specimens were tested under monotonic loading, while three others were exposed to reversed/cyclic loading where a specimen has irregular openings. The model captured the capacity and stiffness of the walls with varying configurations under monotonic loading conditions with or without drilling degrees of freedom. For reversed/cyclic loading, the model can predict the local responses as well as the load-displacement curves.

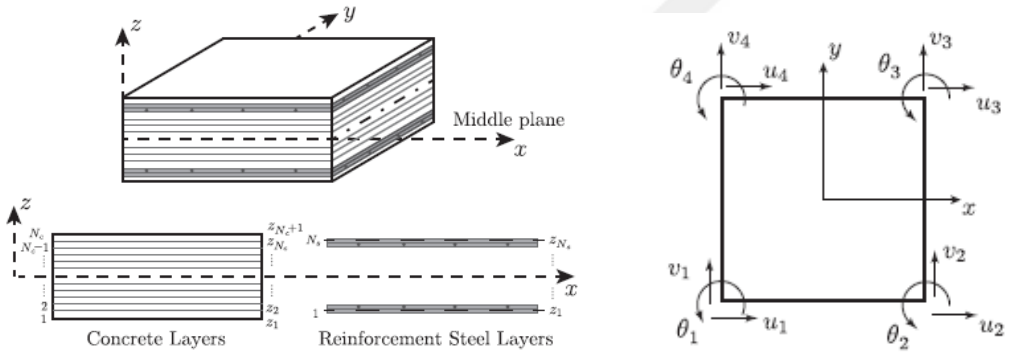


(a) (b)

Figure 1.3. (a) Layered membrane section, (b) element global degrees of freedom (Rojas et al., 2016).

VecTor2 is a nonlinear finite element analysis tool that is used for RC members subjected to combined shear and normal stresses. This tool makes use of MCFT (Vecchio and Collins, 1986) and DCFT (Vecchio, 2000) to model the response of RC panels. Material models used in this program considers compression softening, tension stiffening, tension softening, and tension splitting. Lu and Henry (2017) used VecTor2 to predict both the local and global behavior of lightly reinforced walls. Six lightly reinforced walls with changing features are used in this study. Wall sections are represented by four-node elements while the vertical reinforcement is represented by two-node truss elements. During the modeling phase, the mesh size found to be an important parameter to capture the crack patterns and localization of reinforcement strains. Verification of model against experimental data showed that the model can reasonably simulate the local and global responses, crack patterns,

the height over the cracks are formed, vertical strains, and drift capacities at the onset of reinforcement buckling and fracture. However, the reinforcing bar buckling could not be captured even though the lightly reinforced concrete walls are prone to reinforcement buckling since few large flexural cracks that dominate their behavior. A numerical study was also carried out by modeling eleven walls to evaluate the effects of wall dimensions and material properties on lateral load response, which were shown to be impacting the lateral drift capacities of lightly reinforced walls.

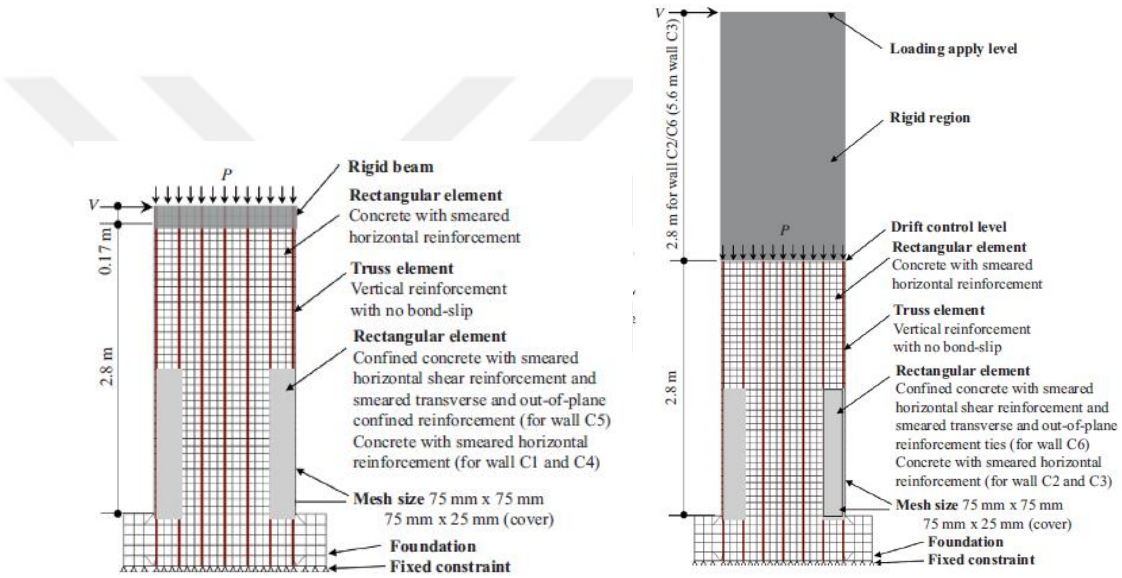


(a) (b)

Figure 1.4. (a) Discretization of walls with shear span ratio of 2, (b) discretization of walls with shear span ratio larger than 2 (Lu and Henry, 2017).

Dashti et al. (2017) used commercial software DIANA9.4.4 (DIANA, 2011) to conduct nonlinear analysis of structural walls. 8-node curved shell elements, each node having three translational and two rotational degrees of freedoms are used to discretize the wall sections. Without introducing an eccentricity, these elements can replicate the out-of-plane behavior under in-plane forces. For reinforcement, bar elements are embedded into the shell elements. A rotating crack technique was employed to replicate the behavior of curved shell elements. This approach is named as Total Strain Crack Model, which follows MCFT (Vecchio and Collins, 1986) and available in DIANA. For the concrete model, Mander's Model was implemented into Total Strain Crack Model. The behavior of reinforcement was

defined by the well-known Menegotto-Pinto Model (1973). The numerical model was verified against existing experimental data for structural walls. These wall specimens are selected such that they have varying shear-span ratios, loading conditions (eg. monotonic, reversed-cyclic, etc.) and failure mechanisms. Overall, the numerical model and experimental results showed good correlation. However, for walls which shear-flexure dominates the behavior, though the model can capture the out-of-plane deformations, bar buckling, and rupture were not predicted since the reinforcement model does not consider bar buckling.

Gullu and Orakcal (2019) introduced a new finite element model referred to as the Fixed Strut Angle Finite Element (FSAFE), which uses an extension of the FSAM (Orakcal et al., 2012) as the constitutive formulation. The FSAFE model incorporates four node panel elements with two translational DOFs per node and a single Gauss integration point, along with linear strain interpolation functions. Shear-aggregate interlock mechanism is described by using a friction-based relationship. FSAM formulation did not consider the dowel action on the reinforcement. A simple constitutive relationship for the dowel action on reinforcement is implemented, using the origin-oriented hysteresis rules. The material models for concrete and reinforcing steel are defined by Chang and Mander model (1994) and Menegotto-Pinto model (1973) improved by Filippou et al. (1983), respectively. FSAFE employs a displacement-based nonlinear solution technique. The model is verified against experimental data for six wall specimens available in the literature. With favorable accuracy, the global and local response of six wall specimens in the literature that had different response characteristics was shown to be simulated by FSAFE.

.

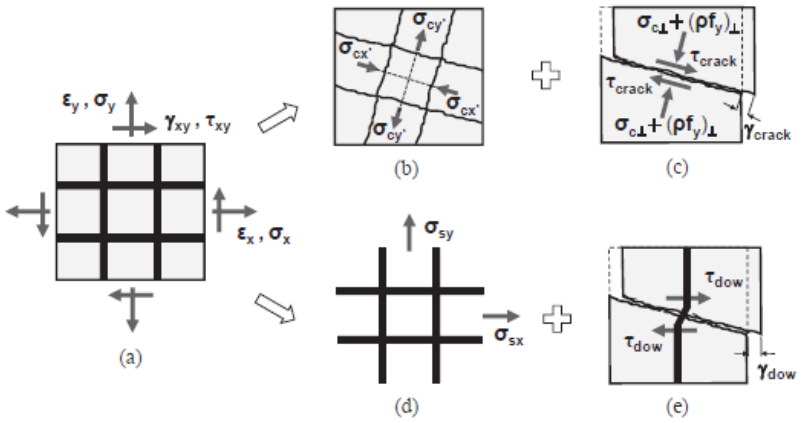


Figure 1.5. FSAM: (a) strain field on a panel element, (b) concrete stresses along fixed struts, (c) shear aggregate interlock stresses along cracks, (d) uniaxial stresses in reinforcement, (e) dowel stresses in reinforcement (Kolozvari et al., 2019).

A comparative study of five-state-of-the-art finite element models for structural walls was conducted by Kolozvari et al (2019). The models compared in this study were VecTor2 (Wong et al., 2002), FSAFE (Gullu and Orakcal, 2019), DIANA (DIANA, 2011), QLMEDD (Rojas et al., 2016), and LS-DYNA (Murray, 2007). VecTor2, FSAFE, DIANA, and QLMEDD were previously explained previously, so only LS-DYNA is described herein. LS-DYNA is a commercial software where a layered shell formulation is used. Two unconfined concrete, two horizontal reinforcement, two vertical reinforcement, and one confined concrete layer, seven layers in total, are considered in the formulation. A fixed crack model, MAT_CONCRETE_EC2 which is available in LS-DYNA is used to recreate the hysteretic nonlinear characteristics of concrete. Reinforcing bars are treated as bar elements and modeled using the material model MAT_HYSTERETIC_REINFORCEMENT. Five rectangular wall sections were chosen for model validation, representing different wall response parameters and characteristics. Results obtained from all state-of-the-art finite element models displayed reasonable accuracy in terms of simulating the inelastic wall responses.

## 1.3. Objectives and Scope

The aim of this study is to model and experimentally verify the nonlinear response of nonrectangular walls with varying axial load levels, reinforcement distributions, and biaxial

quasi-static lateral loading protocols. The baseline formulation of the modeling approach used in this study follows the Fixed Strut Angle Finite Element (FSAFE) Model (Gullu and Orakcal, 2019), which was previously shown to be capable of replicating the nonlinear behavior of rectangular walls, at both global and local response levels.

Within the scope of this thesis, the FSAFE model formulation was extended to construct a finite element model assembly of nonrectangular walls. As well, a new nonlinear analysis solution strategy was developed, for analyzing the walls under biaxial lateral loading. Furthermore, a simplified buckling model for reinforcement was implemented in the model formulation. The improved model formulation, together with the new nonlinear analysis solution strategy was implemented in MATLAB. Verification of the model's ability to simulate the response of U-shaped walls subjected to complex multidirectional loading was conducted using well-documented experimental data available in the literature. Model predictions and experimental measurements were systematically compared in order to identify the capabilities and limitations of the model, in terms of simulating both the global and local response characteristics of nonrectangular walls subjected to biaxial loading.

### 1.4. Thesis Outline

This thesis provides a description of the improved FSAFE model, followed by results of detailed correlation studies between model results and test data, and is composed of five chapters. The first chapter includes the introduction, literature review, objectives and scope of this study, and the outline of this thesis. Descriptions of constitutive modeling approach and material models implemented in this study are provided in Chapter 2. Details of the finite element model formulation and the nonlinear analysis solution strategy are presented in Chapter 3. A description of the experimental program and test specimens used for validation of the model, calibration of the model parameters for the test specimens, and detailed comparisons between model predictions and test results are provided in Chapter 4. Finally, in Chapter 5, a summary of the study, concluding remarks, and recommendations for future improvements are presented.

# 2. CONSTITUTIVE MODEL DESCRIPTION

## 2.1. Overview of Fixed Strut Angle Finite Element (FSAFE) Model

In this study, a two-dimensional finite element modeling approach referred to as the Fixed Strut Angle Finite Element (FSAFE) model is used as a baseline model and is improved upon. The constitutive behavior of the FSAFE model is based on the Fixed Strut Angle Model (FSAM, Ulugtekin, 2010, Orakcal et al., 2012). FSAFE uses quadrilateral elements with eight degrees of freedom in total. The model uses linear strain interpolation functions and only one Gauss integration point located at the center of the quadrilateral element. In the FSAFE formulation, the FSAM is incorporated as a constitutive panel (membrane) model, in the form of a relationship between the average strain field $(\varepsilon_x, \varepsilon_y, \gamma_{xy})$ and the resulting smeared stress field $(\sigma_x, \sigma_y, \tau_{xy})$. The adequacy of the FSAM in representing the hysteretic nonlinear behavior of RC panels was validated by using available experimental results for RC panels in the literature (Orakcal et al., 2012, 2019). FSAFE adopts a direct stiffness approach for assembly of quadrilateral elements to generate global stiffness matrix and internal force vector for a wall model. Various conditions (e.g., support conditions, loading conditions, and body constraints) are incorporated in the model formulation. FSAFE was shown to predict the nonlinear behavior of structural walls with varying characteristics with reasonable accuracy (Gullu and Orakcal, 2019).

The original formulation of the constitutive model FSAM (Ulugtekin, 2010) neglected shear aggregate interlock effect and dowel action on the reinforcing bars. Orakcal et al. (2012) improved the FSAM by adding a friction-based shear aggregate interlock model. In the FSAFE model formulation (Gullu and Orakcal, 2019), in addition to the friction-based model for shear aggregate interlock, dowel action on the reinforcement was also incorporated. A more refined modeling approach was used for squat walls (Gullu, 2019), where more robust constitutive models were adopted to represent the shear stress transfer across cracks in concrete and dowel action on reinforcement.

## 2.2. The Fixed Strut Angle Model (FSAM) for RC Panel (Membrane) Behavior

The FSAM (Ulugtekin, 2010, Orakcal et al., 2012, and Orakcal et al., 2019) assumes equal strain field on both concrete and reinforcement which means that the bond between concrete and reinforcement is also assumed to be perfect. The reinforcing bars develop uniaxial stresses and strains in the longitudinal direction and do not develop shear stresses perpendicular to their orientations. This assumption implies that the dowel action on reinforcement is not considered in the model. The behavior of concrete is defined by using biaxial stress-strain relationships which also represents parameters such as compression softening and tension stiffening effects. The model simulates the hysteretic nonlinear behavior of RC panels by employing a rotating crack approach which similar to MCFT (Vecchio and Collins, 1986) before cracking and a fixed crack approach after the first cracking.

Before the formation of the first crack, the strain field acting on the element is transformed into principal strains which are assumed to coincide with the directions of principal stresses. Until cracking, the uniaxial concrete stress-strain relationships are applied in the directions of principal strains by using the monotonic stress-strain relationship.

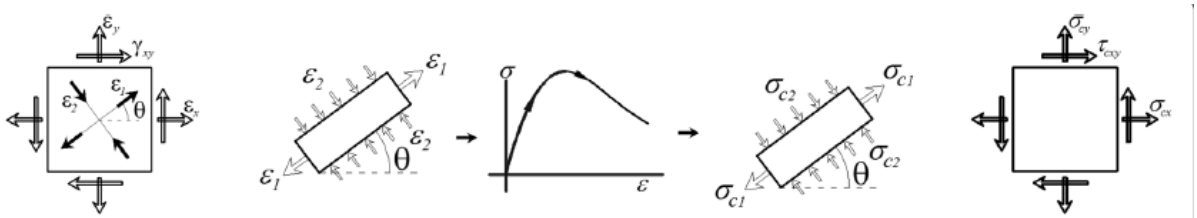


Figure 2.1. Uncracked behavior of concrete in the FSAM (Orakcal et al., 2019).

The first crack forms when the principal tensile strains in concrete first exceeds the cracking strain of the concrete and this principal strain direction is assigned as the fixed crack direction. The first “Fixed Strut” is assumed to develop parallel to the crack. After the cracking, while the principal strain direction continues to rotate according to applied strain field, the directions of the principal stresses are assumed to be fixed parallel and perpendicular to the orientation of the crack which is a fixed crack approach. This

assumption in the original formulation of FSAM (Ulugtekin, 2010) enforces that there are no shear aggregate interlock effects. Uniaxial stress-strain relationship for concrete is applied in the principal stress directions. In order to obtain stresses in the principal directions, the applied strain fields are transformed into principal strains parallel and perpendicular to the fixed strut.

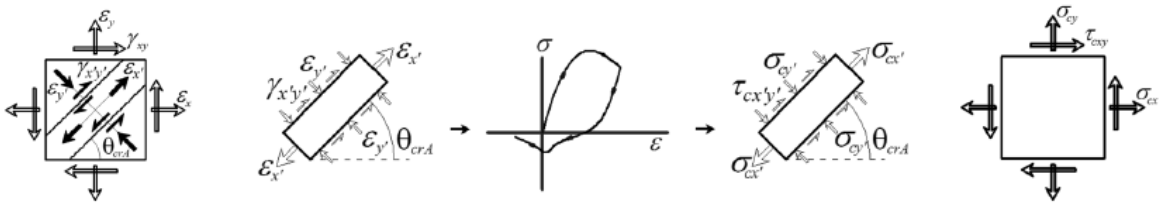

Figure 2.2. Behavior of concrete after the formation of first crack in FSAM (Orakcal et al., 2019).

When the strains in the first crack direction exceeds the cracking strain of the concrete, second crack is formed perpendicular, which is enforced by zero shear aggregate interlock assumption, to the first one according to a stress-based cracking criterion. Similar to the formation of the first crack, the principal strain direction is free to rotate while the principal stress direction is fixed parallel and perpendicular to the second crack, which implies zero shear aggregate interlock. The second "Fixed Strut" is assumed to develop parallel to this crack. After the development of the second fixed strut, the two independent fixed struts work in tension and compression in an interchanging manner. The uniaxial stress-strain relationship for concrete is used parallel to the first and second strut directions by transforming the applied strain fields into strains parallel to the fixed struts. On top of the original formulation (Ulugtekin, 2010), Orakcal et al. (2012) implemented a simple friction-based model shear aggregate interlock effect.

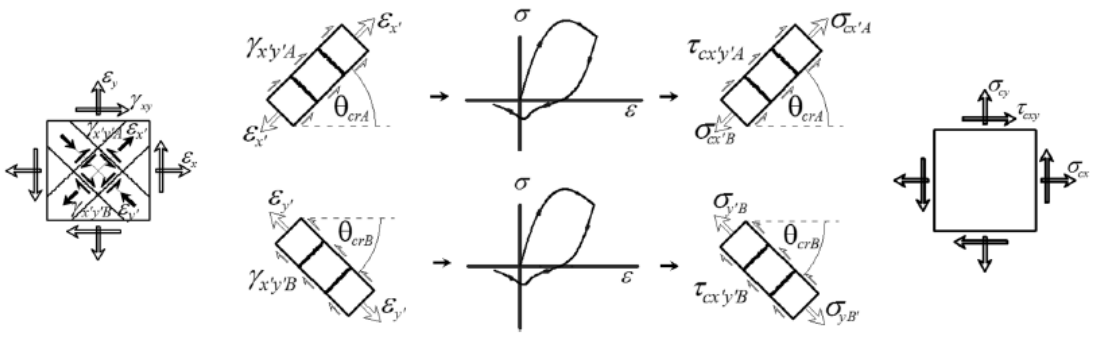

Figure 2.3. Behavior of concrete after formation of second crack in FSAM (Orakcal et al., 2019).

## 2.3. Material Constitutive Relationships

### 2.3.1. Concrete

The uniaxial hysteretic constitutive model used in the implementation of FSAFE is the one by Chang and Mander (1994). Chang and Mander (1994) model is an advanced rule-based model which is applicable to general purpose models. It can capture the hysteretic behavior of unconfined and confined both ordinary and high-strength concrete in cyclic compression and tension. This model particularly focuses on addressing the stress-strain transition between opening and closing of cracks. Existing models generally assume sudden crack closure with a rapid section modulus change that is not observed in experimental studies. Studies by Karsan and Jirsa (1969) and model by Mander et al. (1988a) shows that monotonic curve can be used as the envelope for the hysteretic stress-strain behavior. Concrete in tension with a cyclic behavior was shown to display similar characteristics to that in tension (Gopalaratnman and Shah, 1985; Yankelevsky and Reinhardt, 1987). Thus, Chang and Mander (1994) model treats concrete in cyclic tension in a similar manner. The envelope curves for tension and compression can be improved using new test results.

In the FSAFE model formulation used in this study, the stress-strain relationship for concrete is based on the Chang and Mander (1994) model. However, on top of the baseline Chang and Mander (1994) formulation, the constitutive model adopted in this study for concrete also incorporates parameters representing tension stiffening (Belarbi and Hsu,

1994), compression softening (Vecchio and Collins, 1993), hysteretic biaxial damage (Mansour et al., 2002).

Initial modulus of elasticity of concrete $E_c$, concrete strength $f_c'$, concrete strain at the peak $\varepsilon_c'$, and a parameter $r$ to define the shape of the compression envelope (Tsai, 1988) are used to define the compression curve for concrete. The tension curve is defined in a similar fashion. Hysteretic properties of the concrete are defined by empirical relationships using key parameters such as secant stiffness $E_{sec}$ and plastic stiffness $E_p$ upon unloading from the envelope and stress offset $\Delta f$ and strain offset $\Delta \varepsilon$ upon return to compression envelope Figure 2.4.

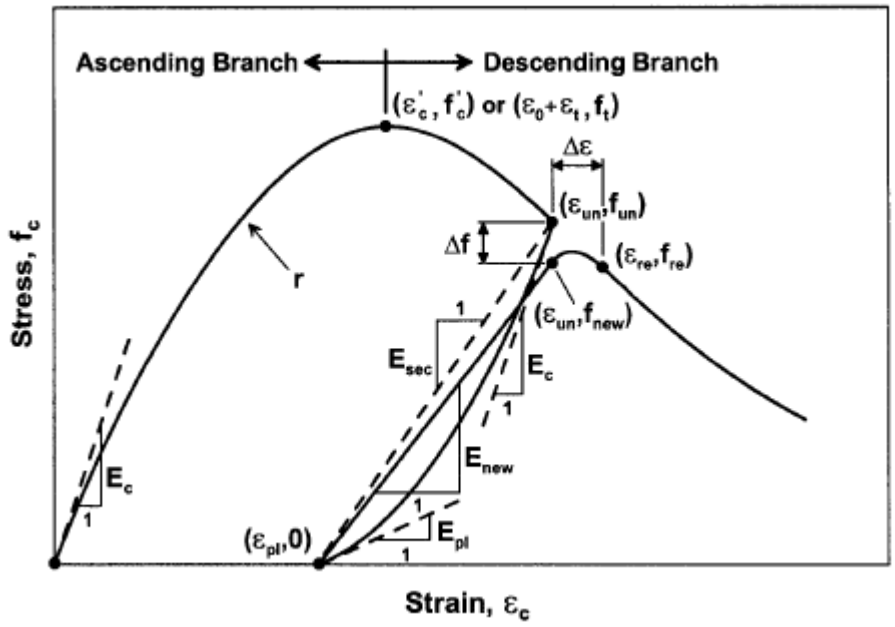


Figure 2.4. Hysteretic parameters of the concrete model according to Chang and Mander, 1994 (Orakcal, 2004).

The unloading and reloading between compression and tension curves are connected smoothly and partial unloading is succeeded by using similar transition curves. The hysteretic model for concrete is shown in Figure 2.5.

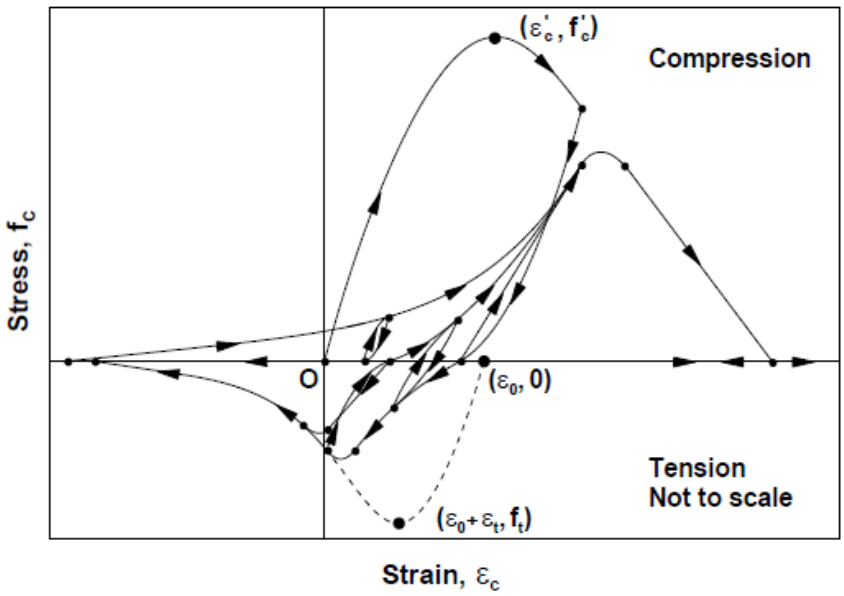


Figure 2.5. Hysteretic rules for concrete according to Chang and Mander, 1994 (Orakcal, 2004).

### 2.3.2. Reinforcing Steel

In the original formulation of the FSAFE model, the Menegotto and Pinto (1973) relationship, which was improved by Filippou et al. (1983) with the introduction of isotropic strain hardening was used to describe the behavior of reinforcing steel. The model was further improved further by Kolozvari et al. (2018) by fixing the stress overshooting upon strain reversals with small magnitude. This model by Menegotto and Pinto (1973) is known for its computational efficiency and accurate representation of experimentally observed stress-strain histories. In this study, the Menegotto-Pinto (1973) model is used to represent reinforcing bar behavior at the web sections of walls, while the longitudinal reinforcing bar behavior at wall boundary regions are represented by a simplified version of the Dhakal and Maekawa (2002a) model, which considers reinforcing bar buckling.

The Menegotto-Pinto (1973) model uses curved transitions for the stress-strain relationships. Each of these curved transitions are from a straight-line asymptote with slope $E_0$ to another straight-line asymptote $E_1 = bE_0$ where $E_0$ is the modulus of elasticity, $E_1$ is

the yield modulus and b is the strain hardening ratio. The uniaxial stress-strain relationship is defined as

$$\sigma^* = b\varepsilon^* + \frac{(1-b)\varepsilon^*}{(1+\varepsilon^{*R})^{1/R}} \tag{2.1}$$

$$\varepsilon^* = \frac{\varepsilon-\varepsilon_r}{\varepsilon_0-\varepsilon_r} \tag{2.2}$$

$$\sigma^* = \frac{\sigma-\sigma_r}{\sigma_0-\sigma_r}. \tag{2.3}$$

where $\sigma_r$ and $\varepsilon_r$ are the stress and strain values at the strain reversals. $\sigma_0$ and $\varepsilon_0$ are the stress and strains at the intersection of the two asymptotes. The curvature of the transition curves is defined by using a parameter *R* which is defined based on the strain history and allows the representation of the Bauschinger's effect. The parameter *R* in Menegotto-Pinto (1973) model is defined as

$$R = R_0 - \frac{a_1\xi}{a_2+\xi} \tag{2.4}$$

where $R_0$ is the initial value for *R* while $a_1$ and $a_2$ are experimentally determined parameters to simulate the degradation in curvature under cyclic loading. $\xi$ is the parameter representing the absolute strain difference between the current asymptote intersection point and the previous maximum or minimum strain reversal points.

The Menegotto-Pinto (1973) formulation implemented in FSAFE also considers the empirical relationships for tension stiffening (Belarbi and Hsu, 1994) in the definition of the tensile yield strength and strain-hardening parameters. However, this formulation does not consider reinforcing bar buckling or fracture behavior.

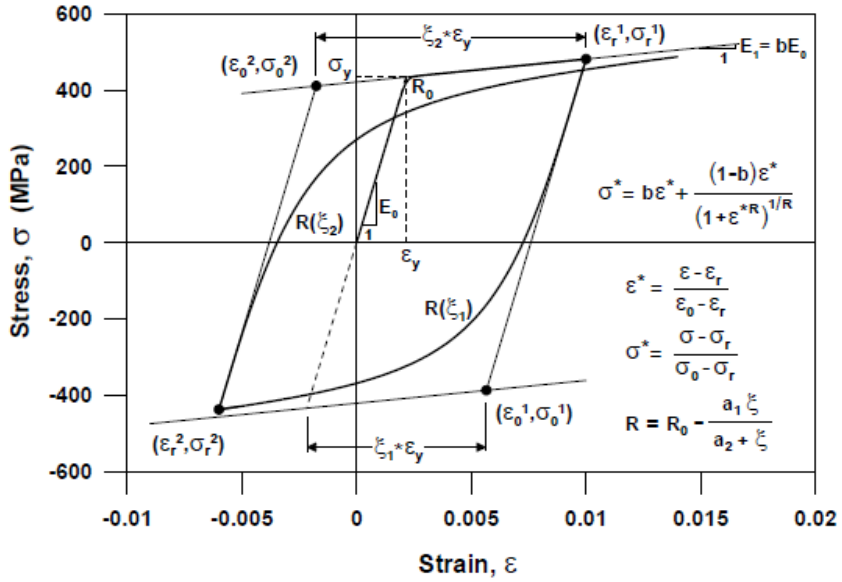


Figure 2.6. Constitutive model for reinforcing steel according to Menegotto and Pinto, 1973 (Orakcal, 2004).

For the regions where reinforcing bar buckling behavior is expected (i.e., wall boundary regions), a simplified version of the Dhakal and Maekawa (2002a) model is used in this study to also incorporate reinforcing bar buckling behavior. Dhakal and Maekawa (2002a) model is a path-dependent cyclic model (i.e. covers all possible strain paths) for reinforcing bars, which considers how geometrical and mechanical properties of the bars influence their post-buckling behavior. The formulation implemented in this study assumes an elasto-plastic tension envelope, variable unloading stiffness from compression, and isotropic strain hardening only in tension. The tension envelope is defined by

$$\sigma_{st} = E_s\varepsilon_{st} \quad for \quad \varepsilon_{st} \leq \varepsilon_y \tag{2.5}$$

$$\sigma_{st} = f_y \quad for \quad \varepsilon_y < \varepsilon_s \leq \varepsilon_u. \tag{2.6}$$

Dhakal and Maekawa (2002a) states that $L/D\sqrt{f_y}$ can be used to represent the average compressive stress-strain relationship and the trend of average compressive stress degradation. The compression envelope is defined as

$$\sigma_{sc} = E_s \varepsilon_{sc} \quad for \quad \varepsilon_{sc} \leq \varepsilon_y \tag{2.7}$$

$$\frac{\sigma_{sc}}{\sigma_t} = 1 - \left(1 - \frac{f_i}{f_{it}}\right)\left(\frac{\varepsilon_{sc} - \varepsilon_y}{\varepsilon_i - \varepsilon_y}\right) \; for \; \varepsilon_y < \varepsilon_s \leq \varepsilon_u \tag{2.8}$$

$$\sigma_{sc} = f_i - 0.02E_s(\varepsilon_{sc} - \varepsilon_i); \; \sigma_{sc} \geq 0.2f_y \; \; for \; \varepsilon_{sc} > \varepsilon_i \tag{2.9}$$

where $\sigma_t$ is the stress corresponding to the current strain $\varepsilon_{sc}$ while $f_{it}$ is the stress corresponding to strain at the intermediate point $\varepsilon_i$. Normalizing the compressive stress $\sigma_{sc}$ before the intermediate point makes the model applicable to a wide range of material models as well as ensuring a similar shaped average compression envelope to the tension envelope.

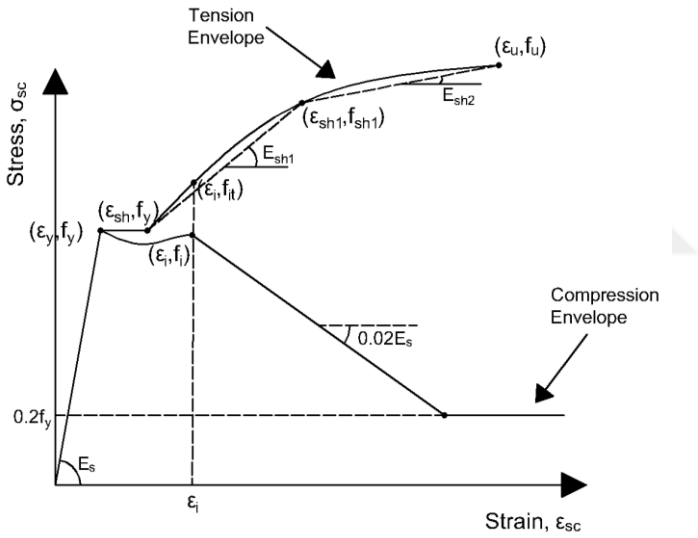


Figure 2.7. Schematic representation of monotonic compression envelope for the reinforcing steel model incorporating buckling.

The coordinates of intermediate point on the average compression envelope can be obtained in relation to the reinforcing bar slenderness ratio, $L/D\sqrt{f_y}$, as follows

$$\frac{\varepsilon_i}{\varepsilon_y} = 55 - 2.3\sqrt{\frac{f_y}{100}}\frac{L}{D}; \qquad \frac{\varepsilon_i}{\varepsilon_y} \geq 7 \tag{2.10}$$

$$\frac{f_i}{f_{it}} = \alpha\left(1.1 - 0.016\sqrt{\frac{f_y}{100}}\frac{L}{D}\right); \qquad \frac{f_i}{f_y} \geq 0.2 \tag{2.11}$$

where $\varepsilon_i$ and $f_i$ represent the current strain and stress values on the compression curve, $\varepsilon_y$ and $f_y$ are the yield strain and stress of the reinforcing bars, $\varepsilon_u$ and $f_u$ are the ultimate strain and stress of the reinforcing bars, $\varepsilon_{sh}$ is the strain at the beginning of the strain hardening, and $\alpha$ is a coefficient needed for stress calculation at the intermediate point. Dhakal and Maekawa (2002a) suggests using 0.75 for the elastic-perfectly plastic bars while 1.0 for bars with continuous strain hardening. For bars with limited strain hardening capacities, the use of Equation 2.12 is suggested

$$\alpha = 0.75 + \frac{\varepsilon_u - \varepsilon_{sh}}{300\varepsilon_y}; \qquad \alpha \leq \frac{f_u}{1.5 f_y}; 0.75 \leq \alpha \leq 1.0. \tag{2.12}$$

Dhakal and Maekawa (2002a) uses the cyclic rules defined by Menegotto-Pinto model (1973) with some modifications to consider the effect of buckling. One of these modifications is a simplification about the joining of the cyclic loops with monotonic compression and tension envelops and another one is that the formulation in this study follows the already defined asymptotes at the target points. Tension asymptote is the same as the strain hardening branch of the tension envelope and shifted upwards at each cycle according to isotropic strain hardening formulation incorporated into Menegetto and Pinto (1973) by Filippou et al. (1983). This shift is given by

$$\frac{\sigma_{st}}{\sigma_y} = a_3 \left( \frac{\varepsilon_{max}}{\varepsilon_y} - a_4 \right) \tag{2.13}$$

where $a_3$ and $a_4$ are experimentally determined values and $\varepsilon_{max}$ is the absolute maximum strain at strain reversal.

The compression asymptote is defined as the line connecting the cyclic minimum strain point ever reached with the monotonic yield point and the negative slope of this compression asymptote is limited to 3% of Young's modulus. Since the reloading stiffness from compression after buckling is observed by Suda et al. (1996) and Monti and Nuti (1992) to be significantly decreasing, Dhakal and Maekawa (2002a) suggests the following equation to account for this change in reloading stiffness

$$E_b = E_s \left(\frac{\sigma_{min}}{\sigma_{tmin}}\right)^2 ; E_b \leq E_s \; for \; \varepsilon_r < -\varepsilon_y \tag{2.14}$$

where $\sigma_{min}$ and $\sigma_{tmin}$ are the stresses on the compression and tension curves at the minimum strain.

Similarly, Dhakal and Maekawa (2002a) suggests another equation to account for the effects of buckling on reinforcing bars in tension after the yield point. The authors propose the use of the Equation (2.15) originally proposed by Dodd and Restrepo-Posada (1995) which considers the reduction in unloading stiffness with increasing plastic tensile strain after the yield point on the tension envelope. The reduced unloading stiffness is

$$\frac{E_u}{E_s} = 0.82 + \frac{1}{5.55+1000\varepsilon_m} \tag{2.15}$$

where $E_u$ is the unloading stiffness from tension and $\varepsilon_m$ is the maximum plastic strain. Both $E_b$ and $E_u$ are updated when the maximum compressive and tensile strains, respectively, are exceeded.

As previously mentioned, Dhakal and Maekawa (2002b) defines buckling depending on a slenderness ratio. Dhakal and Maekawa (2002b) assumes an idealized system where a flexural member is fixed at both ends while discrete elastic springs simulate the tie behavior. The deformed shape of the flexural members is defined by a cosine function. The required spring stiffness is calculated by minimizing the energy of two consecutive buckling modes with respect to their maximum amplitudes. The nondimensional average stiffness of the ties, $k_{eq}$, is defined as

$$k_{eq} = \frac{k_t}{k} = k_t \left(\frac{s^3}{\pi^4 EI}\right) \tag{2.16}$$

$$k_t = \frac{E_t A_t}{l_e} \frac{n_l}{n_b} \tag{2.17}$$

$$EI = \frac{E_s I}{2} \sqrt{\frac{f_y}{400}} \tag{2.18}$$

where $k_t$ represents the stiffness of lateral ties while the axial stiffness of each longitudinal bar is $\frac{E_t A_t}{l_e}$ where $E_t$, $A_t$, $l_e$ are the elastic modulus, cross-sectional area, and the tie length, respectively. $n_l$ is the number of tie legs in each direction while $n_b$ is the number of buckling prone longitudinal reinforcing bars in the same direction. As the last step, effective buckling length is calculated by using the stable buckling mode, n, and the tie spacing, s, as follows

$$L_{eff} = n\, s. \tag{2.19}$$

The stable buckling mode, n, is decided through a comparison between the stiffness required to hold the longitudinal reinforcing bars in place in different buckling modes that was obtained through energy principals by Dhakal and Maekawa (2002b) and the average stiffness of the ties, $k_{eq}$.

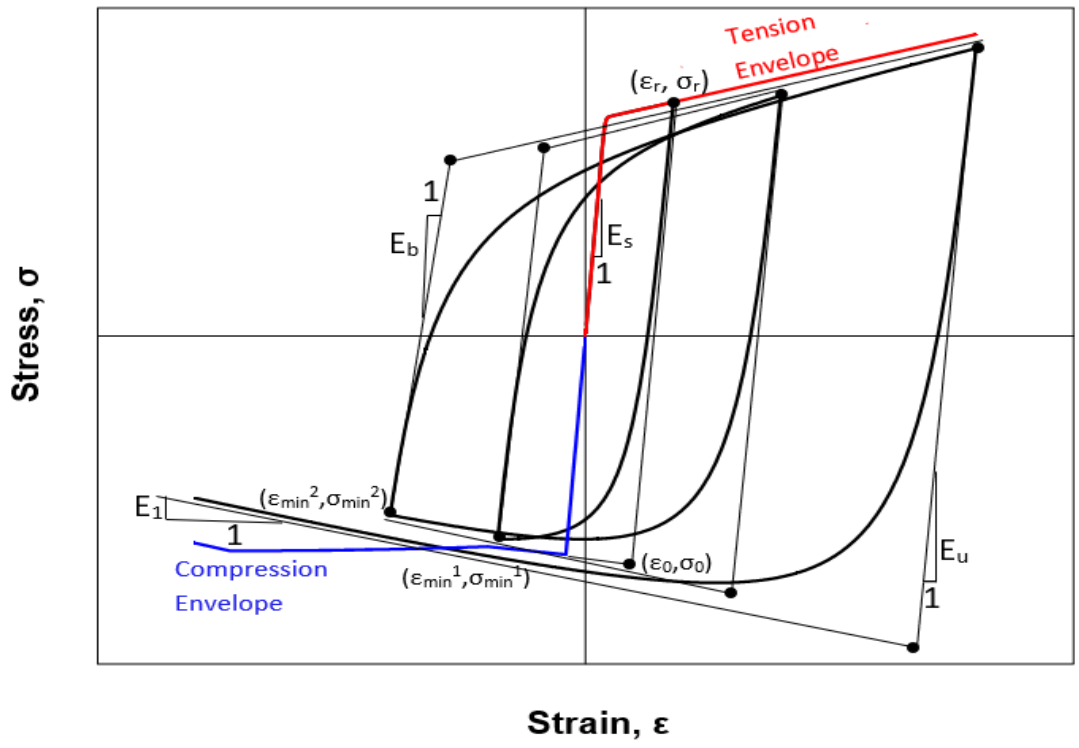


Figure 2.8. Hysteretic rules for the reinforcing steel constitutive model incorporating buckling.

### 2.3.3. Compression Softening in Concrete

Compression softening effect is an important subject that needs to be considered in the modeling of RC panels under membrane actions. Experimental observation of the compression softening effect is done by many researchers such as Vecchio and Collins (1986). Compression softening due to the tensile strains in the perpendicular direction are represented in the analytical models by reducing the compressive stresses in concrete in the principal directions.

The Model B proposed by Vecchio and Collins (1993) was used due to its simplicity in implementation to the cyclic panel model and its high capability of simulating compression softening effect similar to more complex models. Model B by Vecchio and Collins (1993) considers only a reduction by a coefficient in the peak compressive stress.

### 2.3.4. Tension Stiffening on Concrete and Steel

The tension stiffening phenomenon arises from the contribution of concrete between the cracks bonded to reinforcing bars to the tensile strength of RC members. Several researchers (e.g. Belarbi and Hsu, 1994) proved that tension stiffening significantly influences the post-cracking deformations on RC structures. Post-cracking stiffness, yield capacity, and shear behavior is observed to be influenced by the tension stiffening.

Tension stiffening phenomenon is introduced to FSAM formulation by using Belarbi and Hsu (1994) model. A smeared tensile stress-strain relationship for cracked concrete is considered while replacing the stress-strain curve for bare mild steel bars with a smeared stress-strain curve for steel bars stiffened by concrete between the cracks. Belarbi and Hsu (1994) model defines a linear tensile stress-strain relationship for concrete until cracking and a descending stress-strain curve relationship for the post-cracked behavior.

Another point considered by Belarbi and Hsu (1994) is the difference between the stress-strain relationship of reinforcing bars bonded to the concrete and bare steel bars. The yield strength of the RC members is reduced since the yielding of reinforced concrete

members take place when the steel stress at the crack section reaches to the yield strength of the bars. The average smeared steel stress reached by the RC member is lower than the yield strength of a bare reinforcing bar. Cross-sectional area of the longitudinal bars, ratio of moduli of elasticity of steel to concrete, ratio of cracking stress of concrete to the yield stress of the steel are experimentally observed to influence the reduction in the yield stress of the bars bonded to concrete in an empirical manner.

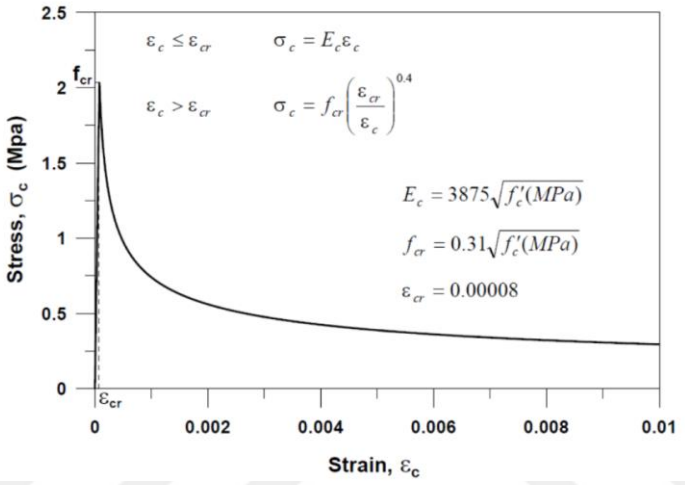


Figure 2.9. Average stress-strain relationship by Belarbi and Hsu (1994) for concrete in tension (Orakcal, 2004).

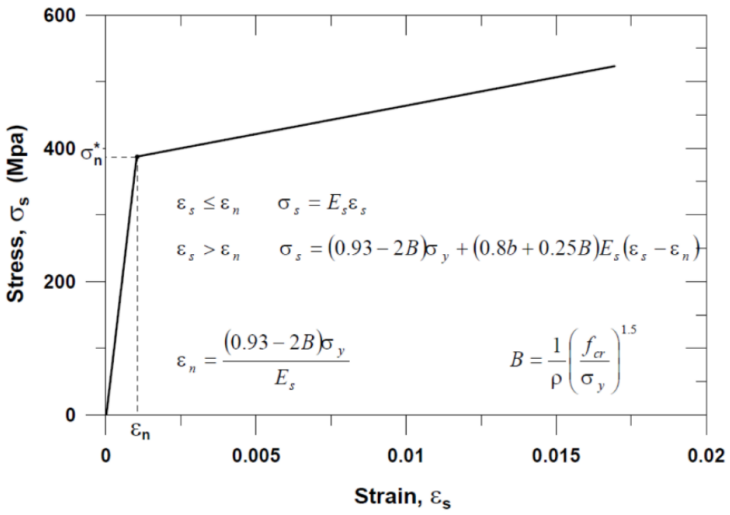


Figure 2.10. Average stress-strain relationship by Belarbi and Hsu (1994) for reinforcing bars embedded in concrete (Orakcal, 2004).

### 2.3.5. Biaxial Damage on Concrete

FSAM formulation also considers the cyclic damage effects on concrete under biaxial loading which is an important feature to cover in simulation of RC panel behavior. The cyclic damage is introduced by using a damage coefficient. The introduced damage coefficient is a cyclic strain history dependent parameter unlike the compression softening or tension stiffening coefficients which are fixed values for the whole strain history. Since this parameter is related to cyclic damage effects, it is not included in the formulation for concrete under monotonic loading.

Compressive strain history perpendicular to the compressive stress direction considered for the concrete influences the damage coefficient. Therefore, the damage coefficient is defined for biaxial loading case and is not applicable to uniaxial concrete constitutive behavior. The damage coefficient applied as a multiplier which softens the compressive stress-strain behavior of concrete. This effect is incorporated into FSAM formulation by using the empirical model proposed by Mansour et al. (2002). This model relates the peak compressive strain in concrete ($\varepsilon_c'$) to the maximum compressive strain perpendicular to the considered compression direction, ($\varepsilon_{\perp max}$).

## 2.4. Shear Aggregate Interlock on Crack Surfaces

In the original formulation of FSAM (Ulugtekin, 2010), shear aggregate interlock was enforced to be zero since principal stress direction is assumed to be fixed along the strut directions. Orakcal et al. (2012) introduced a simple friction-based constitutive model for shear aggregate interlock. Shear aggregate interlock model implemented into this formulation used elasto-plastic hysteresis loops and the contribution of clamping effect to the shear aggregate interlock capacity was not considered. However, Gullu (2019) introduced more robust models for shear aggregate interlock and dowel action, which also include cyclic degradation parameters. The more robust relationships used by Gullu (2019) are also used in this study and are described in the following paragraphs.

Vassilopoulou and Tassios (2003) defines a relationship between the slip along a crack surface and the shear stress by combining the frictional resistance along the crack surface and the resistance due to the clamping that develops on the reinforcing bars normal to the crack. Slip deformation at the crack surface is defined by multiplying the shear strain along that surface with the nominal crack spacing

$$\Delta_{crack} = \gamma_{crack}\, s \tag{2.20}$$

$$s = \frac{1}{\frac{sin\theta}{s_x} + \frac{cos\theta}{s_y}} \tag{2.21}$$

where $\Delta_{crack}$ is the slip deformation, $\gamma_{crack}$ is the shear strains along the crack surface, s is the nominal crack spacing while $s_x$ and $s_y$ represent the distance between horizontal and vertical reinforcing bars, respectively.

Since the clamping stress calculated by the Vassilopoulou and Tassios (2003) model exceeds the ACI 318-14, the shear capacity ($\tau_{crack,max}$) is defined by using a friction-based relationship which relates the concrete compressive stress perpendicular to the crack ($\sigma_{c\perp}$) and the smeared clamping stress of the reinforcing bar spanning the crack $\left((\rho f_y)_{\perp}\right)$ by using a friction coefficient ($\eta$). The shear capacity is

$$\tau_{crack,max} = \eta\left\{\sigma_{c\perp} + (\rho f_y)_{\perp}\right\}. \tag{2.22}$$

Vassilopoulou and Tassios (2003) is also used to define the stress vs. slip deformation stiffness of the envelope and the unloading and reloading paths. Originally, Vassilopoulou and Tassios (2003) suggested a 25% stress offset upon reloading to the unloading slip value from the envelope. However, this offset was not used in this implementation, for improving the numerical stability of the model under generalized slip histories.

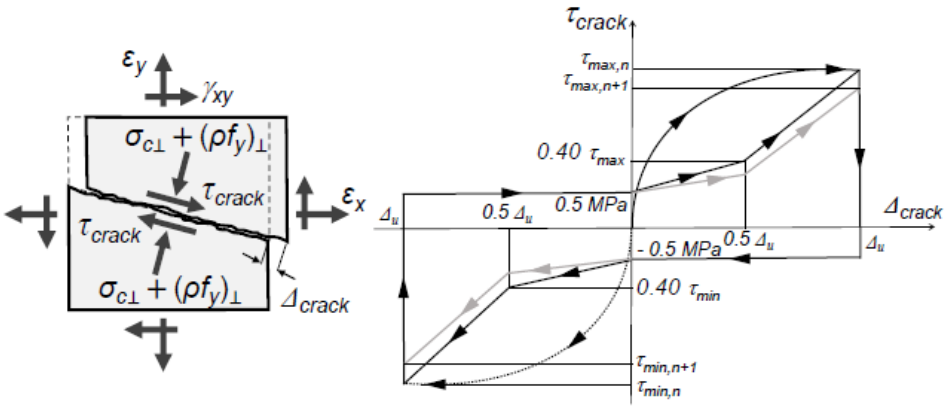


Figure 2.11. Shear aggregate interlock on crack surfaces (Gullu, 2019).

## 2.5. Dowel Action on Reinforcement

In this study, the effects of shear and tensile stresses along the cracks and dowel deformation perpendicular to the reinforcing bar direction are defined by a friction-based dowel action model by He and Kwan (2001). This constitutive model uses a smeared stress and strain approach to describe the dowel action on the reinforcing bars. However, the rules of the adopted origin-oriented model are modified according to the model proposed by Vassilopoulou and Tassios (2003).

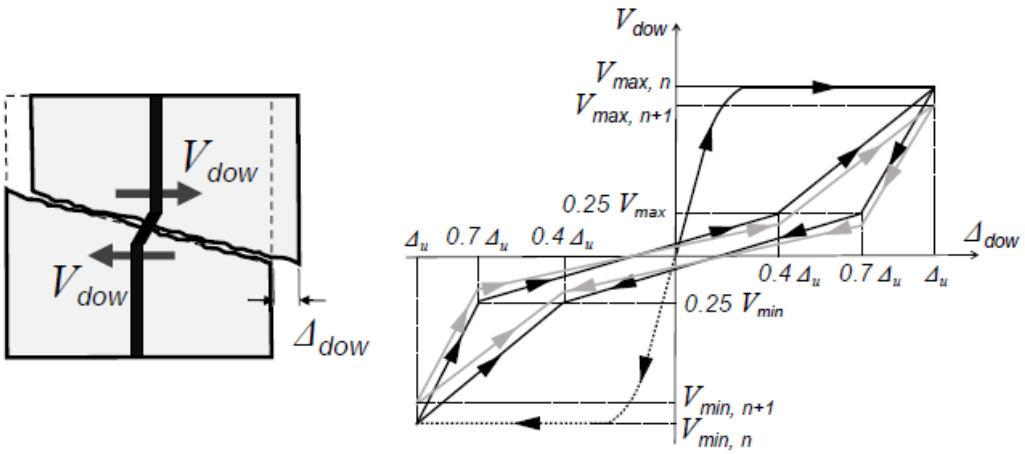


Figure 2.12. Dowel action behavior (Gullu, 2019).

The dowel forces corresponding to the dowel deformations for reinforcing bars are calculated according to this model. In addition, the rule of offsetting the force reloading curve

in Vassilopoulou and Tassios (2003) by 30% is omitted. Therefore, the maximum dowel force is defined as follows

$$V_{dow,max} = 1.30 d_{bar}^2 \sqrt{|f_c'| f_y}\ . \tag{2.23}$$

## 2.6. Cyclic Degradation Parameters

Cyclic degradation parameters in FSAM are defined by using Vassilopoulou and Tassios (2003) model modified according to Thermou et al. (2014). This model was incorporated into FSAM by Gullu (2019) and is also used in this study. The parameters defined by this model represent the degradation in interlock stresses and dowel forces under reversed cyclic loading and they are applicable to indeterminate slip deformation histories along the cracks. The Equations (2.24) and (2.25) are used to simulate these effects

$$\tau_{crack,deg} = 1 - 0.05\alpha \sqrt{\frac{\sum \Delta/|\Delta_{max}|+1}{4}} \left(\frac{f_c'}{\sigma_{c\perp}}\right)^{1/2} \left(\frac{|\Delta_{max}|}{\Delta_u}\right)^{1/3} \tag{2.24}$$

$$V_{dow,deg} = 1 - \alpha \frac{1}{7} \sqrt{\frac{\sum \Delta/\Delta_{max}+1}{4}} \tag{2.25}$$

where $\sum \Delta$ represents the cumulative slip deformation while $\Delta_{max}$ is the maximum slip deformation along the slip reversals. $\Delta_u$ is defined as 2mm according to Vassilopoulou and Tassios (2003). $\alpha$ is the degradation parameter and taken as 1.0.

# 3. FINITE ELEMENT MODEL DESCRIPTION

## 3.1. General Finite Element Model Formulation

FSAFE model formulation combines quadrilateral panel elements which have two translational degrees of freedom per node through a direct stiffness approach. The nodal numbers increase in the clockwise direction. Since membrane elements does not have out-of-plane DOFs, only in-plane behavior is considered. The nodal numbering of a membrane element is shown in Figure 3.1.

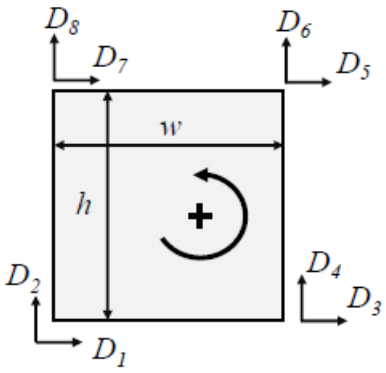


Figure 3.1. Displacement along nodal DOFs in FSAFE model (Gullu, 2019).

For a finite element, displacements at the degrees of freedom can be obtained from equilibrium equations and shape functions. Using these known displacements, the average strain field can be calculated. The kinematic transformation for the average strain field

$$\begin{Bmatrix} \varepsilon_x \\ \varepsilon_y \\ \gamma_{xy} \end{Bmatrix} = \begin{bmatrix} -1/2w & 0 & 1/2w & 0 & 1/2w & 0 & -1/2w & 0 \\ 0 & -1/2h & 0 & -1/2h & 0 & 1/2h & 0 & 1/2h \\ -1/2h & -1/2w & -1/2h & 1/2w & 1/2h & 1/2w & 1/2h & -1/2w \end{bmatrix} \begin{Bmatrix} D_1 \\ D_2 \\ D_3 \\ D_4 \\ D_5 \\ D_6 \\ D_7 \\ D_8 \end{Bmatrix} \quad (3.1)$$

where w represents the width of the finite element while h represents the height of the finite element. Using the average strain field, FSAM constitutive model transforms them into average stress fields and tangent stiffness matrices for each finite element. The 8x1 restoring force vector is obtained by multiplying the stress values with the thickness and the half of the height of the finite elements. These restoring (internal) force vectors are combined in a similar manner to the global stiffness assembly procedure through following a numbering scheme. The restoring force vector for a single element is

$$F_1 = -\sigma_x \frac{ht}{2} - \tau_{xy} \frac{wt}{2} \tag{3.2}$$

$$F_2 = -\sigma_y \frac{wt}{2} - \tau_{xy} \frac{ht}{2} \tag{3.3}$$

$$F_3 = \sigma_x \frac{ht}{2} - \tau_{xy} \frac{wt}{2} \tag{3.4}$$

$$F_4 = -\sigma_y \frac{wt}{2} + \tau_{xy} \frac{ht}{2} \tag{3.5}$$

$$F_5 = \sigma_x \frac{ht}{2} + \tau_{xy} \frac{wt}{2} \tag{3.6}$$

$$F_6 = \sigma_y \frac{wt}{2} + \tau_{xy} \frac{ht}{2} \tag{3.7}$$

$$F_7 = -\sigma_x \frac{ht}{2} + \tau_{xy} \frac{wt}{2} \tag{3.8}$$

$$F_8 = \sigma_y \frac{wt}{2} - \tau_{xy} \frac{ht}{2}. \tag{3.9}$$

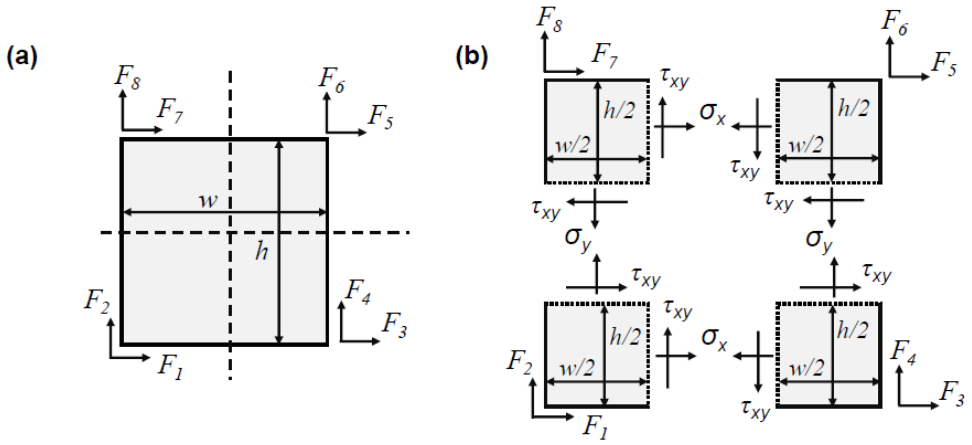


Figure 3.2. FSAFE model element: (a) forces along nodal DOF, (b) equilibrium of nodal forces and average stresses (Gullu, 2019).

Using the partial derivatives of the restoring forces, the tangent stiffness matrix [K] can be obtained as follows

$$[K] = \begin{bmatrix} K_{11} & K_{12} & \cdots & K_{18} \\ K_{21} & K_{22} & \cdots & K_{28} \\ \vdots & \vdots & \ddots & \vdots \\ K_{81} & K_{82} & \cdots & K_{88} \end{bmatrix} = \begin{bmatrix} \frac{\partial F_1}{\partial D_1} & \frac{\partial F_1}{\partial D_2} & \cdots & \frac{\partial F_1}{\partial D_8} \\ \frac{\partial F_2}{\partial D_1} & \frac{\partial F_2}{\partial D_2} & \cdots & \frac{\partial F_2}{\partial D_8} \\ \vdots & \vdots & \ddots & \vdots \\ \frac{\partial F_8}{\partial D_1} & \frac{\partial F_8}{\partial D_2} & \cdots & \frac{\partial F_8}{\partial D_8} \end{bmatrix}. \quad (3.10)$$

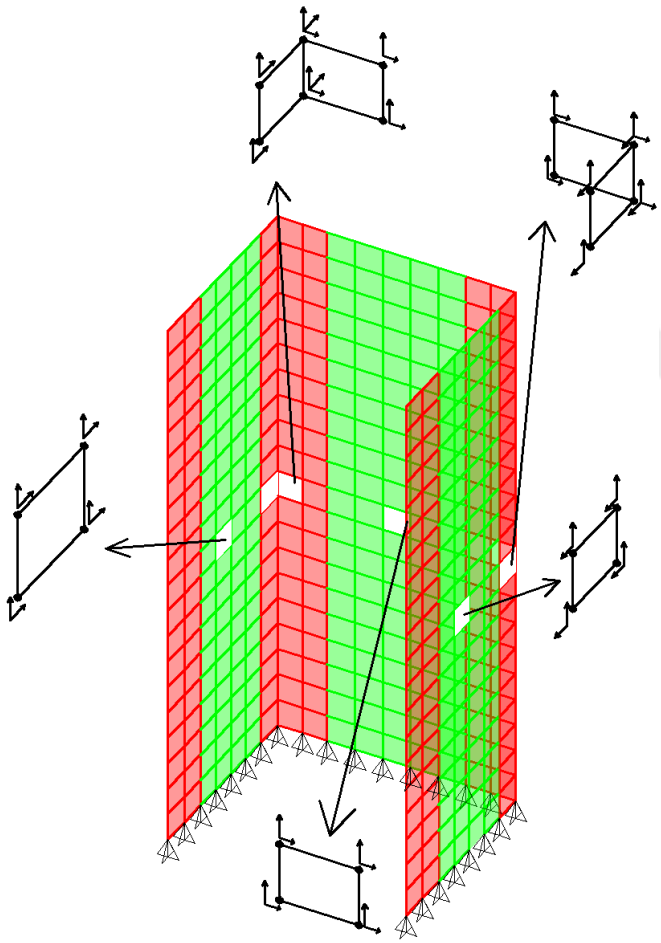

Figure 3.3. Model meshing for a U-shaped reinforced concrete wall.

Since a direct stiffness approach is used in the assembly of four-node rectangular elements, numbering the nodes is an important part of the combination. The local stiffness matrices of each element are combined into a global stiffness matrix for the wall by

superposing overlapping DOFs within the global stiffness matrix. An illustration of nodal connectivity for the U-shaped walls are shown in Figure 3.3. The given example has 48 degrees of freedom which indicates a 48x48 stiffness matrix. The numbering of the elements is given in Figure 3.4.

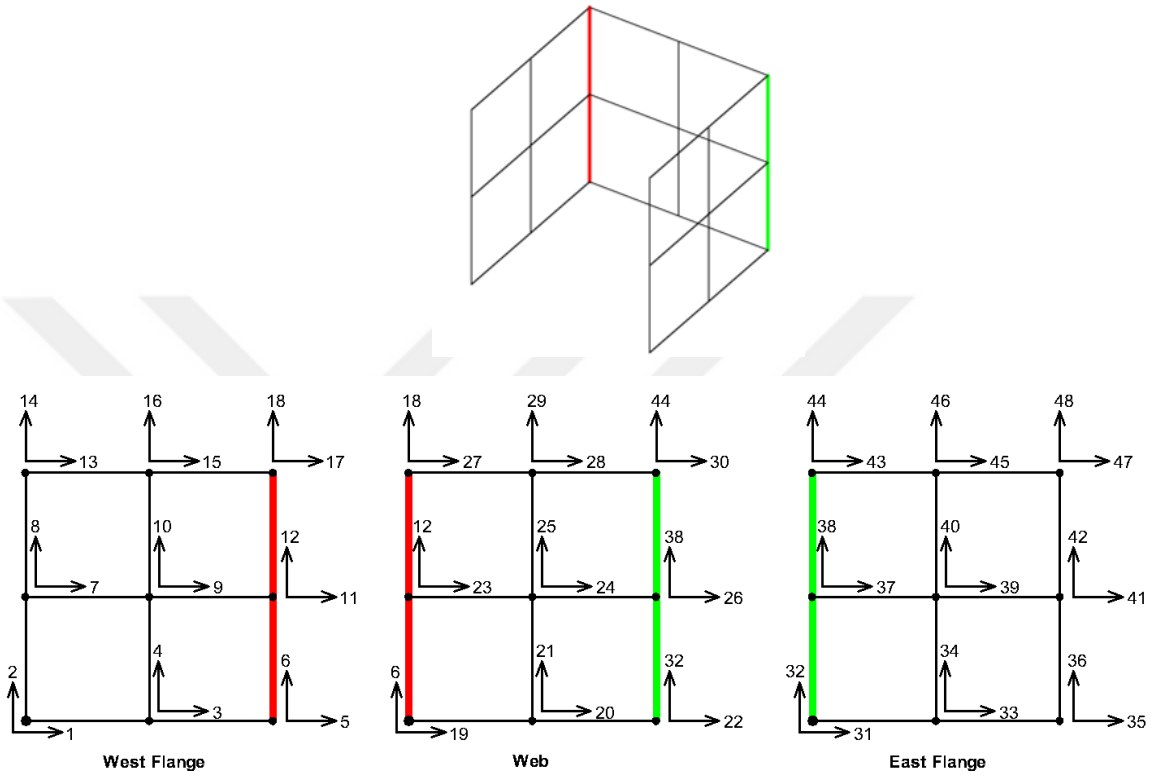


Figure 3.4. Global DOFs in a U-shaped wall.

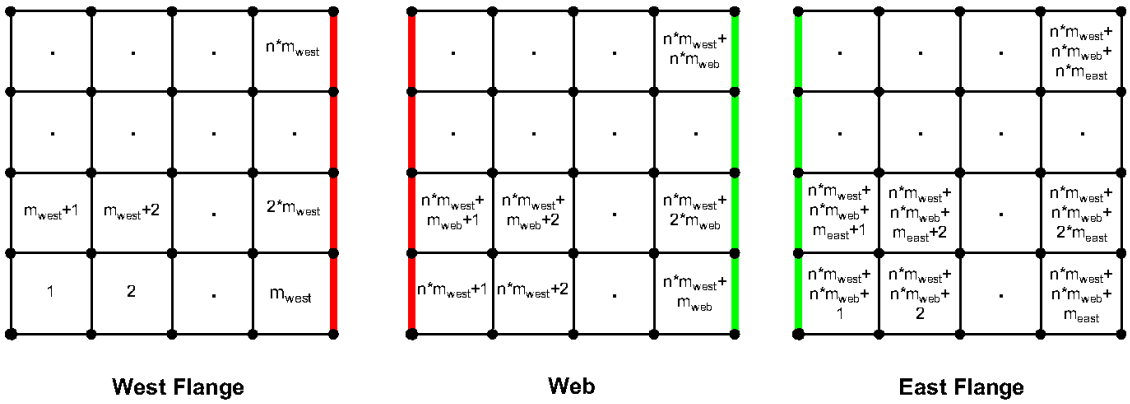


Figure 3.5. Numbering of the model elements.

### 3.2. Body Constraints and Supports

The walls modeled in this study are connected to their foundations with shear keys, and it was experimentally observed that the sliding does not have a considerable effect on the total lateral displacement. Thus, the displacements at the supports are restrained (i.e. equal to zero) to represent the rigid (pin-supported) wall-foundation connection in the finite element model nodes. Equilibrium equations are solved by partitioning the equations to calculate the support reactions using the known displacements.

Body constraints for U-shaped RC walls are defined to represent the actual behavior of the test units used to validate the model. The thickness of the wall head of each test unit was increased to create a collar. Collars restrain the twisting only partially introducing bi-moments at the story levels. The body constraint in the FE model is defined such that to restrain the twisting of the wall head partially while generating bi-directional moments at the story levels. The DOFs at the top of the wall are subjected to equal horizontal displacements in the applied strain field direction.

The effect of the defined body constraints is introduced into the formulation by using a transformation matrix [T]. After applying the body constraint at the wall top, the change in the numbering of DOFs of the wall model is depicted in Figure 3.6 First, the 38x1 displacement vector is transformed into 48x1 displacement vector using the transformation matrix, [T]. The 38x38 stiffness matrix, 38x1 restoring force vector, global stiffness matrix, the global internal force vector, and the displacement vector are derived with the following equations

$$[T]_{48x38} = \begin{array}{c} \\ 1 \\ 2 \\ \vdots \\ 13 \\ 14 \\ 15 \\ 16 \\ 17 \\ 18 \\ \vdots \\ 27 \\ 28 \\ 29 \\ 30 \\ \vdots \\ 43 \\ 44 \\ 45 \\ 46 \\ 47 \\ 48 \end{array} \begin{array}{c} \begin{array}{ccccccccc} 1 & 2 & \dots & 33 & 34 & 35 & 36 & 37 & 38 \end{array} \\ \begin{bmatrix} 1 & 0 & \dots & 0 & 0 & 0 & 0 & 0 & 0 \\ 0 & 1 & \dots & 0 & 0 & 0 & 0 & 0 & 0 \\ \vdots & \vdots & \ddots & \vdots & \vdots & \vdots & \vdots & \vdots & \vdots \\ 0 & 0 & \dots & 0 & 0 & 1 & 0 & 0 & -b \\ 0 & 0 & \dots & 0 & -b & 0 & 0 & c_g - 2b & 0 \\ 0 & 0 & \dots & 0 & 0 & 1 & 0 & 0 & -b \\ 0 & 0 & \dots & 0 & -b & 0 & 0 & c_g - b & 0 \\ 0 & 0 & \dots & 0 & 0 & 1 & 0 & 0 & -b \\ 0 & 0 & \dots & 0 & -b & 0 & 0 & c_g & 0 \\ \vdots & \vdots & \vdots & \vdots & \vdots & \vdots & \vdots & \vdots & \vdots \\ 0 & 0 & \dots & 1 & 0 & 0 & 0 & 0 & -c_g \\ 0 & 0 & \dots & 1 & 0 & 0 & 0 & 0 & -c_g \\ 0 & 0 & \dots & 0 & 0 & 0 & 0 & c_g & -c_g \\ 0 & 0 & \dots & 1 & 0 & 0 & 0 & 0 & -c_g \\ \vdots & \vdots & \vdots & \vdots & \vdots & \vdots & \vdots & \vdots & \vdots \\ 0 & 0 & \dots & 0 & 0 & -1 & 0 & 0 & -b \\ 0 & 0 & \dots & 0 & b & 0 & 0 & 0 & 0 \\ 0 & 0 & \dots & 0 & 0 & -1 & 0 & 0 & -b \\ 0 & 0 & \dots & 0 & b & 0 & 0 & 0 & 0 \\ 0 & 0 & \dots & 0 & 0 & -1 & 0 & 0 & -b \\ 0 & 0 & \dots & 0 & b & 0 & 0 & 0 & 0 \end{bmatrix} \end{array} \tag{3.11}$$

$$[K]_{48x48}x\{D\}_{48x1} = \{F\}_{48x1} \tag{3.12}$$

$$[K]_{48x48}x[T]_{48x38}x\{D\}_{38x1} = \{F\}_{48x1} \tag{3.13}$$

$$[T]^T_{48x38}x[K]_{48x48}x[T]_{48x38}x\{D\}_{38x1} = [T]^T_{48x38}x\{F\}_{48x1} \tag{3.14}$$

$$[K]_{38x38}x\{D\}_{38x1} = \{F\}_{38x1}. \tag{3.15}$$

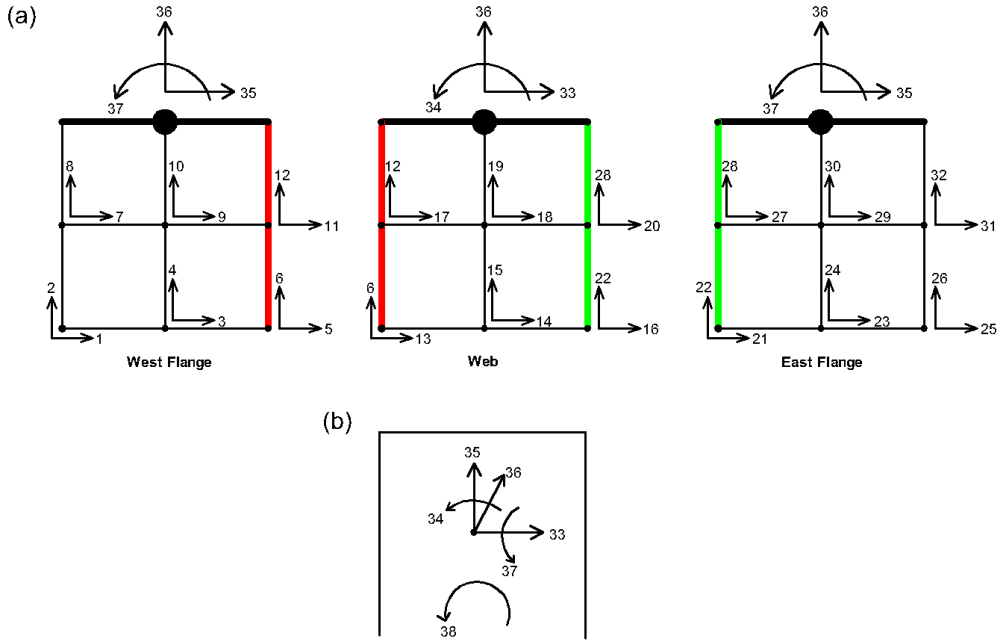


Figure 3.6. U-shaped wall after assigning body constraints: (a) side view, (b) top view.

### 3.3. Nonlinear Analysis Strategy for Biaxial Loading

The displacement-based nonlinear solution technique which was proposed by Clarke and Hancock (1990) is used in this study as the baseline nonlinear analysis solution strategy. However, it was extended to allow displacement-controlled analysis under bi-directional lateral loading, as described in this section. The reason for using a displacement-based solution strategy is to be able to compare model responses with the displacement-controlled test results. Since the U-shaped walls are subjected to biaxial loading, the chosen nonlinear solution strategy is applied in both directions and consists of two stages named load incrementation and equilibrium. At the load incrementation stage (denoted by "i") the applied displacement is increased while at the equilibrium stage (denoted by "j"), iterations are performed to reach the equilibrium between internal and external forced within a specified error margin.

First incrementation stage begins with the definition of tangent stiffness matrix $[K_I]_i$ from the geometric and material properties of the wall. Then, the reference external load $\{F_I\}_i$ is defined depending on the normalized external load vector. For example, if biaxial loads are applied to the last two DOFs of n number of DOFs

$$\{F_{I1}\}_i = \begin{Bmatrix} 0 \\ 0 \\ \vdots \\ 1 \\ 0 \end{Bmatrix}, \quad \{F_{I2}\}_i = \begin{Bmatrix} 0 \\ 0 \\ \vdots \\ 0 \\ 1 \end{Bmatrix}. \tag{3.16}$$

Using the tangent stiffness matrix and applied loads, tangent displacement vectors are calculated

$$\{\delta_{I1}\}_i = [K_I]_i^{-1}\{F_{I1}\}_i \tag{3.17}$$

$$\{\delta_{I2}\}_i = [K_I]_i^{-1}\{F_{I2}\}_i. \tag{3.18}$$

The orientation of displacements is decided by using the tangent displacement vectors. Thus, it is not important how large or small are the displacement vectors. Reference displacement vector $\{b_n\}$ is a vector of zeros except at the node along which the displacement is imposed. Again, applying displacement along the last two nodes, $\{b_n\}$ vectors become

$$\{b_{n1}\} = \begin{Bmatrix} 0 \\ 0 \\ \vdots \\ 1 \\ 0 \end{Bmatrix}, \quad \{b_{n2}\} = \begin{Bmatrix} 0 \\ 0 \\ \vdots \\ 0 \\ 1 \end{Bmatrix}. \tag{3.19}$$

The next step is to calculate the initial load increment $\Delta\lambda_i^{j=1}$

$$\{\Delta\lambda_{i,1}\}^{j=1} = (\{b_{n1}\}^T \{\delta_{I1}\}_i)\Delta\delta_{n1} + (\{b_{n1}\}^T\{\delta_{I2}\}_i)\Delta\delta_{n2} \tag{3.20}$$

$$\{\Delta\lambda_{i,2}\}^{j=1} = (\{b_{n2}\}^T \{\delta_{I1}\}_i)\Delta\delta_{n1} + (\{b_{n2}\}^T\{\delta_{I2}\}_i)\Delta\delta_{n2} \tag{3.21}$$

where $\Delta\delta_{n1}$ and $\Delta\delta_{n2}$ are the displacement increments in each direction of the biaxial loading. The corresponding initial displacement increment is obtained from the initial load increment with the following expression

$$\{\Delta\delta\}_i^{j=1} = \{\Delta\lambda_{i,1}\}^{j=1}\{\delta_{I1}\}_i + \{\Delta\lambda_{i,2}\}^{j=1}\{\delta_{I2}\}_i. \tag{3.22}$$

At the end of the preceding load phase, the total displacement and updated load levels in each direction are calculated as follows

$$\{\delta\}_i^{j=1} = \{\delta\}_{i-1} - \{\Delta\delta\}_i^{j=1} \tag{3.23}$$

$$\lambda_{i,1}^{j=1} = \lambda_{(i-1),1} + \left\{\Delta\lambda_{i,1}\right\}^{j=1} \tag{3.24}$$

$$\lambda_{i,2}^{j=1} = \lambda_{(i-1),2} + \left\{\Delta\lambda_{i,2}\right\}^{j=1}. \tag{3.25}$$

Multiplying the external load vector with the scalar $\lambda$, the external force vector ($F_{ext}$) is obtained as

$$\{F_{ext}\}_i^{j=1} = \lambda_{i,1}^{j=1}\{F_{I1}\}_i + \lambda_{i,2}^{j=1}\{F_{I2}\}_i. \tag{3.26}$$

The unbalanced force is calculated from the difference of the internal and external forces as

$$\{F_{unb}\}_i^{j=1} = \{F_{int}\}_i^{j=1} - \{F_{ext}\}_i^{j=1}. \tag{3.27}$$

As previously mentioned, the iterations are performed within a tolerance. If any term in the unbalanced force vector exceeds the tolerance, iterations within the load step are required. The iterations begin with the calculation of the residual displacement increment

$$\{\Delta\delta_R\}_i^j = \frac{\{F_{unb}\}_i^{j-1}}{[K_I]_i} \tag{3.28}$$

$$\left\{\Delta\lambda_{i,1}\right\}^j = (\{b_{n1}\}^T\{\delta_{I1}\}_i)(-\{b_{n1}\}^T\{\Delta\delta_R\}_i^j) + (\{b_{n1}\}^T\{\delta_{I2}\}_i)(-\{b_{n2}\}^T\{\Delta\delta_R\}_i^j) \tag{3.29}$$

$$\left\{\Delta\lambda_{i,2}\right\}^j = (\{b_{n2}\}^T\{\delta_{I1}\}_i)(-\{b_{n1}\}^T\{\Delta\delta_R\}_i^j) + (\{b_{n2}\}^T\{\delta_{I2}\}_i)(-\{b_{n2}\}^T\{\Delta\delta_R\}_i^j) \tag{3.30}$$

$$\{\Delta\delta\}_i^j = \left\{\Delta\lambda_{i,1}\right\}^j\{\delta_{I1}\}_i + \left\{\Delta\lambda_{i,2}\right\}^j\{\delta_{I2}\}_i + \{\Delta\delta_R\}_i^j. \tag{3.31}$$

From the nodal displacement and load increments, the displacement vector, and the scalars to calculate the external force vector are computed by

$$\{\delta\}_i^j = \{\delta\}_i^{j-1} - \{\Delta\delta\}_i^j \tag{3.32}$$

$$\lambda_{i,1}^j = \lambda_{i,1}^{j-1} + \{\Delta\lambda_{i,1}\}^j \tag{3.33}$$

$$\lambda_{i,2}^j = \lambda_{i,2}^{j-1} + \{\Delta\lambda_{i,2}\}^j. \tag{3.34}$$

The external load is calculated in the same way in the equilibrium cycles as in the load increment cycles. Again, the unbalanced force is obtained through the difference of internal and external forces

$$\{F_{ext}\}_i^j = \lambda_{i,1}^j\{F_{I1}\}_i + \lambda_{i,2}^j\{F_{I2}\}_i \tag{3.35}$$

$$\{F_{unb}\}_i^j = \{F_{int}\}_i^j - \{F_{ext}\}_i^j. \tag{3.36}$$

If the unbalanced force is smaller than the specified error margin, the equilibrium cycles are stopped, and another load increment cycle begins. If the unbalanced force is larger than the tolerance, the equilibrium cycles are repeated until the error is within the limits. When the eventual error is smaller than the limit, the step is assumed to converge.

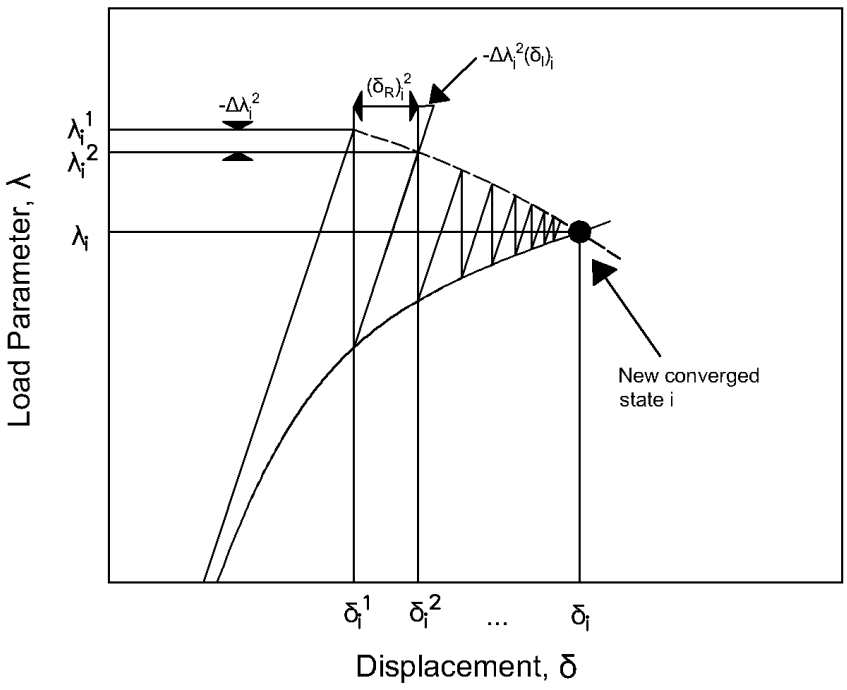


Figure 3.7. The iterative nonlinear analysis solution strategy.

# 4. EXPERIMENTAL VALIDATION OF THE MODEL FOR U-SHAPED WALLS

## 4.1. Test Units

For the experimental verification of the model, test results for four U-shaped walls subjected to biaxial loading are obtained from two separate testing campaigns in the literature. The experimental results consider the effects of a variety of parameters such as wall thickness, axial load level, reinforcement layout, and loading history.

Half-scale elevator shaft prototypes TUA and TUB tested by Beyer et al. (2008) are the first two test units utilized for model verification. The difference between the test units in this testing program are the different wall thicknesses. The wall thickness for TUA is 0.15 m while the wall thickness for TUB is 0.10 m. The same constant axial load of 780 kN is applied to both test units close to the center of inertia of the gross concrete sections. Approximately the same area of longitudinal reinforcement and the same longitudinal reinforcement are used for the two walls. 6 shear keys are used as a measure against shear sliding. The shear span parallel to the flanges is 2.95m while the shear span parallel to the web is 3.35m. Figure 4.1 shows the details of TUA and TUB.

The concrete cylinder strength for TUA was tested as 77.9 MPa while the cylinder strength of concrete for TUB was 54.7 MPa. The yield strengths for the reinforcing bars ranged from 471 to 518 MPa. The loading history followed mainly a pattern at each drift level where the walls are loaded parallel to the web first and then the walls loaded parallel to the flanges. The third step was a sweep motion which is similar to a rounded clover leaf pattern. The last step was to apply the displacement field in the diagonal direction. This pattern of loading is followed until the failure of the wall specimens. Some of the longitudinal reinforcing bars of TUA was ruptured and led to its failure. For TUB, the compression diagonals were crushed, and this was recorded as its failure. The test setup, loading history, and the instrumentation of the test units are shown in Figure 4.2-4.4.

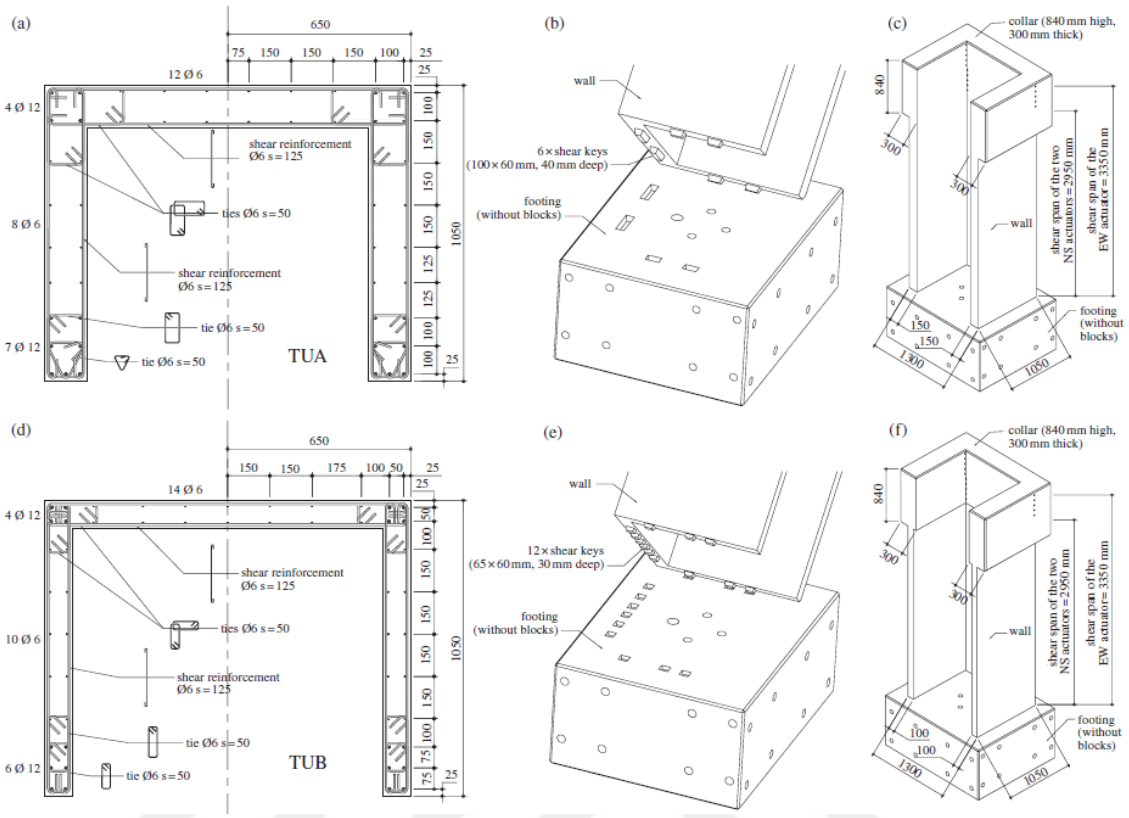


Figure 4.1. Cross-sections of the walls and reinforcement layout: (a) TUA, (b) TUB (Beyer et al., 2008).

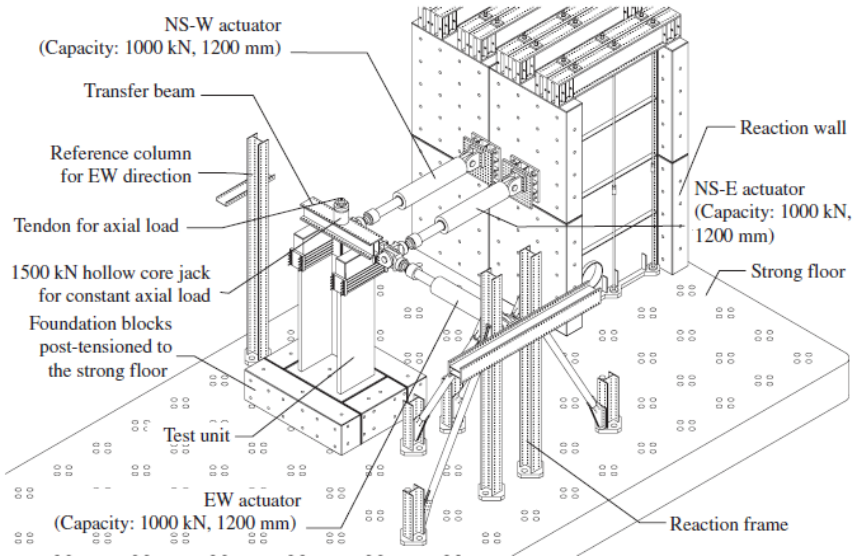


Figure 4.2. Test setup (Beyer et al., 2008).

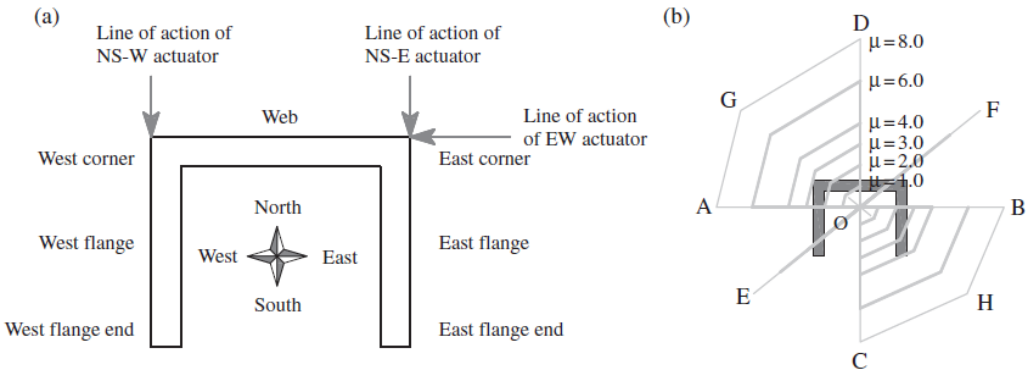


Figure 4.3. (a) Name of the wall sections, (b) target top displacement (Beyer et al., 2008).

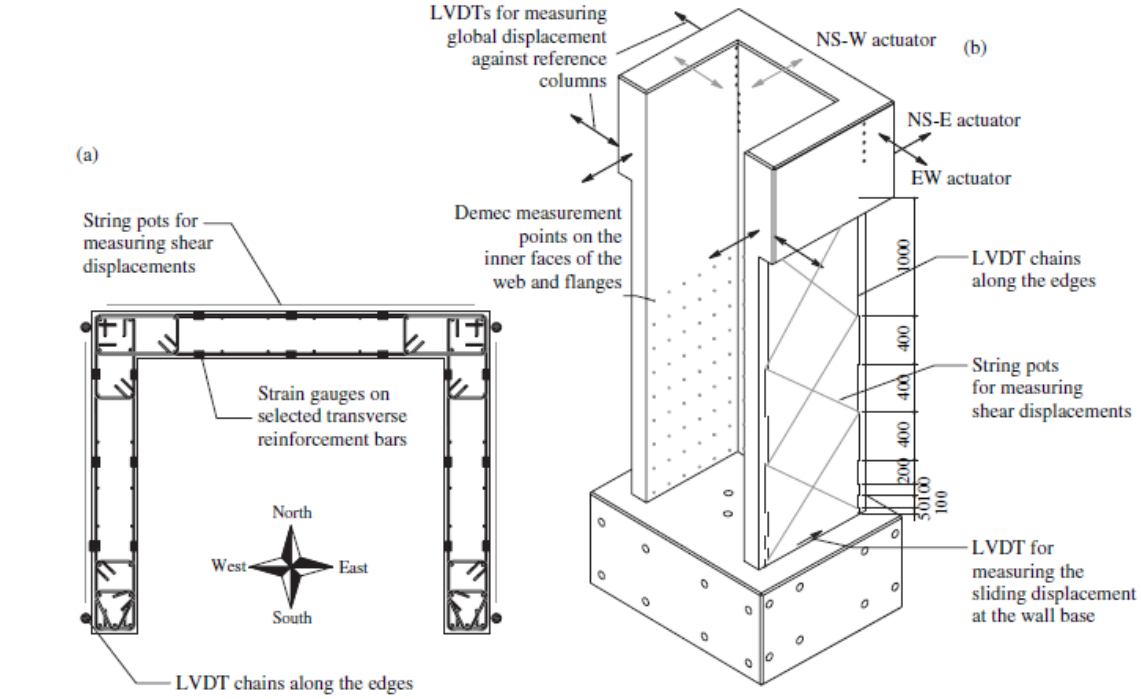


Figure 4.4. Instrumentation of TUA and TUB (Beyer et al., 2008).

The other two wall sections are a continuation of the experimental program by Beyer et al. (2008). Changes in instrumentation, loading history, and reinforcement layout were made. The test units tested by Constantin and Beyer (2016) have the same dimensions as TUB from the previous testing program. Same longitudinal reinforcement was used for both specimens, TUC and TUD. They differed by the applied level of axial load, which is $0.06A_g f_c'$ for TUC and $0.15A_g f_c'$ for TUD, and their shear reinforcement. Also, TUD had

a ~25% more shear reinforcement than TUC. The vertical reinforcement is concentrated at the boundary elements at one flange and uniformly distributed at the other flange to investigate the effect of reinforcement layout.

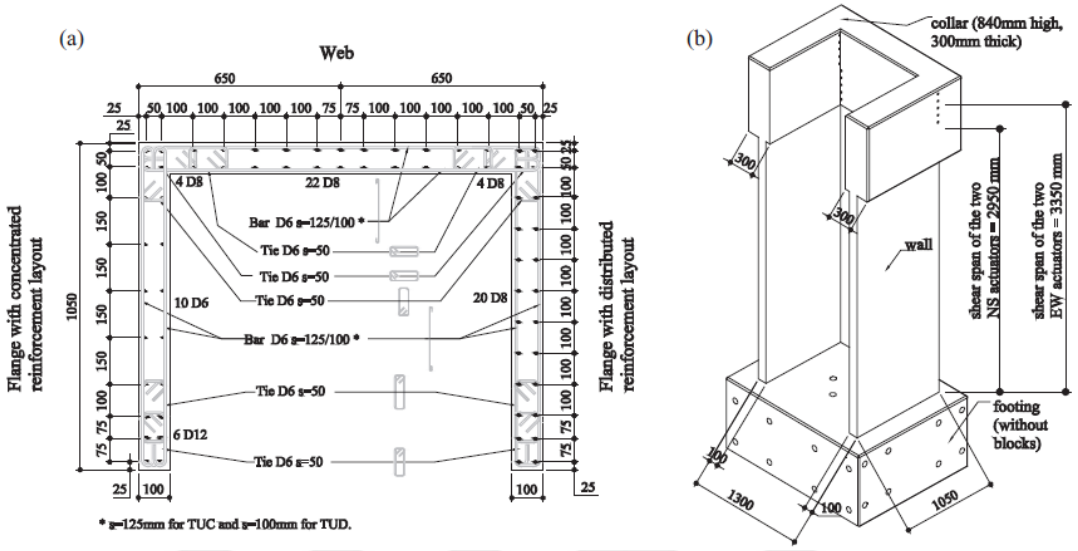


Figure 4.5. TUC and TUD: (a) cross-section and reinforcement layout, (b) elevation (Constantin and Beyer, 2016).

The compressive strength of the concrete was tested as 42 MPa for TUC and 41.5 MPa MPa for and TUD. Modulus of elasticity and shear strength for concrete were also very similar for both test units. Modulus of elasticity for concrete was 31.6 and 30.3 GPa and concrete shear strength was 3.2 and 3.0 MPa for TUC and TUD, respectively. The yield strength for the reinforcing bars ranged from 492 MPa to 563 MPa while the ultimate strength was between 623 and 663 MPa.

The test setup was the same as in Beyer et al. (2008). The LVDT chains were again the same with the previous program while a large number for LEDs were glued to the walls unlike TUA and TUB. The loading history up to 1% drift mainly followed a similar pattern where at each drift level, the test units were loaded in the orientation of the web and flanges and in diagonal directions for one reversed cycle while after 1% drift, reversed cycles are repeated at each drift level in diagonal directions.

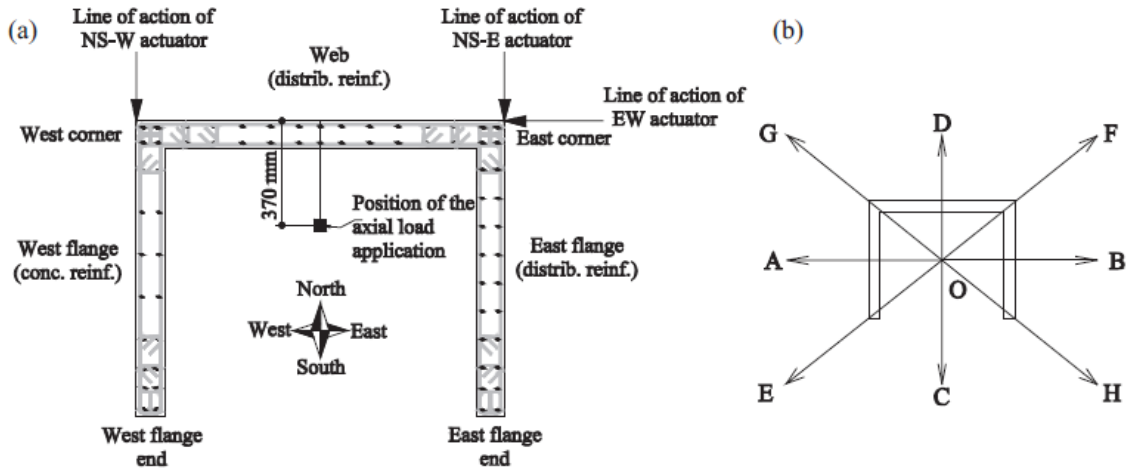


Figure 4.6. (a) loading points on the wall segment ; (b) the loading positions (Constantin and Beyer, 2016).

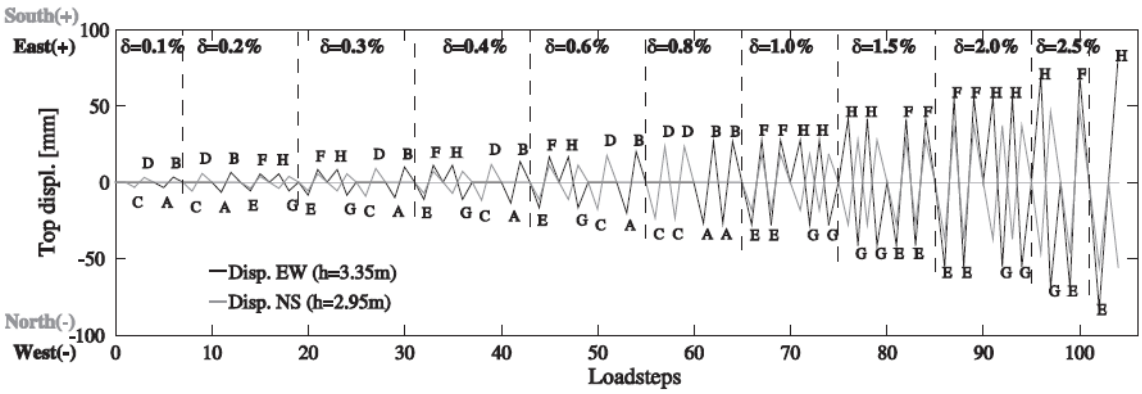


Figure 4.7. TUC loading history (Constantin and Beyer, 2016).

TUC failed because of out-of-plane buckling and compression failure of the west flange during an E-F diagonal direction loading. After the failed west flange, loading in E-F direction was stopped and the wall was loaded in the other diagonal direction H-G which led to the compression failure of the east flange. TUD failed due to an explosive compression failure of the east flange under diagonal loading in H-G direction. Upon continuing the loading in E-F direction, concrete crushing of the web occurred.

## 4.2. Calibration of the Model for the Wall Specimens

Each wall specimen's geometric and material properties are considered for calibration of the analytical model. First, the wall specimen is divided into square-like rectangles in horizontal and vertical direction. Then, the input material parameters such as vertical and transverse reinforcement ratios, concrete strength, reinforcing bar yield strength, etc. are defined to calibrate the constitutive model.

For all four wall specimens, each flange is divided into 7 segments and web is divided into 9 segments in the horizontal direction and both flanges, and web is divided into 20 segments in the vertical direction. Thus, each wall is divided into 460 rectangular elements. All rectangular elements have almost equal height and width. Number of meshes in horizontal and vertical directions together with number of boundary and web elements used at each part of the wall are shown in Table 4.1.

Table 4.1. Number of meshes for each wall specimen.

| Experimental Program | Test Unit | | Number of Meshes | | |
|---|---|---|---|---|---|
| | | | Horizontal Meshes (m) | | Vertical Meshes (n) |
| | | | Boundary | Web | |
| Beyer et al. (2008) | TUA | Web | 4 | 5 | 20 |
| | | Flanges | 4 | 3 | 20 |
| | TUB | Web | 2 | 7 | 20 |
| | | Flanges | 3 | 4 | 20 |
| Constantin and Beyer (2016) | TUC | Web | 4 | 5 | 20 |
| | | Flanges | 3 | 4 | 20 |
| | TUD | Web | 4 | 5 | 20 |
| | | Flanges | 3 | 4 | 20 |

Constitutive model parameters were adjusted to match the tested properties or represented by well-known material models in the literature. Since experimental results used for the model verification in this part provided only the compressive strength for cylinder specimens, not stress-strain relationships, the monotonic stress-strain relationship for the ascending part of the unconfined concrete compressive strength curve is defined according to Chang and Mander (1994). The ascending part of the confined concrete stress-strain envelopes are defined by using the Mander et al. (1998). The descending slope of both

unconfined and confined concrete stress-strain envelopes are matched with the descending slope of the Saatcioglu and Razvi Model (1992). More details about the parameters $f_c'$ (concrete compressive strength), $E_c$ (concrete elastic modulus), $\varepsilon_c'$ (strain at the peak compressive stress), $r$ (parameter to define the shape of the envelope), $x_{crn}$ (normalized critical strain value) are shown in Table 4.2.

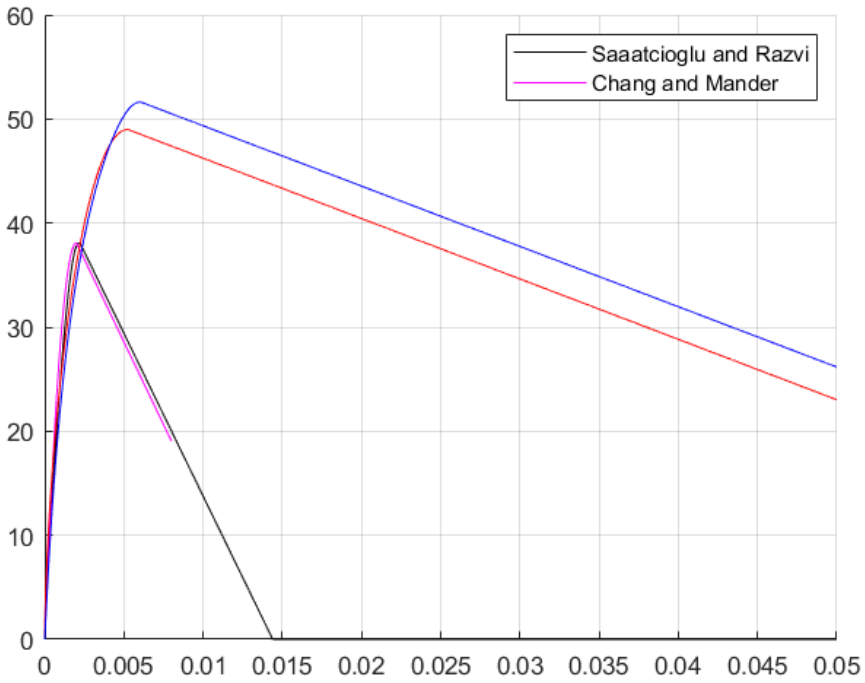


Figure 4.8. Calibrated unconfined and confined concrete models for the web of TUC.

Concrete tensile stress is defined by $f_t = 0.31\sqrt{f_c'}$. The strain at the peak tensile stress is chosen as 0.00008 as recommended by Belarbi and Hsu (1994). The shape post-cracking stress-strain curve is chosen such that it represents the effects of tension stiffening proposed by Belarbi and Hsu (1994). More details about the tensile strength of concrete ($f_t$), elastic modulus ($E_c$), strain at the peak tensile stress ($\varepsilon_t$), shape parameter for the tension envelope ($r_t$) and normalized critical strain ($x_{crp}$) are given in Table 4.3.

Table 4.2. Parameters for the calibration of the concrete model.

| Test Unit | | | $f_c'$ (MPa) | $E_c$ (MPa) | $\varepsilon_c$ | r | $x_{crn}$ |
|---|---|---|---|---|---|---|---|
| TUA | Web | Unconfined | 77.9 | 42225 | 0.0026 | 13.2 | 1.020 |
| | | Confined | 81.0 | 42848 | 0.0031 | 13.8 | 1.009 |
| | Flanges | Confined | 93.6 | 45241 | 0.0052 | 16.2 | 1.013 |
| | | Unconfined | 77.9 | 42225 | 0.0026 | 13.2 | 1.020 |
| | | Confined (web-flange intersection) | 83.6 | 43350 | 0.0035 | 14.3 | 1.010 |
| TUB | Web | Unconfined | 54.7 | 36982 | 0.0024 | 8.7 | 1.032 |
| | | Confined | 62.5 | 38885 | 0.0043 | 10.1 | 1.013 |
| | Flanges | Confined | 70.5 | 40675 | 0.0058 | 11.7 | 1.023 |
| | | Unconfined | 54.7 | 36982 | 0.0024 | 8.7 | 1.032 |
| | | Confined (web-flange intersection) | 61.8 | 38711 | 0.0039 | 10.1 | 1.012 |
| TUC | Web | Unconfined | 42.0 | 33494 | 0.0022 | 6.2 | 1.059 |
| | | Confined | 53.9 | 36783 | 0.0053 | 8.5 | 1.040 |
| | West Flange | Confined | 58.3 | 37879 | 0.0065 | 9.4 | 1.040 |
| | | Unconfined | 42.0 | 33494 | 0.0022 | 6.2 | 1.059 |
| | | Confined (web-flange intersection) | 53.1 | 36565 | 0.0051 | 8.4 | 1.033 |
| | East Flange | Confined | 57.4 | 37647 | 0.0063 | 9.2 | 1.038 |
| | | Unconfined | 42.0 | 33494 | 0.0022 | 6.2 | 1.059 |
| | | Confined (web-flange intersection) | 53.8 | 36761 | 0.0053 | 8.5 | 1.036 |
| TUD | Web | Unconfined | 41.5 | 33344 | 0.0022 | 6.1 | 1.051 |
| | | Confined | 52.8 | 36499 | 0.0052 | 8.3 | 1.033 |
| | West Flange | Confined | 57.8 | 37752 | 0.0065 | 9.3 | 1.043 |
| | | Unconfined | 41.5 | 33344 | 0.0022 | 6.1 | 1.051 |
| | | Confined (web-flange intersection) | 47.0 | 34947 | 0.0037 | 7.2 | 1.018 |
| | East Flange | Confined | 55.0 | 37062 | 0.0058 | 8.7 | 1.037 |
| | | Unconfined | 41.5 | 33344 | 0.0022 | 6.1 | 1.051 |
| | | Confined (web-flange intersection) | 48.1 | 35238 | 0.0039 | 7.4 | 1.020 |

Table 4.3. Parameters for concrete in tension.

| Test Unit | $f_t$ (MPa) | $E_c$ (MPa) | $\varepsilon_t$ | $r_t$ | $x_{crp}$ |
|---|---|---|---|---|---|
| TUA | 2.8 | 42225 | 0.00008 | 1.22 | 10000 |
| TUB | 2.3 | 36982 | 0.00008 | 1.23 | 10000 |
| TUC | 2.0 | 33494 | 0.00008 | 1.23 | 10000 |
| TUD | 2.0 | 33344 | 0.00008 | 1.24 | 10000 |

The stress-strain relationship of the reinforcing bars is defined by using the Menegotto and Pinto (1973) model. The Menegotto-Pinto Model (1973) was calibrated by using the experimental results for the reinforcing bars. Tensile properties of the reinforcing bars, tensile yield strength and tensile strain-hardening parameters, are altered to account for the tension stiffening according to Belarbi and Hsu (1994) while the same parameters for the reinforcing bars in compression are equal to those of bare bars.

As previously discussed in Section 2.3.2, some parameters are needed to define the cyclic stiffness degradation of the reinforcing bars as stated in Menegetto and Pinto (1973). Following the recommendation, these parameters are defined as $R_0 = 20$, $a_1 = 18.5$, and $a_2 = 0.15$. As previously described in Section 2.3.2, the buckling model requires slenderness ratio calculations. Table 4.5 shows the effective slenderness ratio calculations for each wall specimen. After calculating slenderness ratios for each boundary region, the results are found to be similar. Therefore, for simplicity, a single slenderness ratio is used at all boundary regions of each wall specimen. These slenderness ratios are taken as 8 for TUA, and 7 for TUB, TUC, and TUD.

Table 4.4. Parameters for reinforcing steel.

| Test Unit | | Rebar Orientation | Boundary 1 | | | | | Web | | | | | Boundary 2 | | | | |
|---|---|---|---|---|---|---|---|---|---|---|---|---|---|---|---|---|---|
| | | | ϕ (mm) | Rebar in Compression | | Rebar in Tension | | ϕ (mm) | Rebar in Compression | | Rebar in Tension | | ϕ (mm) | Rebar in Compression | | Rebar in Tension | |
| | | | | $f_y$ (MPa) | b | $f_y$ (MPa) | b | | $f_y$ (MPa) | b | $f_y$ (MPa) | b | | $f_y$ (MPa) | b | $f_y$ (MPa) | b |
| TUA | Web | Horizontal | 6 | 429 | 0.020 | 518 | 0.010 | 6 | 349 | 0.040 | 518 | 0.010 | 6 | 429 | 0.021 | 518 | 0.010 |
| | | Vertical | 12 | 352 | 0.030 | 494 | 0.005 | 6 | 309 | 0.050 | 518 | 0.010 | 12 | 352 | 0.031 | 494 | 0.005 |
| | Flanges | Horizontal | 6 | 429 | 0.020 | 518 | 0.010 | 6 | 349 | 0.040 | 518 | 0.010 | 6 | 429 | 0.021 | 518 | 0.010 |
| | | Vertical | 12 | 434 | 0.010 | 488 | 0.004 | 6 | 314 | 0.049 | 518 | 0.010 | 12 | 352 | 0.031 | 494 | 0.005 |
| TUB | Web | Horizontal | 6 | 455 | 0.020 | 518 | 0.010 | 6 | 414 | 0.024 | 518 | 0.010 | 6 | 455 | 0.015 | 518 | 0.010 |
| | | Vertical | 12 | 413 | 0.010 | 480 | 0.005 | 6 | 384 | 0.032 | 518 | 0.010 | 12 | 413 | 0.013 | 480 | 0.005 |
| | Flanges | Horizontal | 6 | 455 | 0.020 | 518 | 0.010 | 6 | 414 | 0.024 | 518 | 0.010 | 6 | 455 | 0.015 | 518 | 0.010 |
| | | Vertical | 12 | 416 | 0.010 | 475 | 0.005 | 6 | 382 | 0.032 | 518 | 0.010 | 12 | 413 | 0.013 | 480 | 0.005 |
| TUC | Web | Horizontal | 6 | 435 | 0.014 | 492 | 0.010 | 6 | 400 | 0.023 | 492 | 0.010 | 6 | 435 | 0.014 | 492 | 0.010 |
| | | Vertical | 8 | 504 | 0.010 | 563 | 0.007 | 8 | 500 | 0.011 | 563 | 0.007 | 8 | 504 | 0.010 | 563 | 0.007 |
| | West Flange | Horizontal | 6 | 435 | 0.014 | 492 | 0.010 | 6 | 400 | 0.023 | 492 | 0.010 | 6 | 435 | 0.014 | 492 | 0.010 |
| | | Vertical | 12 | 467 | 0.010 | 526 | 0.006 | 6 | 374 | 0.029 | 492 | 0.010 | 8 | 452 | 0.018 | 537 | 0.008 |
| | East Flange | Horizontal | 6 | 435 | 0.014 | 492 | 0.010 | 6 | 400 | 0.023 | 492 | 0.010 | 6 | 435 | 0.014 | 492 | 0.010 |
| | | Vertical | 8 | 506 | 0.010 | 563 | 0.007 | 8 | 497 | 0.011 | 563 | 0.007 | 8 | 506 | 0.009 | 563 | 0.007 |
| TUD | Web | Horizontal | 6 | 435 | 0.010 | 492 | 0.010 | 6 | 412 | 0.020 | 492 | 0.010 | 6 | 435 | 0.014 | 492 | 0.010 |
| | | Vertical | 8 | 504 | 0.010 | 563 | 0.007 | 8 | 500 | 0.011 | 563 | 0.007 | 8 | 504 | 0.010 | 563 | 0.007 |
| | West Flange | Horizontal | 6 | 435 | 0.010 | 492 | 0.010 | 6 | 412 | 0.020 | 492 | 0.010 | 6 | 435 | 0.014 | 492 | 0.010 |
| | | Vertical | 12 | 469 | 0.010 | 526 | 0.006 | 6 | 375 | 0.029 | 492 | 0.010 | 8 | 453 | 0.018 | 537 | 0.008 |
| | East Flange | Horizontal | 6 | 435 | 0.010 | 492 | 0.010 | 6 | 412 | 0.020 | 492 | 0.010 | 6 | 435 | 0.014 | 492 | 0.010 |
| | | Vertical | 8 | 506 | 0.010 | 563 | 0.007 | 8 | 497 | 0.011 | 563 | 0.007 | 8 | 506 | 0.010 | 563 | 0.007 |

Table 4.5. Slenderness ratio calculation for reinforcing bar buckling.

| Wall | Boundary No | Buckling Direction | $f_y$ (MPa) | Bar Diameter $D_b$ (mm) | Flexural Rigidity, $EI$ (N.mm$^2$) | Tie Spacing, $s$ (mm) | Tie Diameter $D_t$ (mm) | Tie Area, $A_t$ (mm2) | Tie Length, $l_e$ (mm) | Number of Bars $n_l/n_b$ | Tie Stiffness, $k_t$ (N/mm) | Normalizing Stiffness, $k$ (N/mm) | Equiv. Stiffness, $k_{eq}$ | Buckling Mode, $n$ | Slenderness, $L_{eff}/D_b$ | Avg. $L_{eff}/D_b$ |
|---|---|---|---|---|---|---|---|---|---|---|---|---|---|---|---|---|
| TUA | 1 | In-plane | 488.0 | 12.00 | $112.4*10^6$ | 50 | 6 | 28.27 | 167 | 1.0 | $33.9*10^3$ | $87.6*10^3$ | 0.3865 | 2 | 8.3 | 8.3 |
| | | Out-of-plane | 488.0 | 12.00 | $112.4*10^6$ | 50 | 6 | 28.27 | 118 | 0.5 | $24.0*10^3$ | $87.6*10^3$ | 0.2735 | 2 | 8.3 | |
| | 2 | In-plane | 488.0 | 12.00 | $112.4*10^6$ | 50 | 6 | 28.27 | 268 | 1.0 | $21.1*10^3$ | $87.6*10^3$ | 0.2408 | 2 | 8.3 | 9.2 |
| | | Out-of-plane | 498.0 | 10.00 | $54.8*10^6$ | 50 | 6 | 28.27 | 118 | 0.5 | $24.0*10^3$ | $42.7*10^3$ | 0.5614 | 2 | 10.0 | |
| TUB | 1 | In-plane | 471.0 | 12.00 | $110.5*10^6$ | 50 | 6 | 28.27 | 265 | 1.0 | $21.3*10^3$ | $86.1*10^3$ | 0.2479 | 2 | 8.3 | 6.5 |
| | | Out-of-plane | 482.5 | 10.50 | $65.5*10^6$ | 50 | 6 | 28.27 | 68 | 0.5 | $41.6*10^3$ | $51.1*10^3$ | 0.8142 | 1 | 4.8 | |
| | 2 | In-plane | 487.0 | 12.00 | $112.3*10^6$ | 50 | 6 | 28.27 | 165 | 1.0 | $34.3*10^3$ | $87.5*10^3$ | 0.3916 | 2 | 8.3 | 6.7 |
| | | Out-of-plane | 487.0 | 10.00 | $54.2*10^6$ | 50 | 6 | 28.27 | 68 | 0.5 | $41.6*10^3$ | $42.2*10^3$ | 0.9851 | 1 | 5.0 | |
| TUC | 1 | In-plane | 526.2 | 12.00 | $116.7*10^6$ | 50 | 6 | 28.27 | 168 | 1.0 | $33.7*10^3$ | $91.0*10^3$ | 0.3700 | 2 | 8.3 | 6.7 |
| | | Out-of-plane | 517.6 | 10.00 | $55.8*10^6$ | 50 | 6 | 28.27 | 64 | 0.5 | $44.2*10^3$ | $43.5*10^3$ | 1.0153 | 1 | 5.0 | |
| | 2 | In-plane | 563.0 | 8.00 | $23.9*10^6$ | 50 | 6 | 28.27 | 163 | 1.0 | $34.7*10^3$ | $18.6*10^3$ | 1.8663 | 1 | 6.3 | 6.5 |
| | | Out-of-plane | 539.3 | 7.33 | $16.5*10^6$ | 50 | 6 | 28.27 | 64 | 0.5 | $44.2*10^3$ | $12.8*10^3$ | 3.4455 | 1 | 6.8 | |

Table 4.5. Slenderness ratio calculation for reinforcing bar buckling (cont.).

| Wall | Boundary No | Buckling Direction | $f_y$ (MPa) | Bar Diameter $D_b$ (mm) | Flexural Rigidity, $EI$ (N.mm$^2$) | Tie Spacing, $s$ (mm) | Tie Diameter $D_t$ (mm) | Tie Area, $A_t$ (mm2) | Tie Length, $l_e$ (mm) | Number of Bars $n_l/n_b$ | Tie Stiffness, $k_t$ (N/mm) | Normalizing Stiffness, $k$ (N/mm) | Equiv. Stiffness, $k_{eq}$ | Buckling Mode, $n$ | Slenderness, $L_{eff}/D_b$ | Avg. $L_{eff}/D_b$ |
|---|---|---|---|---|---|---|---|---|---|---|---|---|---|---|---|---|
| TUC | 3 | In-plane | 563.0 | 8.00 | $23.9*10^6$ | 50 | 6 | 28.27 | 164 | 1.0 | $34.5*10^3$ | $18.6*10^3$ | 1.8550 | 1 | 6.3 | 6.3 |
| | | In-plane | 563.0 | 8.00 | $23.9*10^6$ | 50 | 6 | 28.27 | 64 | 0.5 | $44.2*10^3$ | $18.6*10^3$ | 2.3767 | 1 | 6.3 | |
| | 4 | Out-of-plane | 563.0 | 8.00 | $23.9*10^6$ | 50 | 6 | 28.27 | 163 | 1.0 | $34.7*10^3$ | $18.6*10^3$ | 1.8663 | 1 | 6.3 | 6.3 |
| | | In-plane | 563.0 | 8.00 | $23.9*10^6$ | 50 | 6 | 28.27 | 64 | 0.5 | $44.2*10^3$ | $18.6*10^3$ | 2.3767 | 1 | 6.3 | |
| | 5 | Out-of-plane | 563.0 | 8.00 | $23.9*10^6$ | 50 | 6 | 28.27 | 168 | 1.0 | $33.7*10^3$ | $18.6*10^3$ | 1.8108 | 1 | 6.3 | 6.3 |
| | | In-plane | 563.0 | 8.00 | $23.9*10^6$ | 50 | 6 | 28.27 | 64 | 0.5 | $44.2*10^3$ | $18.6*10^3$ | 2.3767 | 1 | 6.3 | |
| TUD | 1 | Out-of-plane | 526.2 | 12.00 | $116.7*10^6$ | 50 | 6 | 28.27 | 168 | 1 | $33.7*10^3$ | $91.0*10^3$ | 0.3700 | 2 | 8.3 | 6.7 |
| | | In-plane | 517.6 | 10.00 | $55.8*10^6$ | 50 | 6 | 28.27 | 64 | 0.5 | $44.2*10^3$ | $43.5*10^3$ | 1.0153 | 1 | 5.0 | |
| | 2 | Out-of-plane | 563.0 | 8.00 | $23.9*10^6$ | 50 | 6 | 28.27 | 163 | 1 | $34.7*10^3$ | $18.6*10^3$ | 1.8663 | 1 | 6.3 | 6.5 |
| | | In-plane | 539.3 | 7.33 | $16.5*10^6$ | 50 | 6 | 28.27 | 64 | 0.5 | $44.2*10^3$ | $12.8*10^3$ | 3.4455 | 1 | 6.8 | |
| | 3 | Out-of-plane | 563.0 | 8.00 | $23.9*10^6$ | 50 | 6 | 28.27 | 164 | 1 | $34.5*10^3$ | $18.6*10^3$ | 1.8550 | 1 | 6.3 | 6.3 |
| | | In-plane | 563.0 | 8.00 | $23.9*10^6$ | 50 | 6 | 28.27 | 64 | 0.5 | $44.2*10^3$ | $18.6*10^3$ | 2.3767 | 1 | 6.3 | |
| | 4 | Out-of-plane | 563.0 | 8.00 | $23.9*10^6$ | 50 | 6 | 28.27 | 163 | 1 | $34.7*10^3$ | $18.6*10^3$ | 1.8663 | 1 | 6.3 | 6.3 |
| | | In-plane | 563.0 | 8.00 | $23.9*10^6$ | 50 | 6 | 28.27 | 64 | 0.5 | $44.2*10^3$ | $18.6*10^3$ | 2.3767 | 1 | 6.3 | |
| | 5 | In-plane | 563.0 | 8.00 | $23.9*10^6$ | 50 | 6 | 28.27 | 168 | 1 | $33.7*10^3$ | $18.6*10^3$ | 1.8108 | 1 | 6.3 | 6.3 |
| | | Out-of-plane | 563.0 | 8.00 | $23.9*10^6$ | 50 | 6 | 28.27 | 64 | 0.5 | $44.2*10^3$ | $18.6*10^3$ | 2.3767 | 1 | 6.3 | |

## 4.3. Comparison of Model Responses with Experimental Data

The effectiveness of the FSAFE model in predicting the global and lateral responses of four U-shaped wall specimens (Beyer et al., 2008, Constantin and Beyer, 2016) subjected to multidirectional loading is presented in this section. Test results and model predictions are compared at both global and response levels. At the global level, the lateral load versus top displacement responses are compared, and at local level, the comparisons are done in terms of shear and flexural deformation contributions to top displacement, vertical strain distributions at wall base, and vertical strain profiles along wall height at various locations of the U-shaped wall specimens.

### 4.3.1. Load versus Top Displacement Responses

In this section, analytical and experimental load-displacement responses for the nonrectangular wall specimens subjected to biaxial loading are compared (Figure 9-12). The geometry of test specimens was described in detail previously on Section 4.1. These U-shaped test units were subjected to complex loading histories and the top displacement histories for test units TUA, TUB (Beyer et al., 2008), TUC, and TUD (Constantin and Beyer, 2016) are given in Figure 9f, 10f, 11f, and 12f, respectively. TUA and TUB (Beyer et al., 2008) were subjected to cycles in east-west direction (position A-B), north-south direction (position C-D), and a complex loading cycle called sweep (Figure 9f) for five ductility levels ranging from 1.0 to 6.0. Specimens TUC and TUD (Constantin and Beyer, 2016) were subjected to loading in east-west direction (position A-B) and north-south direction (position C-D) at drift levels of 0.1%, 0.2%, 0.3%, 0.4%, 0.6%, and 0.8% while the diagonal loading cycles (position E-F, and position H-G) started at 0.2% drift level and continued through 0.3%, 0.4%, 0.6%, 1.0%, 1.5%, 2.0%, 2.5%, 3.0% drift level for TUC and up to 1.5% for TUD.

Figure 4.9 displays the load-displacement responses of specimen TUA for loading cycles in E-W direction (Figure 4.9a), N-S direction (Figure 4.9b), diagonal cycles (Figure 4.9c, d), square-root-of-sum-of-squares (SRSS) load-displacement response (Figure 4.9e) and loading history and top displacement (Figure 4.9f).

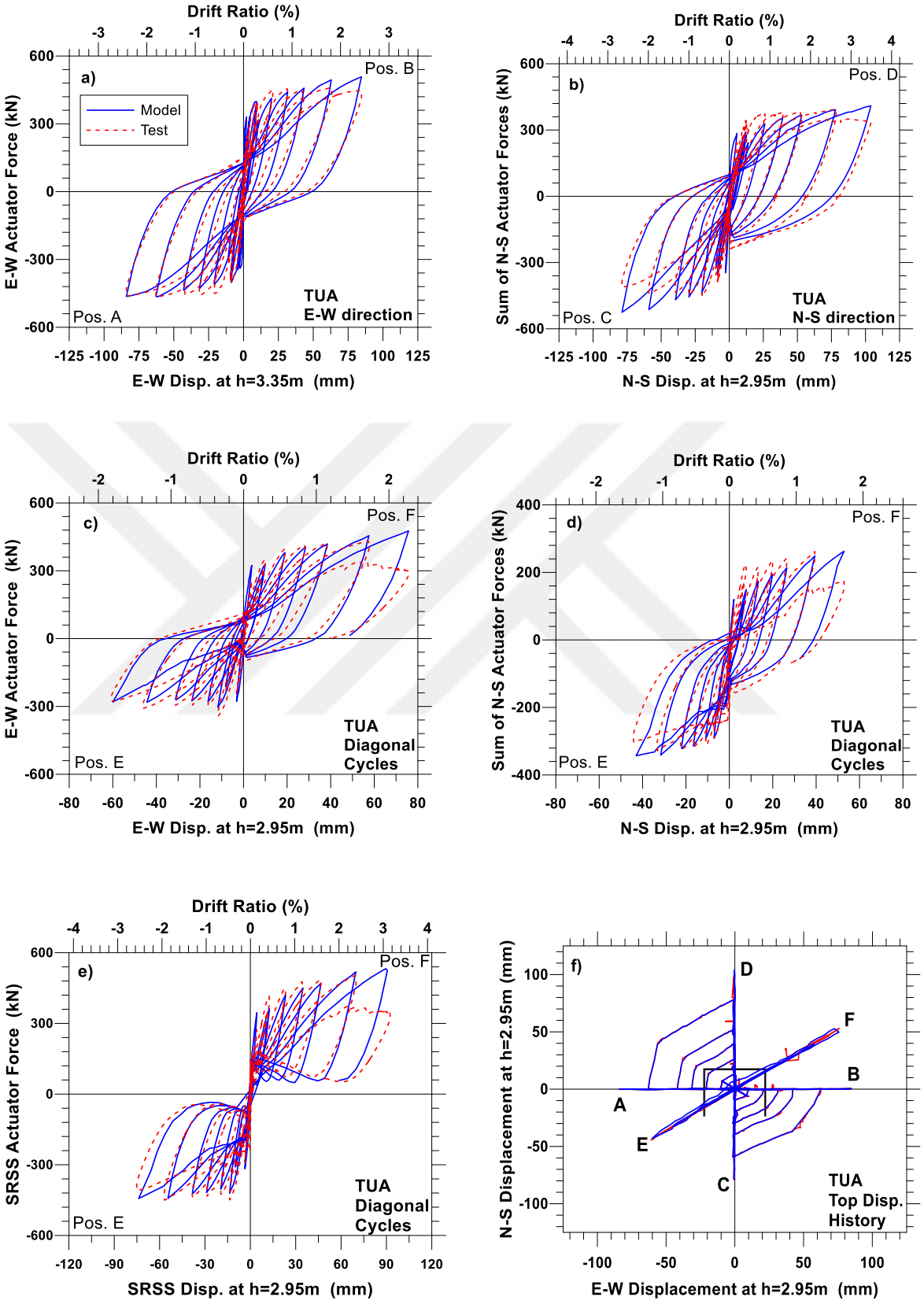


Figure 4.9. Load displacement responses of specimen TUA.

For specimen TUA, the model captures the hysteretic characteristics of the responses such as pinching behavior and plastic displacement at zero load, lateral load capacities and stiffness. For E-W loading cycles (Figure 4.9a), the model predicts the load capacity in the west loading direction (Position A) very well while the overestimation of the load capacity in the east direction (Position B) is 10%. Prediction of the load capacity in the N-S direction (Figure 4.9b) shows good match with the experimental results at Position D (wall web is under compression) while the load capacity is overestimated approximately 15% at Position C (wall flanges are under compression). The actuator forces during diagonal cycles (Figure 4.9c, d, e) show very good correlation with the experimental data for intermediate cycles; however, the model cannot capture the significant strength loss at displacement ductility level $\mu = 8.0$ caused by the rupture of some reinforcing bars while loading from Position F (corner between the wall web and east flange is under compression) to Position E (west flange end is in compression) possibly because the reinforcing bar rupture is not incorporated into the model formulation . Furthermore, the model overestimates the N-S actuator force (Figure 4.9d) for the diagonal cycles for displacement ductility level $\mu = 8.0$ at Position E by 15%.

Load-displacement responses for the test unit TUB are presented for E-W direction in Figure 4.10a, for N-S direction in Figure 4.10b, for diagonal direction in Figure 4.10c, d, SRSS load-displacement response in Figure 4.10e, and top displacement history in Figure 4.10f. Similarly to specimen TUA, model predicts the hysteretic characteristics such as stiffness, pinching behavior, and lateral load capacity very well. The model underestimates the load capacity for cycles in the east-west direction (Figure 4.10a) by approximately 5% only. Similarly, the E-W actuator load-displacement response under diagonal loading cycles (Figure 4.10c) is estimated within 90% of the experimentally measured response. However, for loading cycles in N-S direction (Figure 4.10b) and N-S actuators load-displacement response under diagonal loading cycles (Figure 4.10d), the load capacity at Position E (west flange end is subjected to compression) is overestimated up to 15% and 20%, respectively. At position F, however; the error in prediction is approximately 10% for both cases. For SRSS load-displacement response under diagonal loading (Figure 4.11e), the difference between the analytically predicted and experimentally measured responses are limited, by up to ±10%.

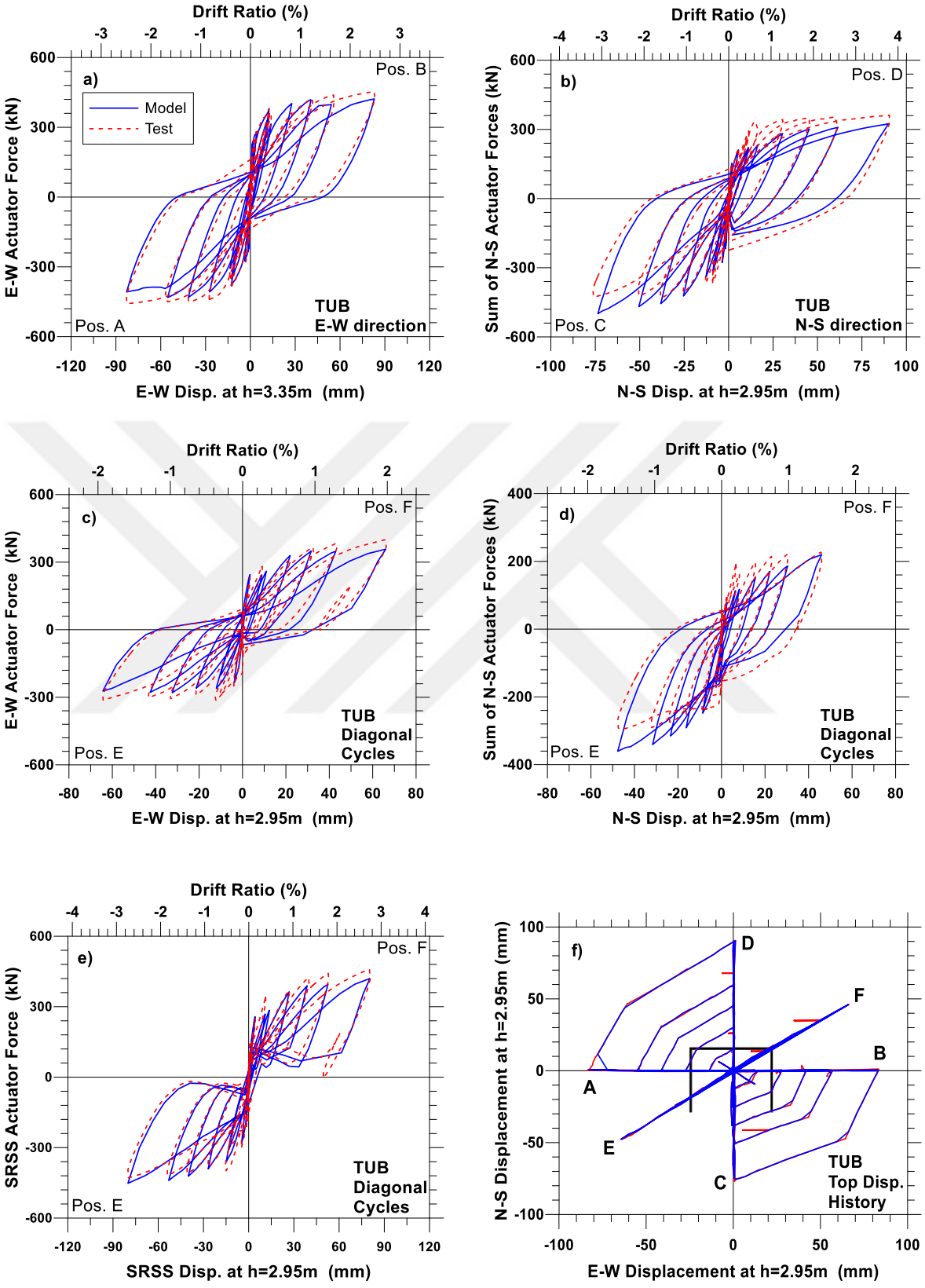


Figure 4.10. Load displacement responses of specimen TUB.

Load-displacement responses of specimen TUC are given for the E-W direction in Figure 4.11a, for N-S direction in Figure 4.11b, for E-F diagonal direction in Figure 4.11c, d, SRSS load-displacement response for E-F diagonal loading in Figure 4.11e, top displacement history in Figure 4.11f, for H-G diagonal direction in Figure 4.1g, h, and SRSS load-displacement response for H-G diagonal loading in Figure 4.11i. Similar to specimen TUB, the model estimates the lateral load capacity for E-W loading cycles (Figure 4.11a) and E-W actuator forces under E-F and H-G diagonal loading cycles (Figure 4.11c, g) with an accuracy of larger than 90%. However, for N-S loading cycles (Figure 4.11b), model underestimates the load capacity at Position C by approximately 10% while a more significant underestimation (up to 30%) is seen at Position D. The N-S actuator forces in either diagonal loading cycles (Figure 4.11d, h) at the positive loading direction are captured well for the last loading cycles; however, N-S actuator forces for the intermediate E-F diagonal loading cycles (Figure 4.11d) are underestimated up to 30% at Position F (intersection of wall web and east flange is subjected to compression) while the same forces are underestimated up to 40% at position G (wall web and west flange intersection is under compression) for the intermediate H-G diagonal loading cycles (Figure 4.11g). The model also manages to capture the SRSS load-displacement responses for the diagonal loading cycles (Figure 4.11e, i) with an overestimation approximately of 10% at Position E during the E-F loading cycles. Similar to specimen TUA, the predicted load-displacement responses for diagonal cycles do not show the sudden strength loss due the onset of out-of-plane buckling of the west flange end and compression failure of the unconfined concrete in the west flange during the last E-F loading cycle while loading to Position E (west flange end is subjected to compression) (Figure 4.11c, d, e) since the out-of-plane behavior is not included in the model formulation. Also, crushing was observed in the east flange while loading to Position H (east flange is subjected to compression) after the failure of the west flange. This led to a significant strength loss and the analytically determined results do not reflect this sudden strength loss (Figure 4.11h,i). Overall, the model can capture the lateral load capacities, unloading stiffness, and hysteretic characteristics reasonably well. However, the pinching characteristics in E-W direction (Figure 4.11a) and N-S direction (Figure 4.11b) are slightly overestimated and the load capacities in the positive N-S direction (Figure 4.11b, d, h) are always underestimated.

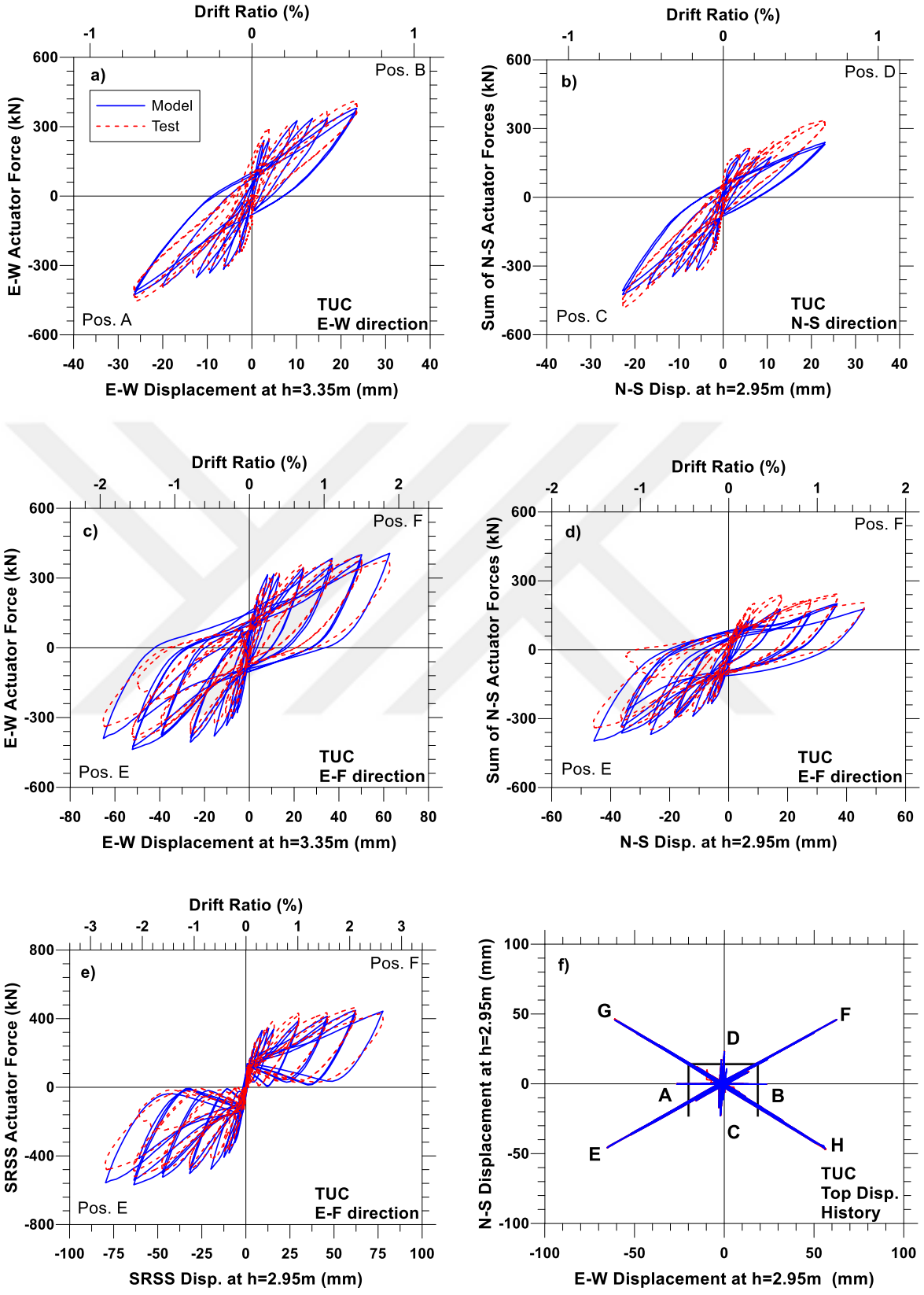


Figure 4.11. Load displacement responses of specimen TUC.

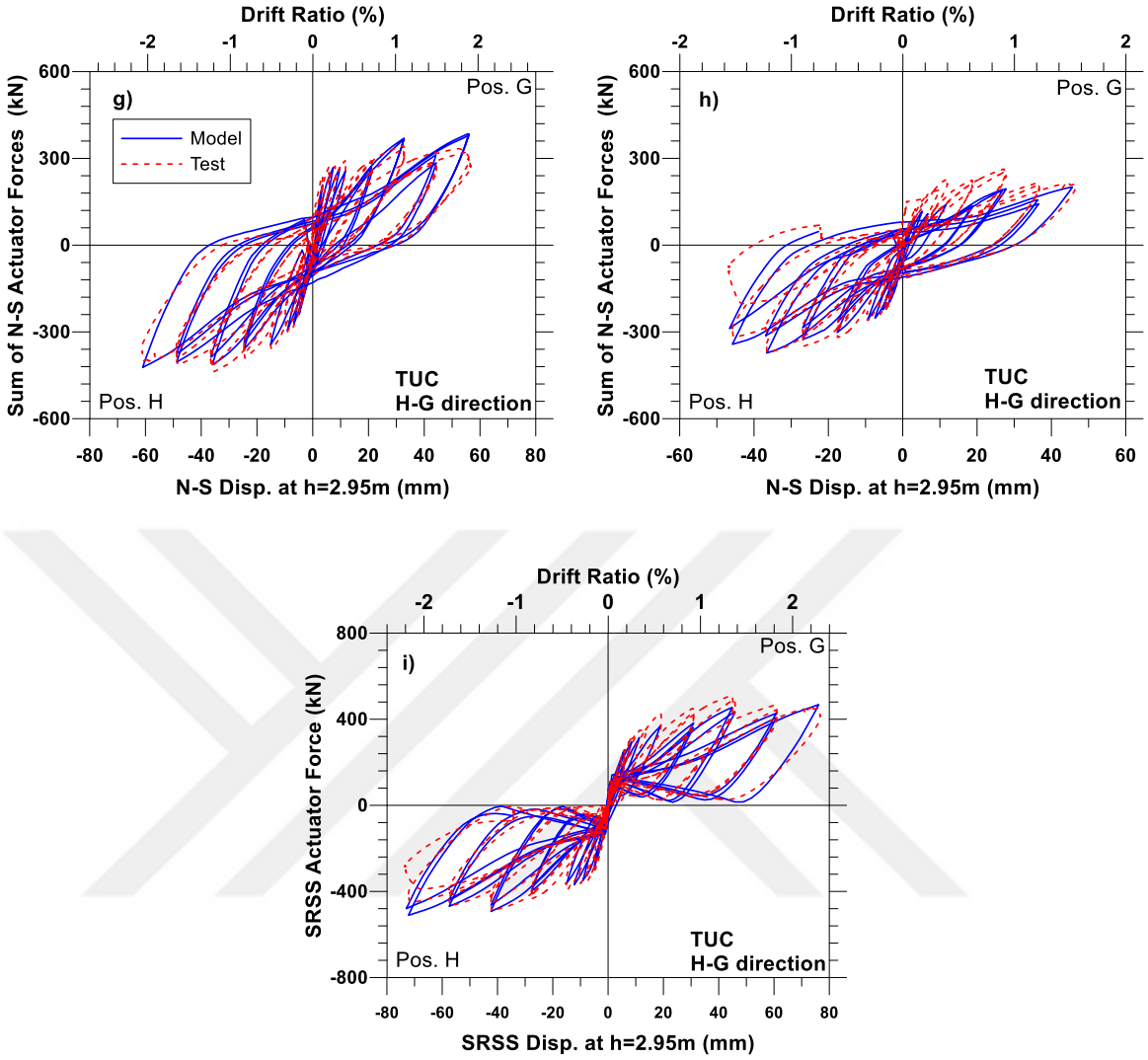


Figure 4.11. Load displacement responses of specimen TUC (cont.).

Load-displacement responses of specimen TUD are given for the E-W direction in Figure 4.12a, for N-S direction in Figure 4.12b, for E-F diagonal direction in Figure 4.12c, d, SRSS load-displacement response for E-F diagonal loading in Figure 4.12e, top displacement history in Figure 4.12f, for H-G diagonal direction in Figure 4.12g, h, and SRSS load-displacement response for H-G diagonal loading in Figure 4.12i. Similar to the results of TUC, the model predicts the load-displacement response in E-W direction (Figure 4.12a) with an error up to 10% for the loading cycles. For N-S cycles (Figure 4.12b), the analytically determined load capacity is captured very accurately at Position C (wall flanges are under compression) while the load capacity at Position D is underestimated by approximately 15%. The failure mode of the specimen TUD is the crushing of the east flange at Position H (east flange end is subjected to compression) during the second cycle of 1.5%

drift which resulted in approximately 75% loss in SRSS force capacity. The loading continued in E-F direction; however, wall web crushed during the first cycle and loading was stopped due to significant loss of load bearing capacity of the wall. The E-W actuator force under diagonal loading in the E-F direction (Figure 4.12c) is over-predicted by approximately 10%. For the N-S actuator forces predicted for the E-F diagonal loading case (Figure 4.12d), the model underestimates the load capacity approximately by 20% when the wall web and east flange intersection is under compression (Position F) while this underestimation turns into overestimation by approximately 10% when the west flange end is under compression (Position E). The model predicts the SRSS load-displacement response for the diagonal loading in the E-F direction (Figure 4.12e) within approximately 90% of that measured experimentally. Even though the analytically determined results show a degradation in the lateral force, it cannot capture the significant strength drop after crushing of the web at approximately 1.0% drift during the last E-F loading cycle. The E-W actuator force during diagonal loading in H-G direction (Figure 4.12g) shows excellent correlation with the experimental results for the positive loading cycles (Position G) while the underestimation of the lateral force around 10% in the negative loading cycles (Position H). The prediction for the sum of N-S actuator forces under the loading in the H-G direction (Figure 4.12h) shows very good agreement with the experimental results when the east flange end is in compression (Position H), while the capacity in the positive loading direction is under-predicted by approximately 10%. Also, SRSS load-displacement during H-G loading cycles (Figure 4.12i) is predicted reasonably well. However, for all load-displacement components for H-G loading, the model cannot capture the sudden loss of the lateral force capacity due to crushing of the east flange at a drift level of approximately 1.0%.

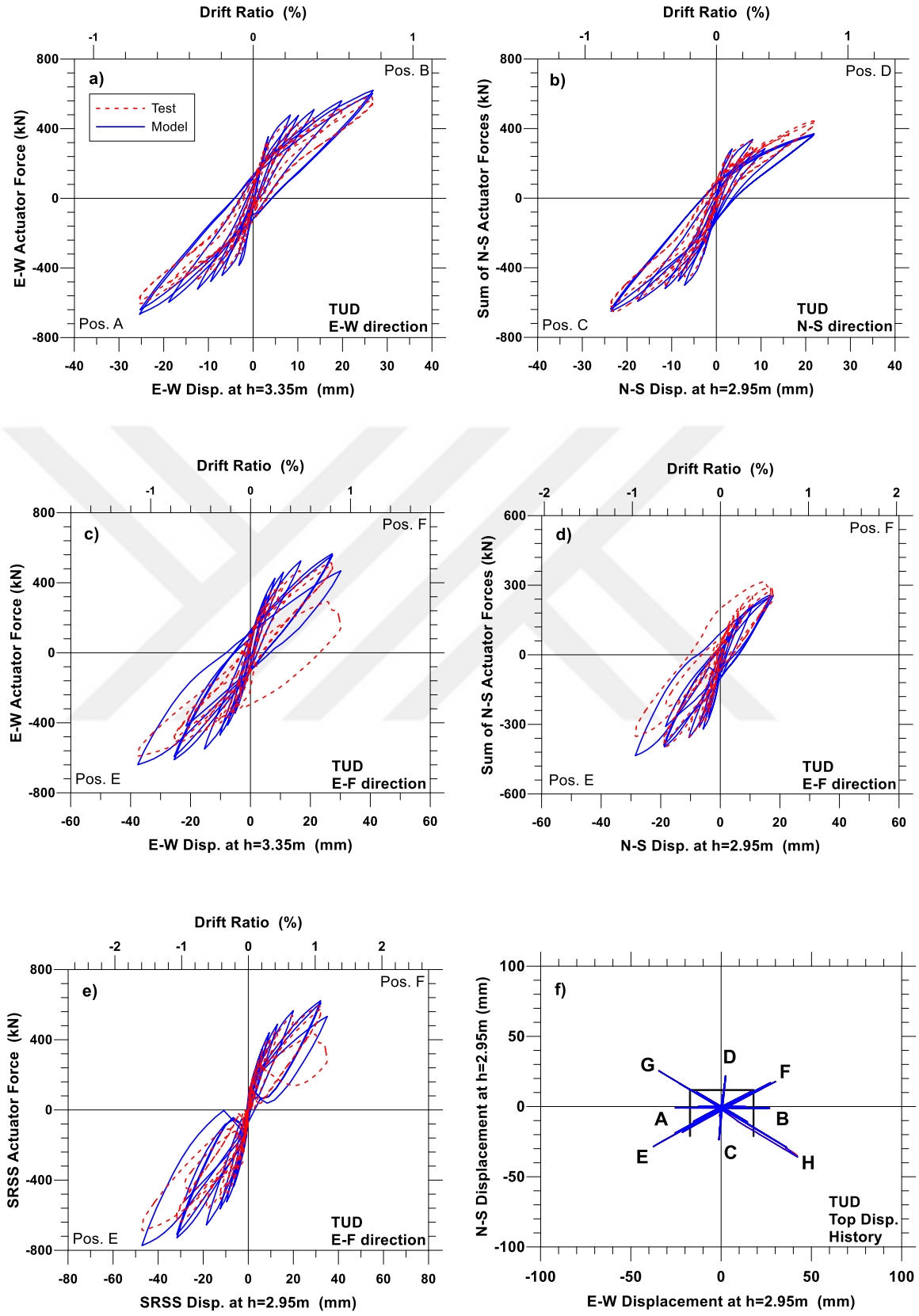


Figure 4.12. Load displacement responses of specimen TUD.

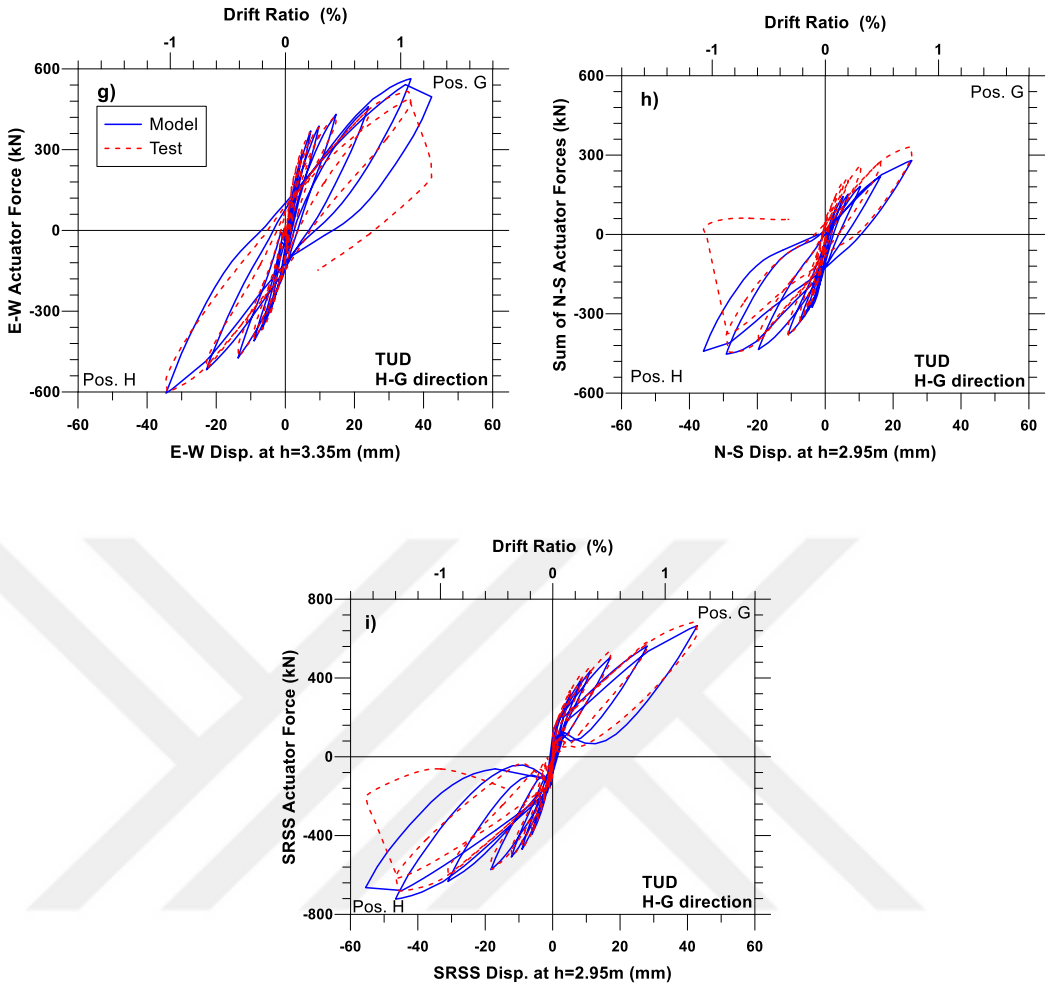


Figure 4.12. Load displacement responses of specimen TUD (cont.).

### 4.3.2. Flexural and Shear Deformation Components

Accuracy of the predictions is also assessed in terms of shear and flexural deformations (Figure 4.13-16). For TUA and TUB (Beyer et. al, 2008), the ratio of flexural deformations to the top displacements are compared while for TUC and TUD (Constantin and Beyer, 2016), the ratio of shear to flexural deformations are compared. It should be noted that, during the experiments, the top displacement was defined as a combination of shear and flexural deformations and sliding. However, for the analytically predicted results the top displacement is defined as the sum of shear and flexural deformations only. For consistency, the sliding deformations are excluded from the experimental results. Sliding deformations were small (the largest contribution not exceeding 5.0% for any of the specimens) compared to other deformation components.

Flexural deformation contributions to the top displacement of specimen TUA are given for the flanges under N-S loading cycles in Figure 4.13a, for the web under E-W loading cycles in Figure 4.13b, for the flanges under diagonal loading in Figure 4.13c, and for the web under diagonal loading in Figure 4.13d. Figure 4.13a reveals very good agreement between the analytical and experimental results while the contribution of flexural deformations are underestimated with an increasing error percentage (up to 20% in the last cycle) in Figure 4.13b. Figure 4.13c shows also a reasonably well correlation. However, the model significantly underestimates the flexural deformation contribution to the top displacement (up to 40% in the last cycle) in the wall web at position E (Figure 4.13d) while the model can capture the ratios at Position F within an accuracy of 85% for all cycles.

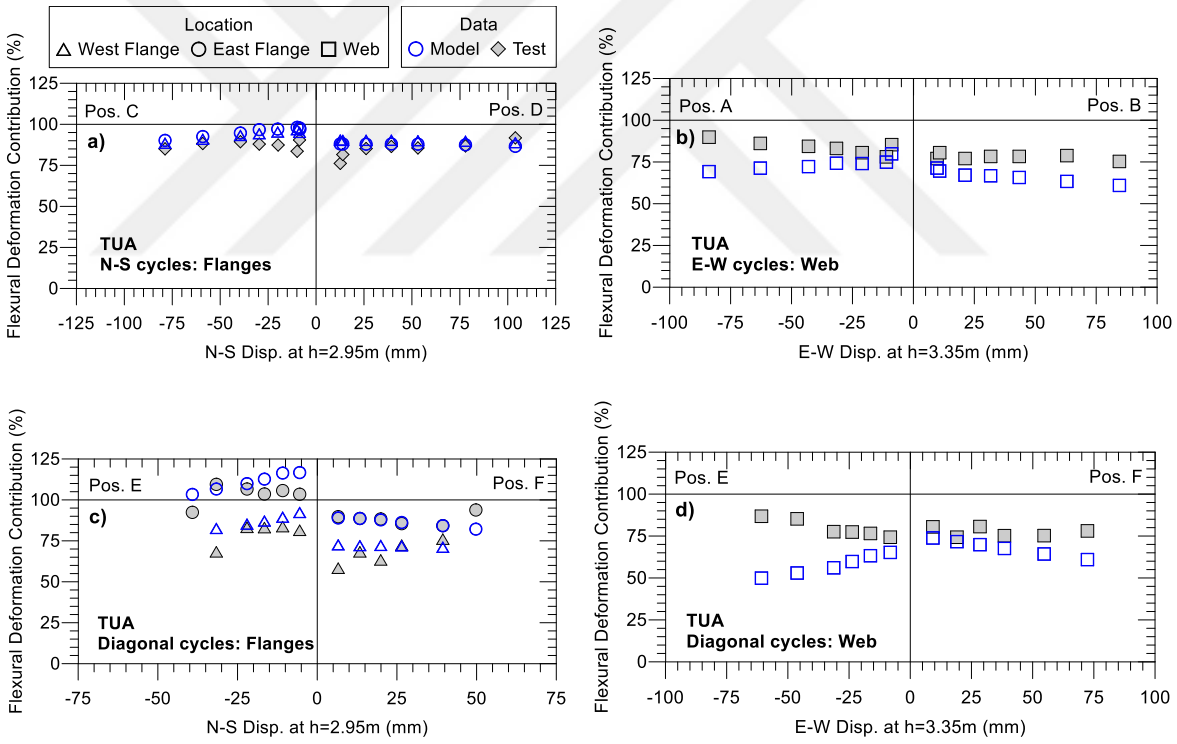


Figure 4.13. Contributions of flexural deformations to wall top displacement for specimen TUA.

For TUB, similarly to TUA, the flexural deformation contributions to the top displacement are given for the flanges under N-S loading cycles in Figure 4.14a, for the web under E-W loading cycles in Figure 4.14b, for the flanges under diagonal loading in Figure 4.14c, and for the web under diagonal loading in Figure 4.14d. The analytical results for

TUB are more accurate than it is for TUA. Figure 4.14a and 4.14b show very good correlation between the analytical results and experimental data at the flanges for all N-S cycles as well as in the wall web for most of the E-W cycles. For diagonal cycles, the model can capture the ratio of deformation components at the flanges and the wall web for most of the loading cycles, largest difference being 25% in the last cycle (displacement ductility level μ=6.0) at the wall web.

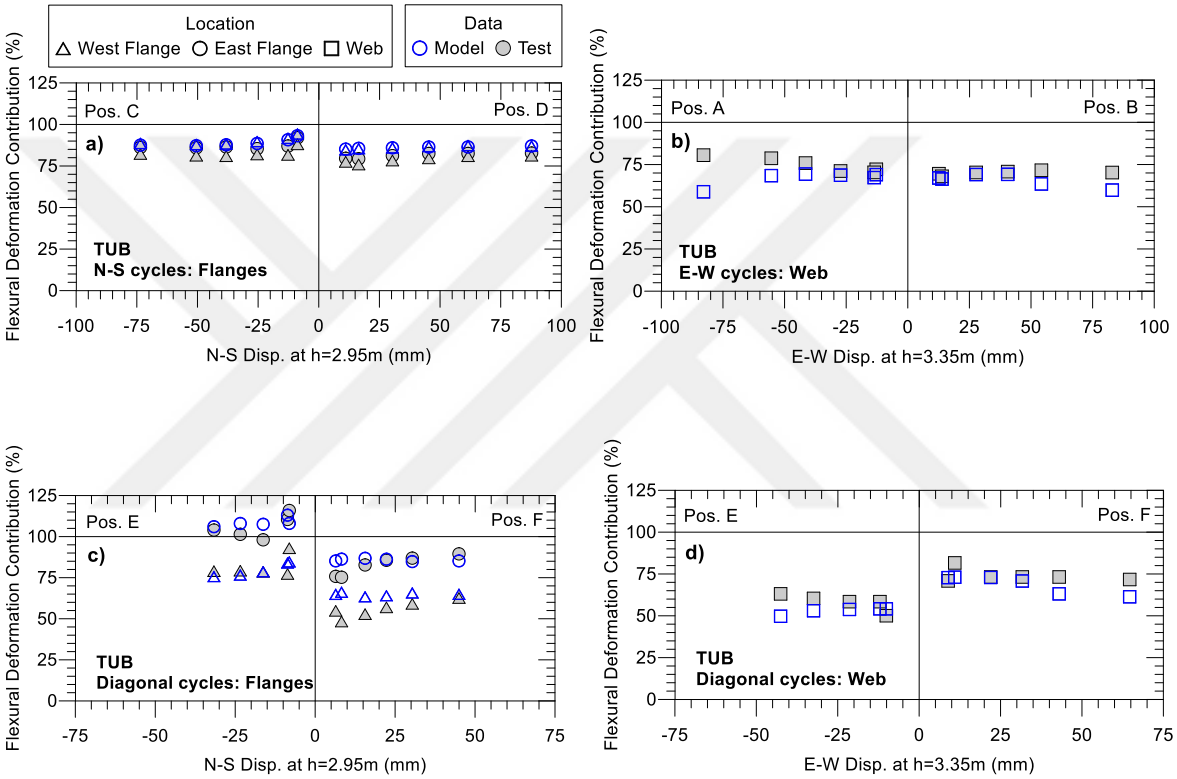


Figure 4.14. Contributions of flexural deformations to wall top displacement for specimen TUB.

Figure 4.15 shows the shear to flexural deformation ratios for specimen TUC. Shear to flexural deformation ratios under different loading types are given in the following order: in wall flanges under N-S loading (Figure 4.15a), in wall web under E-W loading (Figure 4.15b), in wall flanges under diagonal loading in E-F direction (Figure 4.15c), in wall web under diagonal E-F loading (Figure 4.15d), in wall flanges under diagonal loading in H-G direction (Figure 4.15e), in wall web under diagonal H-G loading (Figure 4.15f). Predicted shear to flexural deformation ratios of the flanges at various drift levels under N-S loading (Figure 4.15a) show very good agreement with the experimentally measured results when

the flanges are under compression (Position C) while the ratios are mostly underestimated by the model (approximately by 50%) when the flanges are subjected to tension (Position D). Figure 4.15b shows that the over-prediction of shear deformation at the wall web by the model is very significant especially for the lower drift levels. Figure 4.15c shows that the predictions for the east flange under diagonal loading E-F shows excellent correlation while the result for the west flange is overestimated by 35% on average when the west flange end is under compression (Position E) and underestimated by approximately 40% for the larger drift levels and around 80% for the first few drift levels when the west flange end is under tension (Position F). Similarly, the model prediction at the wall web for diagonal E-F loading (Figure 4.15d) shows significant overestimation at lower drift levels while matching well with the experimental data at larger drift levels. Figure 4.15e indicates that the shear to flexural deformation ratios are predicted more accurately when the flange end is under compression (Position H) while the analytically calculated values are significantly under-predicted at the flange that is subjected to the tension (east flange at Position G). Similar to the diagonal cycles in E-F direction, the wall web shows more divergence from the experimental data at lower drift levels (Figure 4.15f).

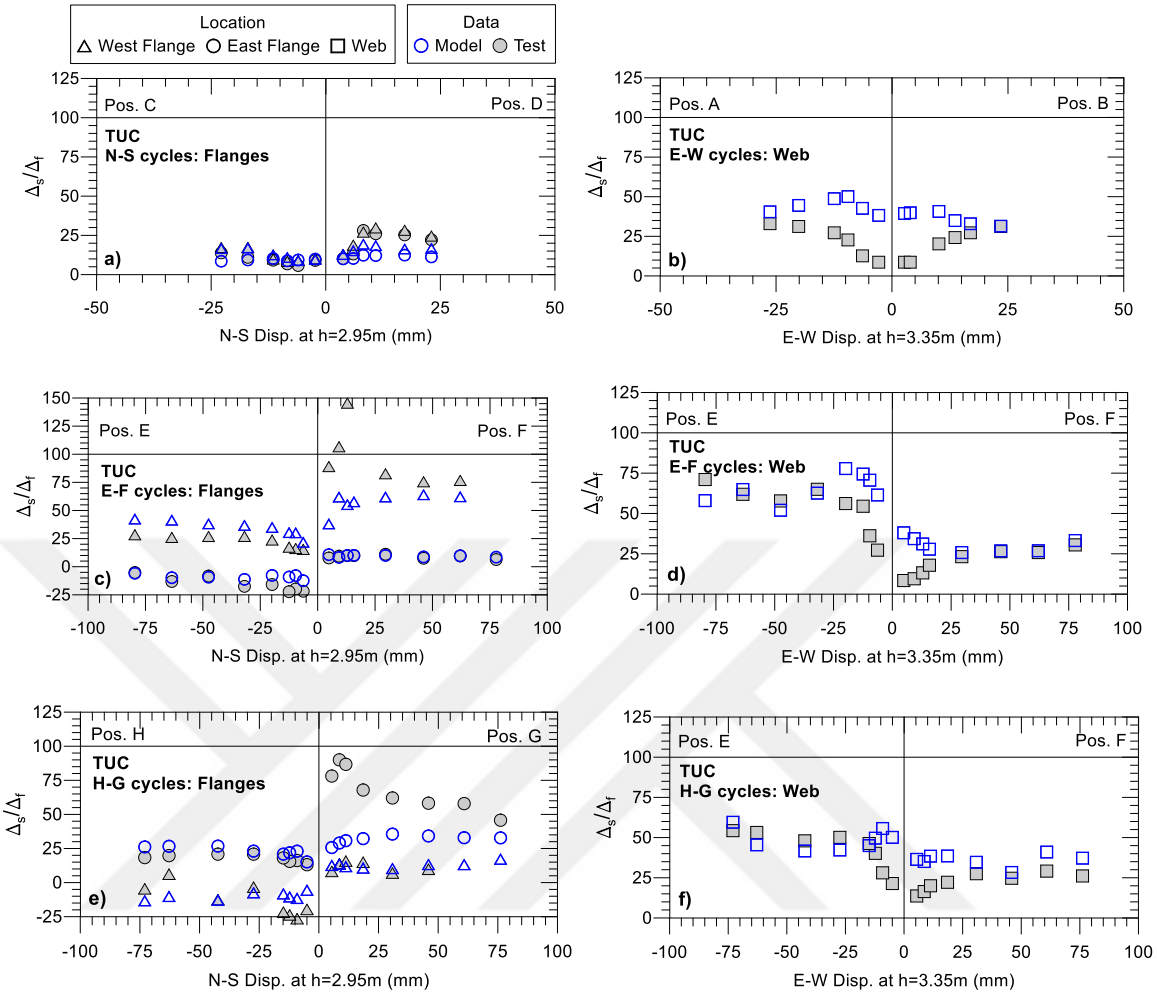


Figure 4.15. Ratio of flexural deformations to shear deformations for specimen TUC.

The comparison of shear to flexural deformation ratios for specimen TUD is given in Figure 4.16. Shear to flexural deformation ratios under different loading types are given in the following order: in wall flanges under N-S loading (Figure 4.16a), in wall web under E-W loading (Figure 4.16b), in wall flanges under diagonal loading in E-F direction (Figure 4.16c), in wall web under diagonal E-F loading (Figure 4.16d), in wall flanges under diagonal loading in H-G direction (Figure 4.16e), in wall web under diagonal H-G loading (Figure 4.16f). The shear to flexural deformation ratios at the flanges under N-S cycles (Figure 4.16a) are overestimated when the flanges are under compression (Position C) while the ratios at Position D are underestimated by the model. Figure 4.16b, Figure 4.16d, and Figure 4.16f show that regardless of the type of loading, contribution of shear deformations to the total displacement is significantly overestimated by the model. Similar to specimen TUC, the shear deformations at the flanges under diagonal loading cycles (Figure 4.16c and Figure

4.16e) are significantly underestimated at the flange that was subjected to tension (west flange at Position F for E-F loading and east flange at Position G for H-G loading).

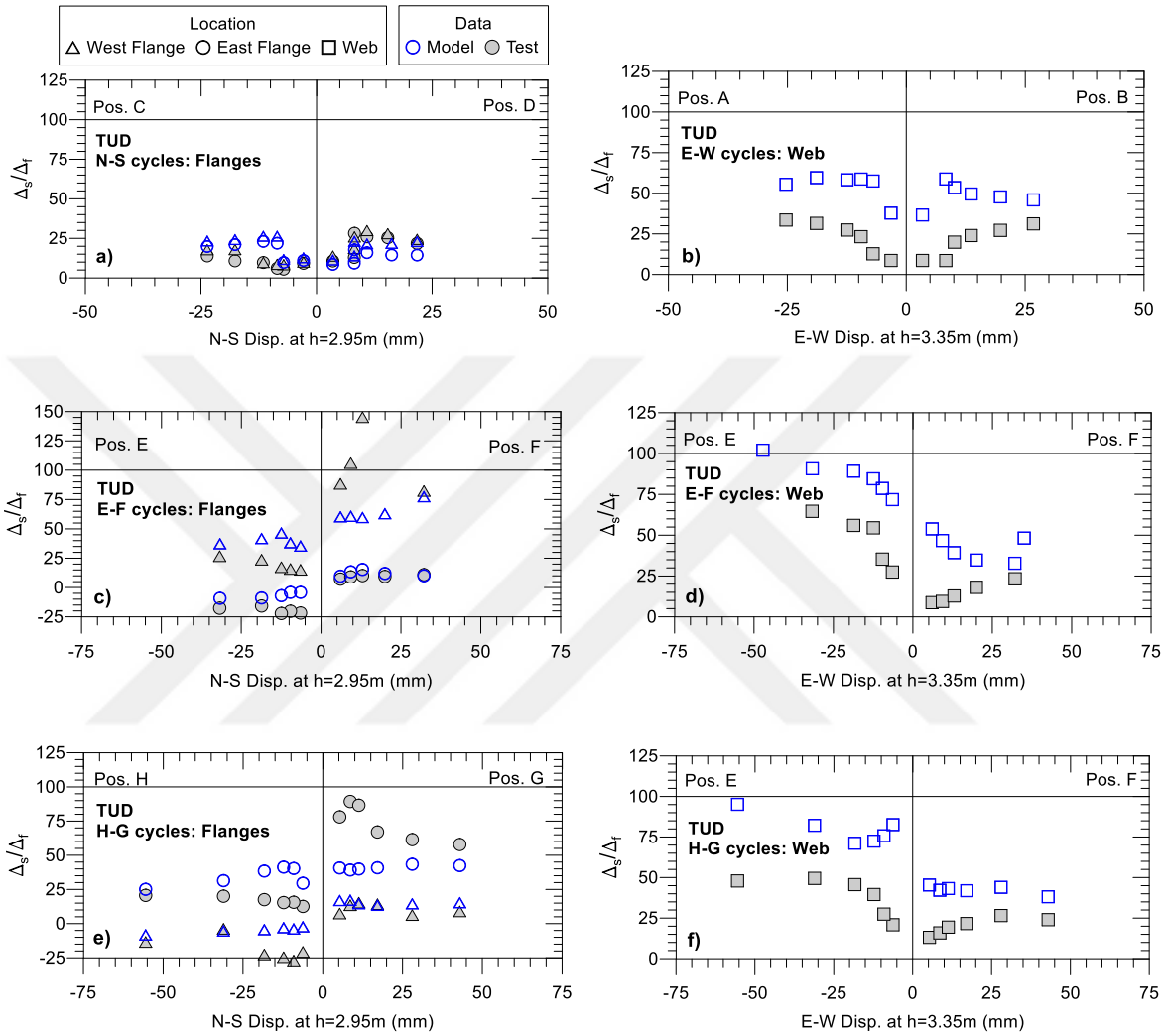


Figure 4.16. Ratio of flexural deformations to shear deformations for specimen TUD.

Overall, the shear and flexural deformations are replicated reasonably well by the model for all specimens; however, model seems to give slightly better results for specimens TUA and TUB. Experimental results for TUC and TUD show that the flange with the concentrated vertical reinforcement (west flange) shows larger shear deformation contributions compared to the flange with distributed vertical reinforcement (east flange) especially when the flanges are under tension and the wall is subjected to diagonal loading. Even though the model cannot capture the shear to flexural deformation ratios for TUC and TUD very accurately, the effect of different reinforcement layouts is visible in analytically

calculated results as well. Even though a reinforcing bar buckling model was incorporated, since the model is composed of membrane elements, out-of-plane forces which are more pronounced for flanged wall sections under bi-directional loading were not considered and this may have caused the difference between the experimental and the model results.

### 4.3.3. Vertical Strain Profiles Along Wall Height

The analytically replicated vertical strain profiles and test results of specimens TUB, TUC, and TUD at certain loading positions and drift levels are compared in from Figure 4.17 to Figure 4.19. Vertical strain profiles for TUB are given for loading position C (N-S cycles, flange ends in compression), position D (N-S cycles, wall web is in compression), and position A (corner between the west flange and wall web is under compression) at marked locations at displacement ductility levels of $\mu$=1.0 (low drift cycles), $\mu$=3.0 (intermediate drift cycles), $\mu$=6.0 (large drift cycles). Mentioned loading positions can be seen in Figure 4.10f for specimen TUB. These vertical strain profiles along the wall height are shown at the west flange at Position C in Figure 4.17a, at the same location at Position D in Figure 4.17b, at the corner between the east flange and the wall web at Position C in Figure 4.17c, and at the same location at Position A in Figure 4.17d. Figure 4.17 shows that the model can capture the vertical strains along the wall height and the concentration of vertical strains at the plastic hinge length of the wall specimen (bottom 900mm) is also predicted well. However, Figure 4.17a shows that the compressive vertical strain profile predictions at displacement ductility levels of $\mu$=1.0 and $\mu$=3.0 match well with the experimental results while the predictions at displacement ductility level of $\mu$=6.0 displays scattering and is not very accurate. This discrepancy between the analytically predicted and experimentally measured results could be partially because of the locations of the given strain profiles where the experimental values are measured at the outer face of the wall while the model gives strain values at the center of wall.

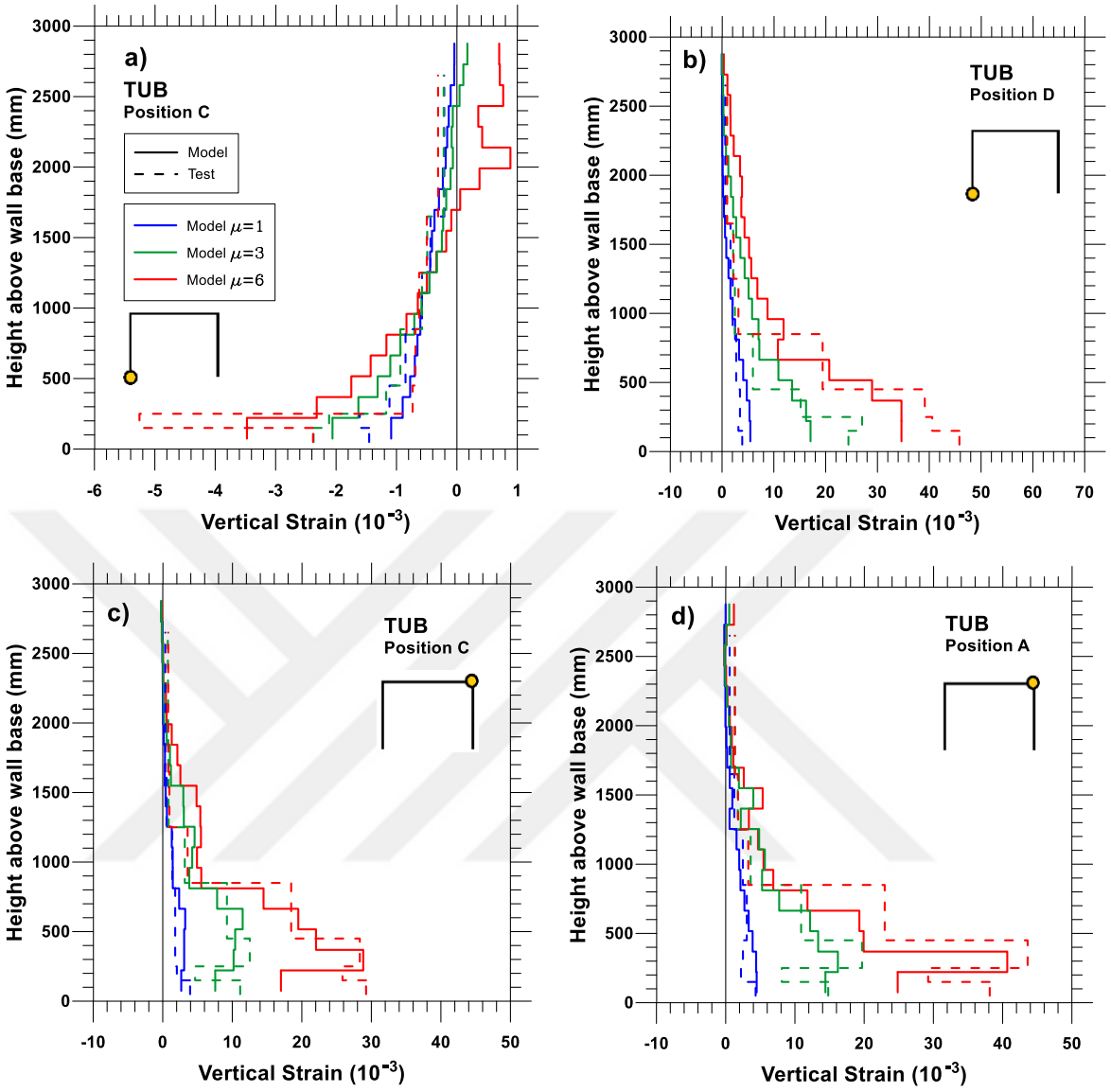


Figure 4.17. Vertical strain profiles along wall height for specimen TUB.

For specimens TUC and TUD, the vertical strain measurements were taken by using two LVDT chains at inner and outer faces of the wall at the flange ends and corners between the web and flanges. Therefore, the test data was shown for both faces of the wall specimens while the model results are obtained at the center of the wall. For specimen TUC, the experimental results and model predictions are compared at drift levels of 0.4% and 1.0% at the west flange end at loading Position E (Figure 4.18a) and Position F (Figure 4.18b), and at the east flange end at loading Position G (Figure 4.18c), and at Position H (Figure 4.18d). Loading positions can be seen in Figure 4.11f. Vertical strain profile along the wall height is simulated reasonably well even though the vertical strains above 450mm is overestimated

(Figure 4.18a). Similarly, the analytical results match reasonably well with the experimental results in Figure 4.18d. However, Figure 4.18b and Figure 4.18c indicate that the analytical results are significantly different from the test data. Especially for 1.0% drift level, the vertical strains are significantly underestimated along approximately half of the plastic hinge length region of the wall, and significantly overestimated for the rest of the plastic hinge region. For TUC, it can be concluded that the model can capture the vertical strain profile reasonably well at the locations that are in compression, while the model results are not very accurate at corner locations in tension.

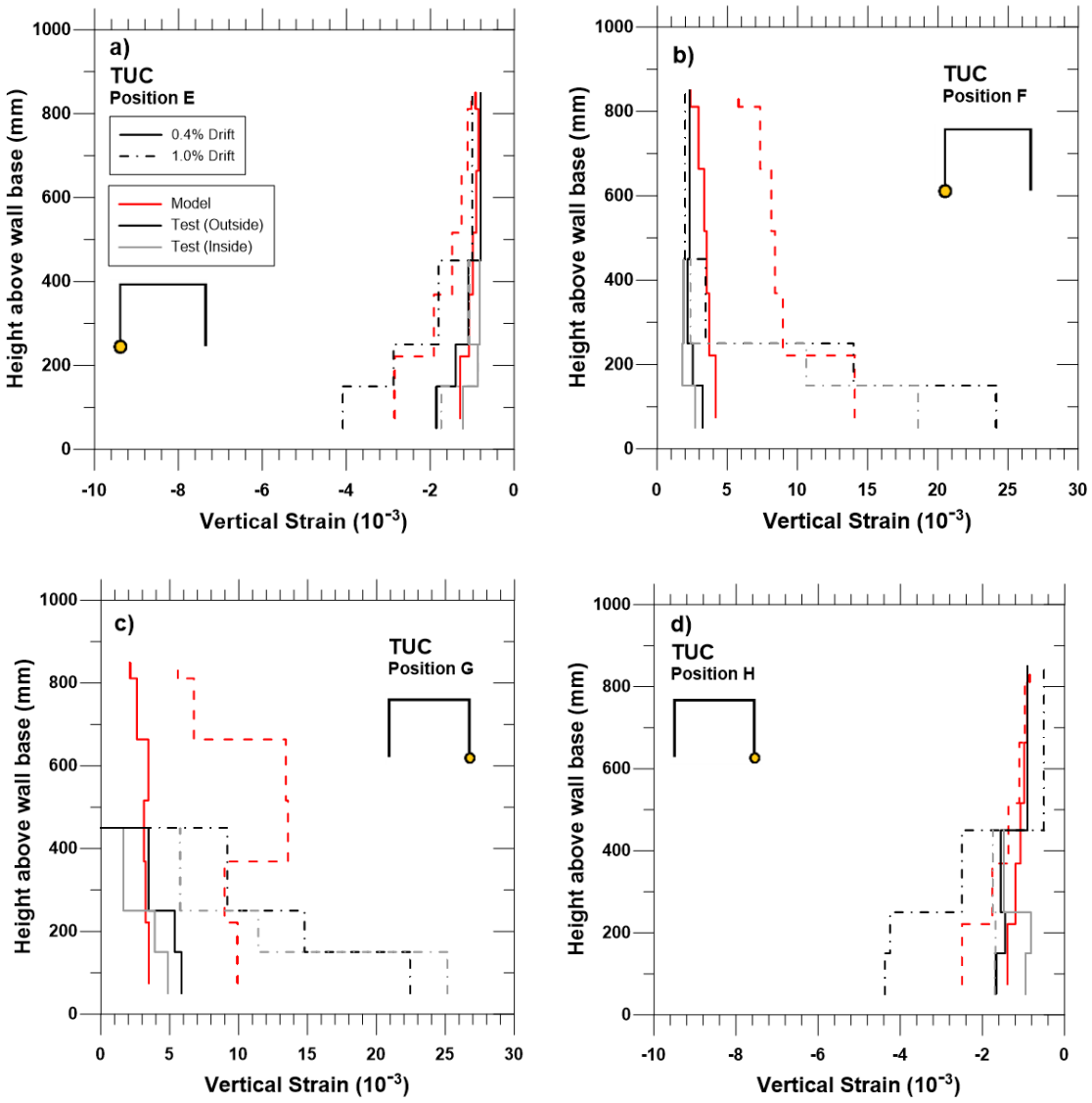


Figure 4.18. Vertical strain profiles along wall height for specimen TUC.

For specimen TUD, the model and experimental results are compared at drift levels of 0.4% and 1.0% at the west flange end at loading Position E (Figure 4.19a) and Position F (Figure 4.19b), and at the east flange end at loading Position G (Figure 4.19c), and at Position H (Figure 4.19d). Loading positions can be seen in Figure 4.12f. Similar to TUC, the model manages to provide a reasonable prediction of the trend of the vertical strain distribution along the wall height, especially when the corners where the strains are measured are in compression (Figure 4.19a, and Figure 4.19d). Again, similar to the previous case, the vertical strains along the first 450mm of the wall when the specific corner is subjected to compression are predicted better than the other cases. Figure 4.19b and Figure 4.19c show that the analytically predicted tensile strain profiles are notably different than the experimental measurements.

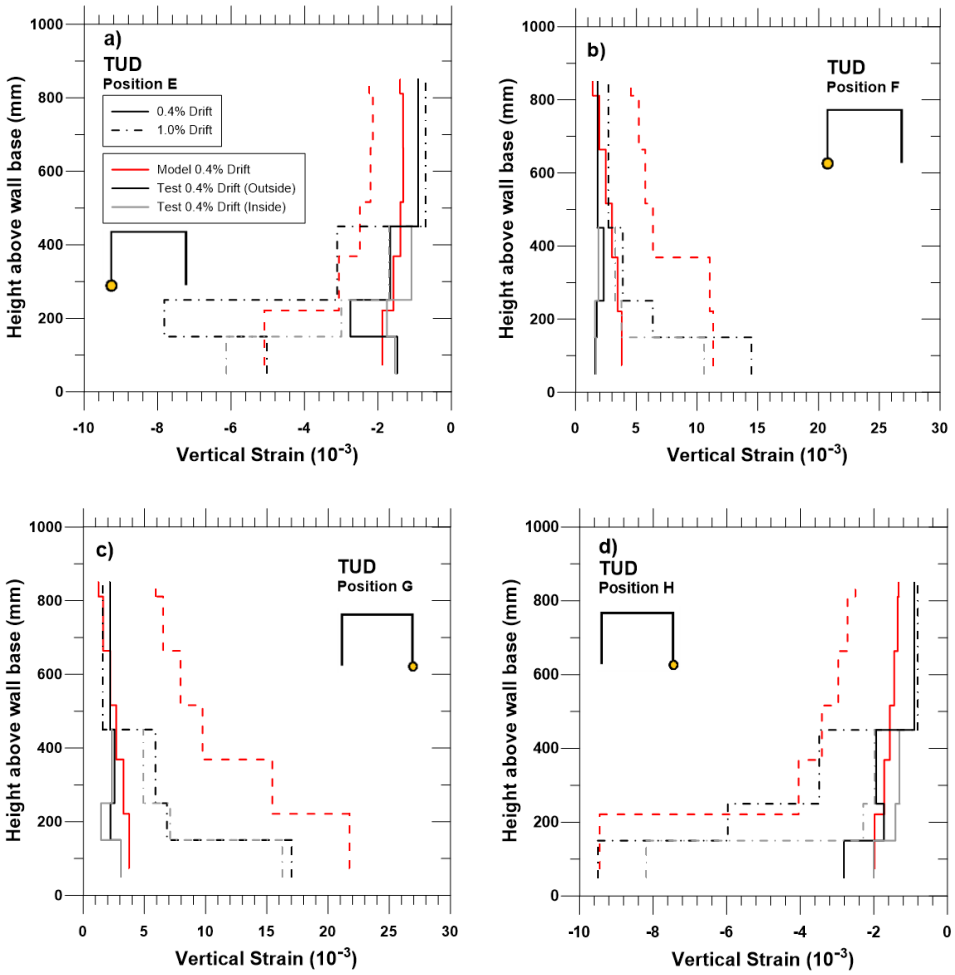


Figure 4.19. Vertical strain profiles along wall height for specimen TUD.

### 4.3.4. Vertical Strain Distribution at the Base

Figure 4.20 shows that comparison of the vertical strain distribution by the model and the experimental results at 0.6% drift level for loading cases in one direction at loading positions A (Figure 4.20a), B (Figure 4.20b), C (Figure 4.20c), D (Figure 4.20d) and at 0.4% and 1.0% drift levels for diagonal loading cases at positions E (Figure 4.20e), F (Figure 4.20f), G (Figure 4.20g), and H (Figure 4.20h) for specimen TUC. The loading positions can be seen in Figure 4.11f. The comparison in Figure 4.20 reveals that the model can reasonably capture the nonlinear vertical strain distribution at the wall base that was observed in the experimental study. The magnitude and distribution of the vertical strain are usually well predicted by the model. The largest discrepancies between the analytically predicted results and experimental results are usually for the diagonal loading cases, especially for the west flange at position E (Figure 4.20e), and the east flange under the loading in H-G directions (Figure 4.20g and Figure 4.20h) at 1.0% drift level. The discrepancy of experimental data and model predictions are due to vertical strains being calculated at the centerline by the model while the experimental results are measured at the outer face of the walls.

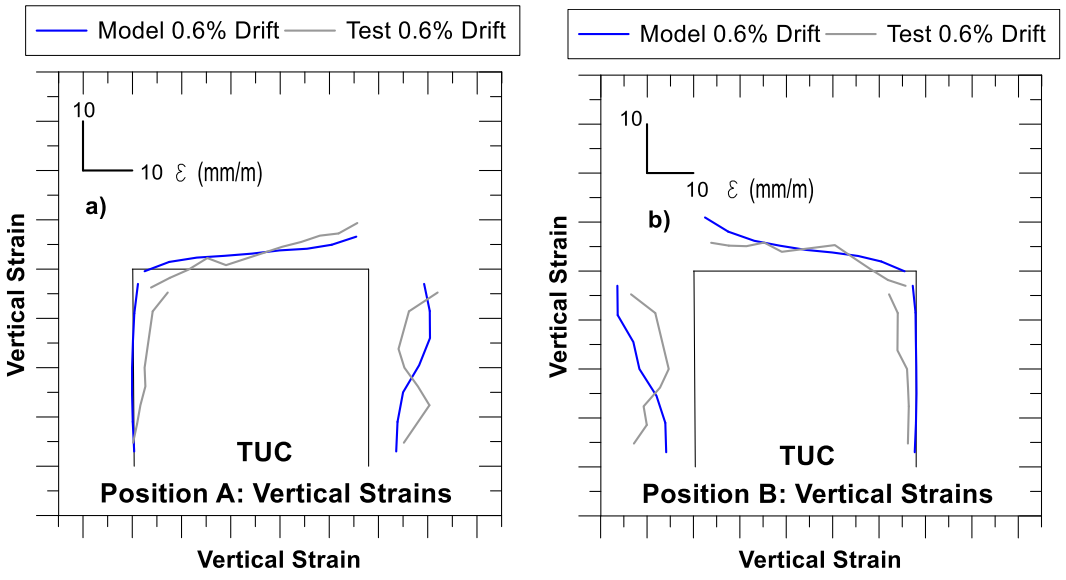


Figure 4.20. Specimen TUC: vertical strain distribution at wall base at a) position A, b) position B, c) position C, d) position D, e) position E, f) position F, g) position G, h) position H.

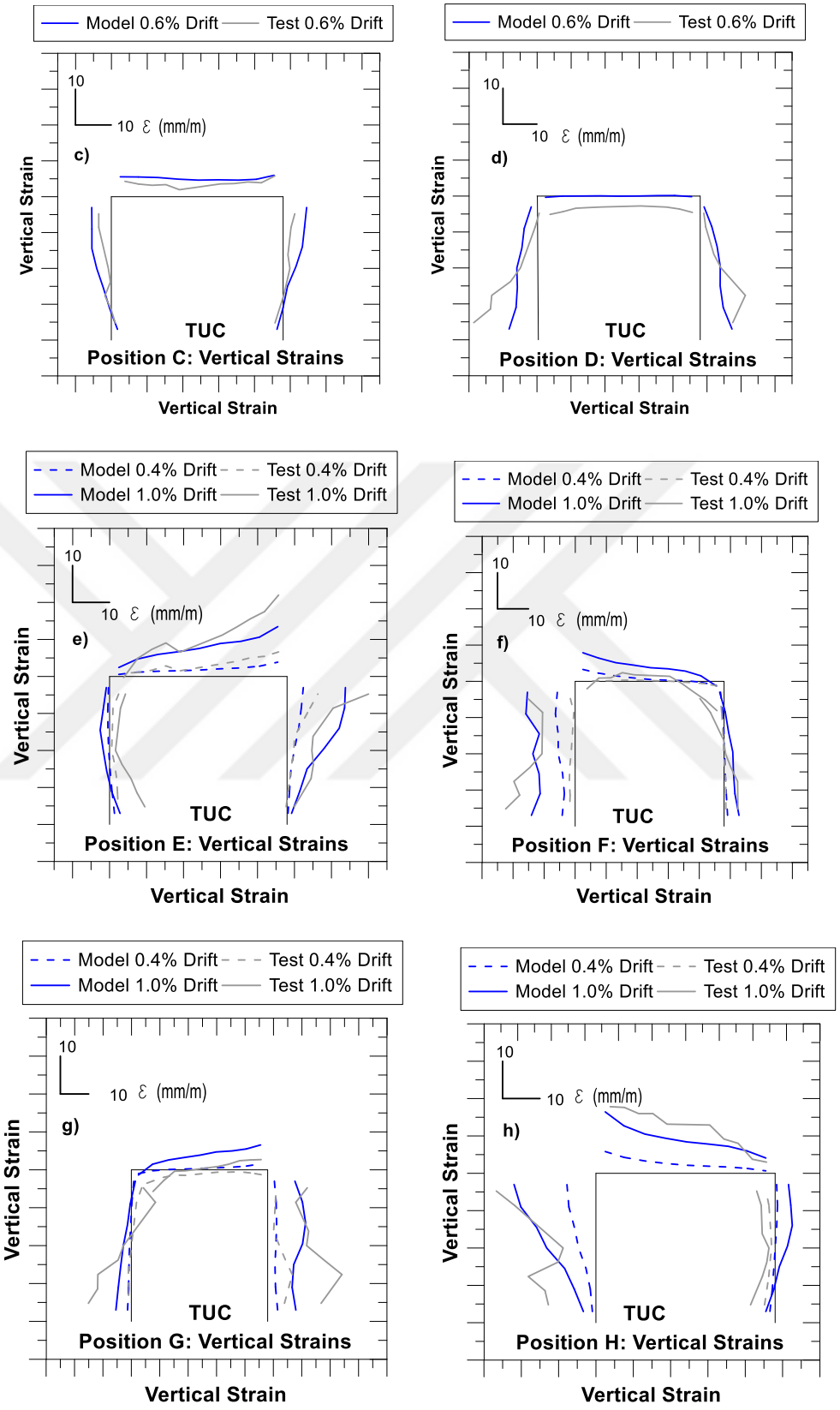


Figure 4.20. Specimen TUC: vertical strain distribution at wall base at a) position A, b) position B, c) position C, d) position D, e) position E, f) position F, g) position G, h) position H (cont.).

Figure 4.21 shows the shear stress distribution at the wall base predicted by the model for specimen TUC. The analytical shear stress results are given at 0.6% drift level for loading position A (Figure 4.21a), position B (Figure 4.21b), position C (Figure 4.21c), position D (Figure 4.21d), and at 0.4% drift and 1.0% drift levels for position E (Figure 4.21e), position F (Figure 4.21f), position G (Figure 4.21g), and position H (Figure 4.21h). These results reveal the migration of shear stresses across the wall cross-section depending on the loading position. This migration of shear stresses depending on whether the section is in tension or compression show the relationship between axial stresses which are related to vertical strains (Figure 4.20) and shear stresses (Figure 4.21).

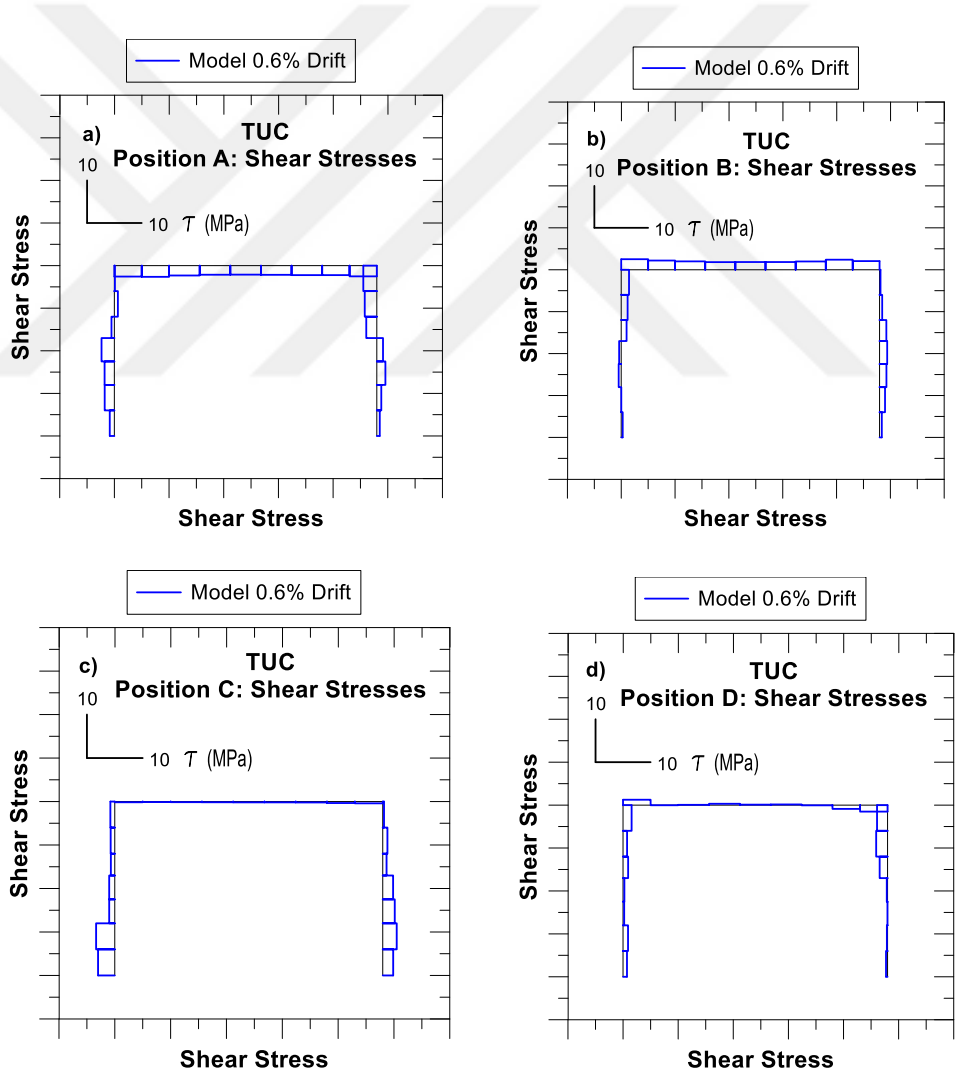


Figure 4.21. Specimen TUC: shear stress distribution at wall base at: a) position A, b) position B, c) position C, d) position D, e) position E, f) position F, g) position G, h) position H.

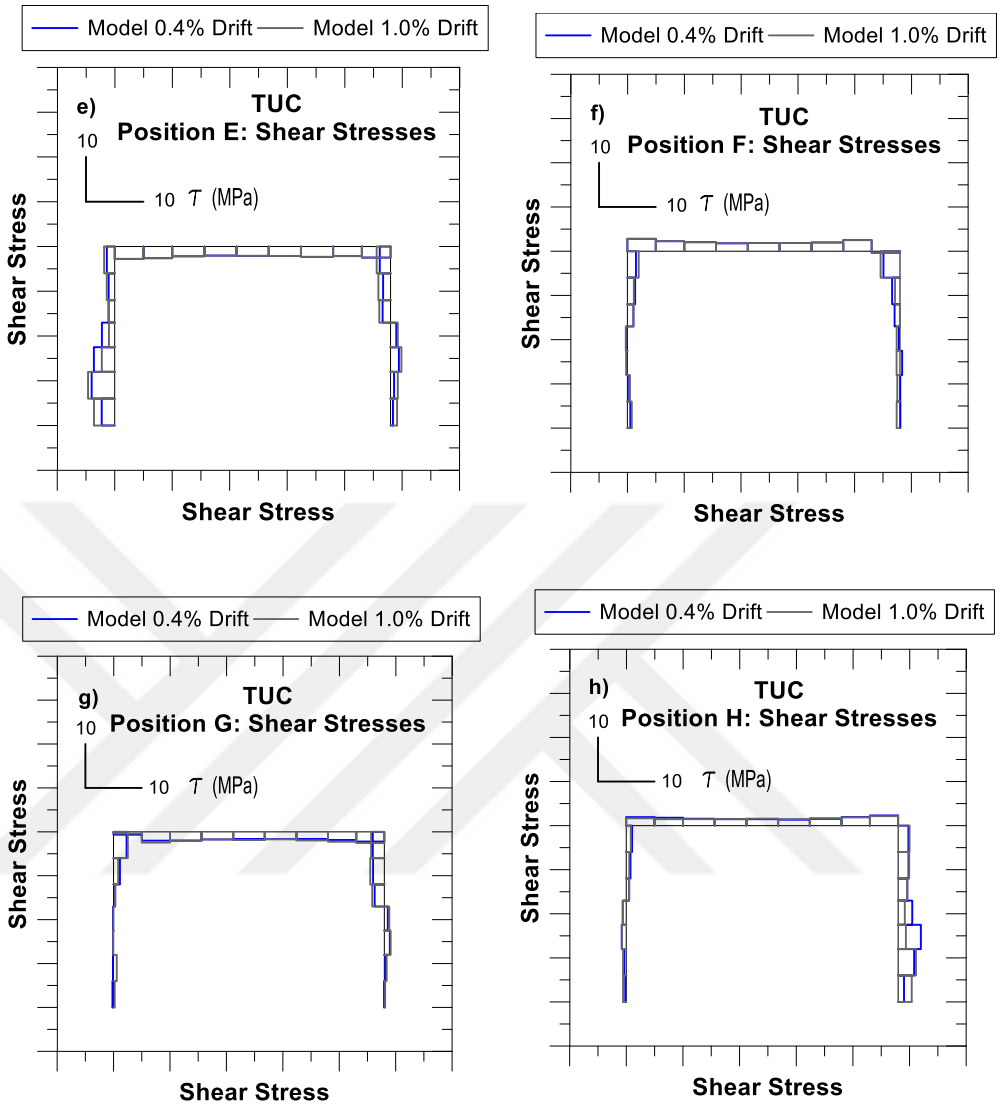


Figure 4.21. Specimen TUC: shear stress distribution at wall base at: a) position A, b) position B, c) position C, d) position D, e) position E, f) position F, g) position G, h) position H (cont.).

Vertical strain distribution at the wall base for specimen TUD are shown at positions A (Figure 4.22a), B (Figure 4.22b), C (Figure 4.22c), D (Figure 4.22d) at 0.6% drift level while distributions at positions E (Figure 4.22e), F (Figure 4.22f), G (Figure 4.22g), and H (Figure 4.22h) are given at 0.4% and 1.0% drift levels. The loading positions can be seen in Figure 4.12f. Similar to TUC, the model can capture the nonlinear vertical strain distribution at the wall base reasonably well. Overall, the magnitude and distribution of the vertical strain are usually well predicted by the model, the largest discrepancies being observed at web and

west flange at Position C (Figure 4.22c), at web at Position D (Figure 4.22d), and at wall web at Position G (Figure 4.22g) at 1.0% drift level. The reason for these discrepancies is suspected to be the same as previous case where vertical strains being calculated at the centerline by the model while the experimental results are measured at the outer face of the walls.

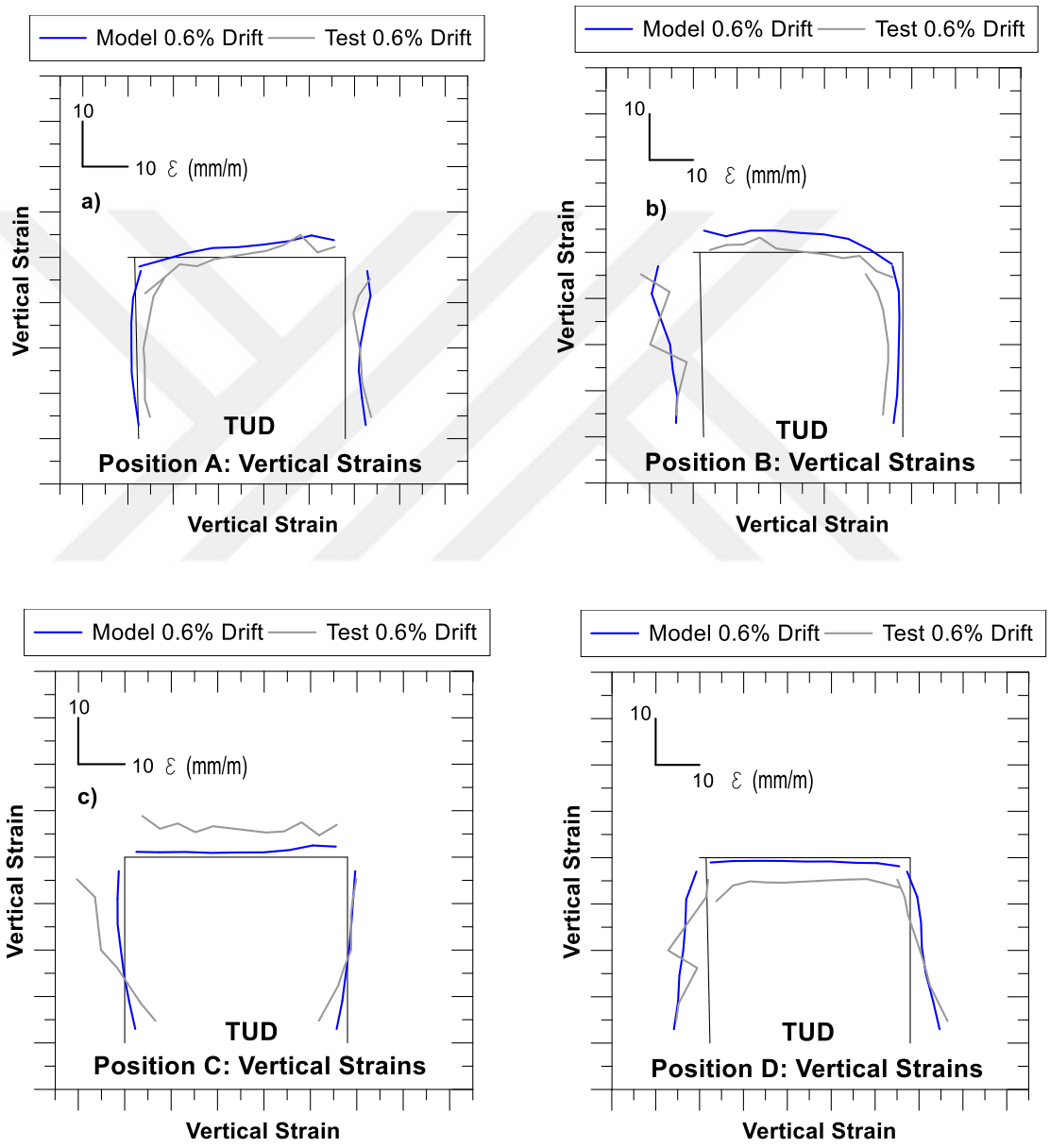


Figure 4.22. Specimen TUD: vertical strain distribution at wall base at a) position A, b) position B, c) position C, d) position D, e) position E, f) position F, g) position G, h) position H.

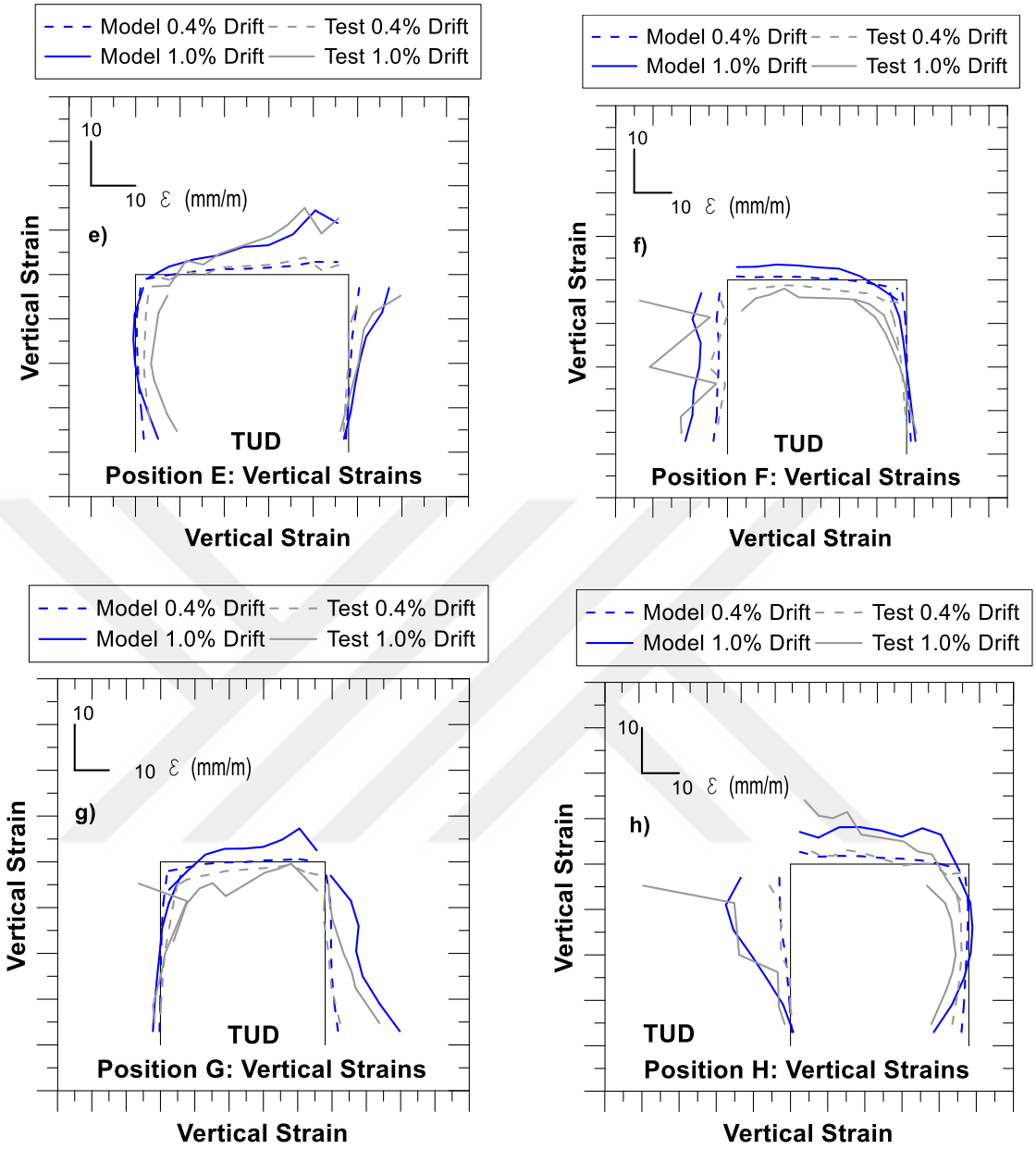


Figure 4.22. Specimen TUD: vertical strain distribution at wall base at a) position A, b) position B, c) position C, d) position D, e) position E, f) position F, g) position G, h) position H (cont.).

Figure 4.23 shows the shear stress distribution at the wall base predicted by the model for specimen TUC. The analytical shear stress results are given at 0.6% drift level for loading position A (Figure 4.23a), position B (Figure 4.23b), position C (Figure 4.23c), position D (Figure 4.23d), and at 0.4% drift and 1.0% drift levels for position E (Figure 4.23e), position F (Figure 4.23f), position G (Figure 4.23g), and position H (Figure 4.23h). Similar to specimen TUC, the results indicate that the shear stresses migrate across the wall cross-

section depending on whether the wall elements are in tension or in compression. However, since specimen TUD has a higher level of axial load, shear stresses are higher, and this makes the migration of shear stresses even more clear. Model results show that increasing levels of axial/flexural compression increases the level of shear force resisted by the wall elements which indicates the model's capability to capture the axial-shear coupling at element level which improves the internal force predictions along the wall web and wall flanges.

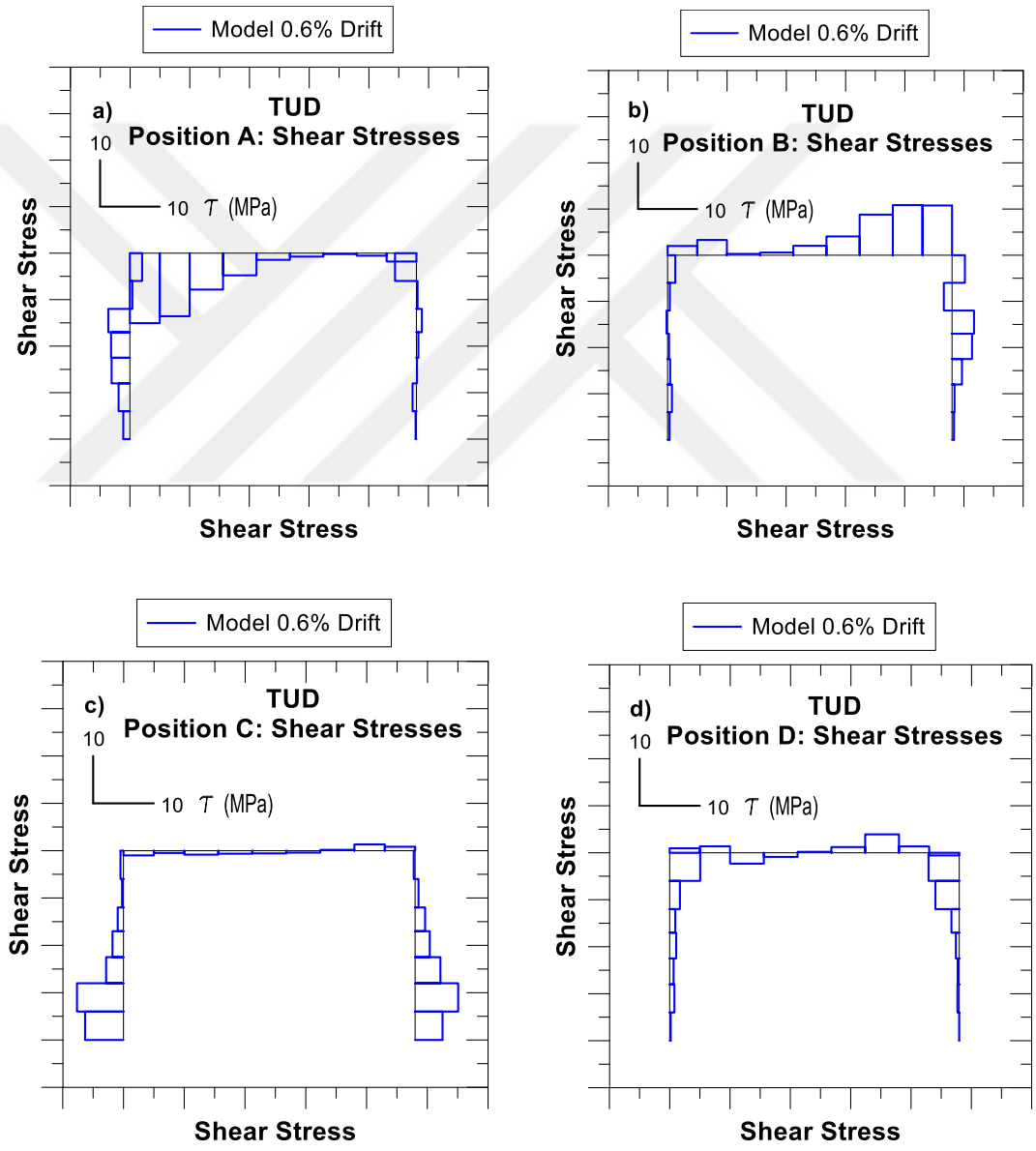


Figure 4.23. Specimen TUD: shear stress distribution at wall base at: a) position A, b) position B, c) position C, d) position D, e) position E, f) position F, g) position G, h) position H.

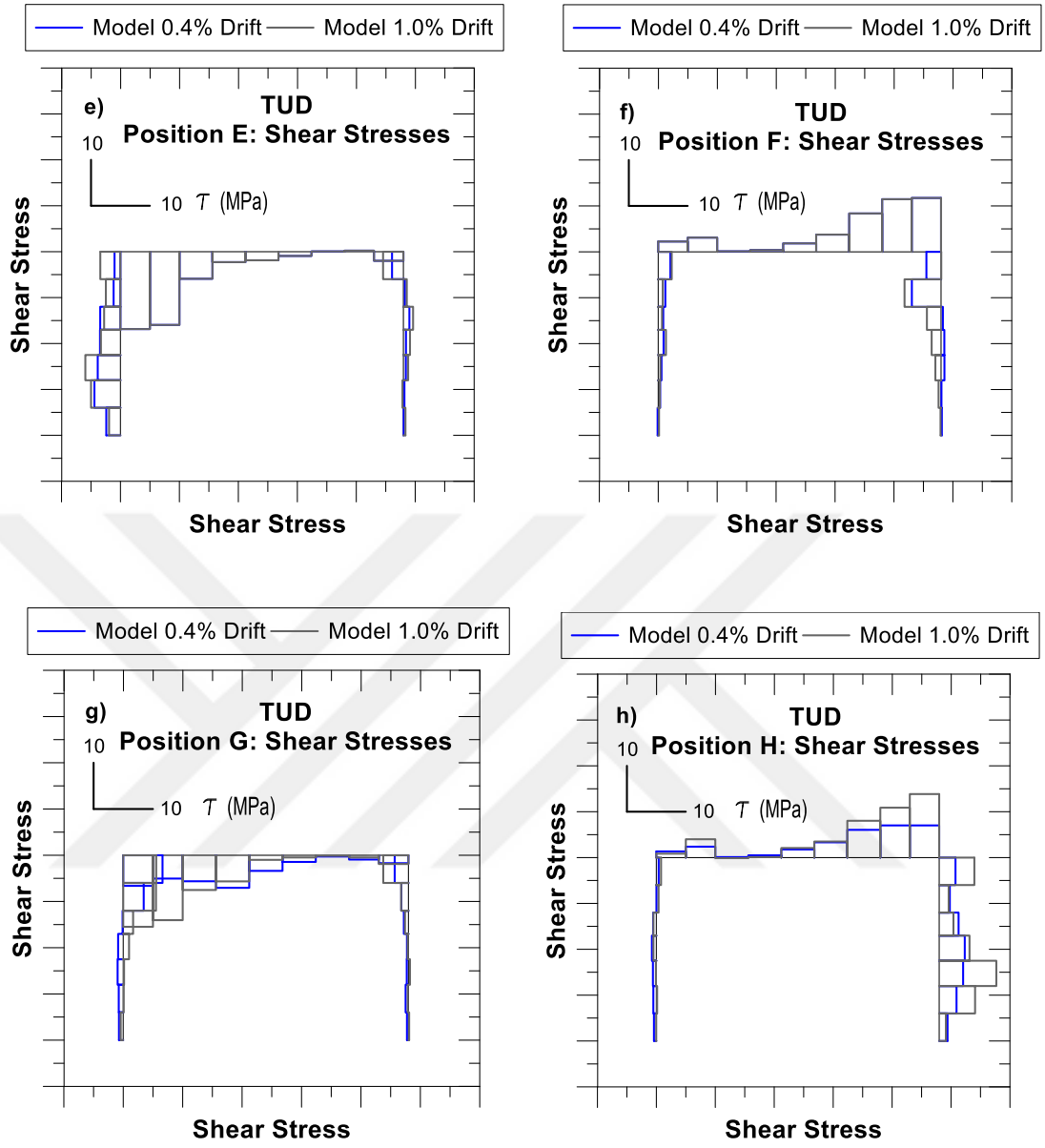


Figure 4.23. Specimen TUD: shear stress distribution at wall base at: a) position A, b) position B, c) position C, d) position D, e) position E, f) position F, g) position G, h) position H (cont.).

# 5. SUMMARY AND CONCLUSION

## 5.1. Summary

A nonlinear finite element model formulation (Fixed Strut Finite Element – FSAFE) Model) was implemented and improved for simulating the nonlinear response of nonrectangular reinforced concrete structural walls subjected to multi-directional lateral loading schemes. This model adopts a fixed crack angle approach for concrete, where the normal stresses in concrete are calculated in parallel direction to these fixed cracks. Reinforcing steel bars are subjected to uniaxial normal stresses in orthogonal reinforcement directions. Additionally, shear aggregate interlock behavior along crack surfaces and dowel effect on the reinforcing steel bars are also incorporated in the model formulation, with robust hysteretic rules and cyclic degradation parameters.

This model's capability of replicating the behavior of planar structural walls under uni-directional cyclic loading had been shown previously (Gullu and Orakcal, 2019). In this study, the model formulation was extended for nonrectangular wall cross-sections, and the displacement-controlled nonlinear analysis solution strategy was improved to allow analysis under bi-directional lateral loading conditions. As well, an improved constitutive relationship for reinforcing steel was incorporated in the model formulation, to represent buckling of longitudinal reinforcing steel bars at wall boundary region.

After extension and improvement of the model formulation and the nonlinear analysis solution strategy, the model was calibrated for and experimentally-validated against the U-shaped wall tests reported by Beyer et al. (2008) and Constantin and Beyer (2016). These U-shaped wall tests included different complex loading schemes including a 'sweep' pattern as well as diagonal loading, and the wall specimens differed in terms of wall thickness, axial load level, reinforcement distribution, and reinforcement ratios. The results provided by the model were systematically compared with the experimental data, at various global (load vs. displacement) and local (deformation) response levels. Different global (lateral load vs. top displacement) response characteristics were obtained for each direction of loading, and at

the local response level, comparisons were made in terms of shear and flexural deformation components of lateral displacement, vertical strain profiles along wall height, and vertical strain distributions at wall base, at various drift levels.

## 5.2. Conclusions

The following conclusions can be drawn from comparison of analytically-predicted experimentally-measured wall responses presented in this study:

- Despite its relatively simple 2D formulation (with no out-of-plane DOFs), the finite element modeling approach adopted in this study has demonstrated reasonable accuracy in predicting the overall behavior of nonrectangular walls subjected to biaxial cyclic lateral loading. For most cases, the model can simulate the experimentally-observed global response characteristics of the walls investigated, including their lateral load capacity, lateral stiffness, pinching behavior, plastic displacements, ductility characteristics, and hysteretic response attributes. However, the model cannot capture sudden drops in lateral strength, whether it be due to out-of-plane instability of the wall or fracture of the reinforcing bars, since these failure modes are not incorporated in the present model formulation.

- The model provides reasonable estimates for the flexural and shear deformation components of all four wall specimens investigated. Even though the results seem slightly better for TUA and TUB, the model can therefore successfully simulate shear-flexure interaction behavior, which is an important phenomenon especially for non-planar walls subjected to multi-directional lateral loading, and this is a major advantage of this model over typical fiber models which consider uncoupled shear and flexural responses.

- Model predictions for the vertical strain profiles along wall height are accurate for specimen TUB, especially along the plastic hinge region of the wall (bottom 900mm). Even though the model manages to provide reasonable vertical strain estimates along the bottom 450mm of specimens TUC and TUD, when the corner where the strains are

measured is in compression, vertical strains above 450mm elevation and vertical strains when the corner is in tension are significantly overestimated. The difference between the experimentally-measured vertical strain profiles and analytically-predicted values could be partially stemming from the fact that the model predicts the vertical strains at the mid-thickness of the wall while the experimental values are measured at the outer face of the wall section for specimen TUB and both inner and outer faces of the specimen TUC and TUD.

- Model predictions for the vertical strain distributions at wall base is reasonable. The experimentally-observed nonlinear vertical strain distribution at the wall base is well-captured by the model, in terms of both magnitudes and distribution, with occasional discrepancies which can be attributed to the vertical strains being calculated by the model at the centerline (mid-thickness), while they are measured at the outer face of the walls during the experiments. Overall, the model can successfully capture the nonlinear vertical strain distribution, due to plane sections not remaining plane, which is another significant strength of the model over typical fiber models.

- One of the specimens, specimen TUC, has experienced sudden degradation in lateral load due to out-of-plane instability of wall flange, which was not captured by the model as expected. The most important drawback of the present model is that it does not consider the out-of-plane behavior (stiffness) of the wall flanges or the wall web, and it does not incorporate out-of-plane instability failure in its formulation.

- It can be concluded from the analytically-predicted shear stress distributions at the wall base that the model can successfully simulate the interaction between the axial strains/stresses and shear stresses developing in the wall segments, which provides improved analytical predictions of the distribution of the internal shear forces resisted by the wall web and flanges of nonrectangular walls under multidirectional loading.

### 5.3. Recommendations for Future Studies

Based on the findings of this study, the following suggestions for future research can also be made:

- Although reinforcement buckling behavior is incorporated in the constitutive formulation of the present model, the model results did not reflect the reinforcing steel bar buckling failures that were observed during the experiments. This is probably because reinforcing steel is modeled using a smeared reinforcement approach within each model element, instead of using discrete rebar elements. This approach may require very fine meshing of the model elements for capture individual reinforcing bar buckling. This incapability of the model can also be improved possibly by using discrete reinforcing steel bar elements in the model formulation.

- One of the major limitations of the model is the lack of consideration of the out-of-plane behavior of the wall segments (flanges and web). Adding out-of-plane DOFs in the model formulation can improve the model performance, especially for nonplanar walls subjected to multidirectional loading. The model formulation also needs to be extended to simulate the lateral instability (out-of-plane buckling) failure of the wall segments, using an effective approach to represent geometric nonlinearity effects.

# REFERENCES

Belarbi, A. and T.T.C. Hsu, 1994, "Constitutive Laws of Concrete in Tension and Reinforcing Bars Stiffened by Concrete, *ACI Structural Journal*, Vol. 91, No. 4, pp. 465-474.

Belarbi, A. and T.T.C. Hsu, 1995, "Constitutive Laws of Softened Concrete in Biaxial Tension-Compression", ACI Structural Journal, Vol. 92, No. 5, pp. 562-573.

Beyer, K., A. Dazio, and J.N. Priestley, 2008, "Quasi-Static Cyclic Tests of Two U-Shaped Reinforced Concrete Walls", Journal of Earthquake Engineering, Vol. 12, pp. 1023-1053.

Chang, G.A. and J.B. Mander, 1994, Seismic Energy Based Fatigue Damage Analysis of Bridge Columns: Part I-Evaluation of Seismic Capacity, NCEER Technical Report No. NCEER-94-0006, National Center for Earthquake Engineering Research, State University of New York at Buffalo, NY, USA.

Clarke, M.J. and G.J. Hancock, 1990, "A Study of Incremental-Iterative Strategies for Non-Linear Analyses", International Journal for Numerical Methods in Engineering, Vol. 29, pp. 1365-1391.

Constantin, R. and K. Beyer, 2016, "Behavior of U-shaped RC walls under quasi-static cyclic diagonal loading", Engineering Structures, Vol. 106, pp. 36-52.

Dashti, F., R. Dhakal, and S. Pampanin, 2017, "Numerical Modeling of Rectangular Reinforced Concrete Structural Walls", ASCE Journal of Structural Engineering, Vol. 143, No. 6, p. 04017031.

Dhakal, R.P. and K. Maekawa, 2002a, Path-dependent cyclic stress-strain relationship of reinforcing bar including buckling", Engineering Structures, Vol. 24, pp. 1383-1396.

Dhakal, R.P. and K. Maekawa, 2002b, Reinforcement Stability and Fracture of Cover Concrete in Reinforced Concrete Members, ASCE Journal of Structural Engineering, Vol. 128, No. 10, pp. 1253-1262.

DIANA, TNO, 2011, Finite Element Analysis User's Manual-Release 9.4.4, The Netherlands.

Dodd, L.L. and J.I. Restrepo-Posada, 1995, "Model for predicting cyclic behavior of reinforcing steel", ASCE Journal of Structural Engineering, Vol. 121, pp. 433-445.

Filippou, F.C., E.G. Popov, and V.V. Bertero, 1983, Effects of Bond Deterioration on Hysteretic Behavior of Reinforced Concrete Joints, EERC Report No. UCB/EERC-83/19, University of California, Berkeley.

Gérin, M. and P. Adebar, 2009, "Simple Rational Model for Reinforced Concrete Subjected to Seismic Shear", ASCE Journal of Structural Engineering, Vol. 135, No. 7, pp. 753-761.

Gopalaratnman, V.S. and S.P. Shah, 1985, "Softening Response of Plain Concrete under Direct Tension", Journal of American Concrete Institute, Vol. 82, No. 3, pp. 310-323.

Gullu, F.M., 2019, Nonlinear Finite Element Modeling of Reinforced Concrete Structural Walls, PhD Thesis, Boğaziçi University.

Gullu, F.M. and K. Orakcal, 2019, "Nonlinear Finite Element Modeling of Reinforced Concrete Walls with Varying Aspect Ratios", Journal of Earthquake Engineering, doi:10.1080/13632469.2019.14164498.

Gullu, F.M., K. Orakcal, and K. Kolozvari, 2019, “The fixed-strut-angle finite element (FSAFE) model for reinforced concrete structural walls”, Bulletin of Earthquake Engineering, Vol. 17, pp. 6463-6489.

He, X.G., and A.H. Kwan, 2001, “Modeling Dowel Action of Reinforcement Bars for Finite Element Analysis of Structures”, Computers and Structures, Vol. 79, No. 6, pp. 595-604.

Hsu, T.T.C, 1998, “Softened Truss Model for Shear and Torsion”, ACI Structural Journal, Vol. 85, No. 6, pp. 624-635.

Hsu, T.T.C. and R.R.H. Zhu, 2002, “Softened Membrane Model for Reinforced Concrete Elements in Shear”, ACI Structural Journal, Vol. 99, No. 4, pp. 460-469.

Karsan, I.D. and J.O. Jirsa, 1969, “Behavior of Concrete under Compressive Loadings”, ASCE Journal of Structural Division, Vol. 95, No. ST12, pp. 2543-2563.

Kolozvari, K., L. Biscombe, F. Dashti, R.P. Dhakal, A. Gogus, M.F. Gullu, R.S. Henry, L.M. Massone, K. Orakcal, F. Rojas, A. Shegay, and J. Wallace, 2019, “State-of-the-art in nonlinear finite element modeling of isolated planar reinforced concrete walls”, Engineering Structures, Vol. 194, pp. 46-65.

Kolozvari, K., K. Orakcal, and J.W. Wallace, 2018, “New Opensees Models for Simulation Nonlinear Flexural and Coupled Shear-Flexural Behavior of RC Walls and Columns”, Computers and Structures, Vol. 196, pp. 246-262.

Lu, Y. and R.S. Henry, 2017, “Numerical modelling of reinforced concrete walls with minimum vertical reinforcement”, Engineering Structures, Vol. 143, pp. 330-345.

Luu, C.H., Y.L. Mo, and T.T.C. Hsu, 2017, “Development of CSMM-Based Shell Element for Reinforced Concrete Structures”, Engineering Structures, Vol. 132, pp. 778-790.

Mander, J.B., M.J.N. Priestley, and R. Park, 1988, “Theoretical Stress-Strain Model for Confined Concrete”, ASCE Journal of Structural Engineering, Vol. 114, No. 8, pp. 1804-1826.

Mansour, M.Y. and T.T.C. Hsu, 2005a, “Behavior of Reinforced Concrete Elements under Cyclic Shear. I: Experiments”, ASCE Journal of Structural Engineering, Vol. 131, No. 1, pp. 54-65.

Mansour, M.Y. and T.T.C. Hsu, 2005b, “Behavior of Reinforced Concrete Elements under Cyclic Shear. II: Theoretical Model”, ASCE Journal of Structural Engineering, Vol. 131, No. 1, pp. 44-53.

Mansour, M.Y, T.T.C. Hsu, J.Y. Lee, 2002, “Pinching Effect in Hysteretic Loops of R/C Shear Elements”, ACI Special Publications, Vol. 205, pp. 293-321.

Massone, L.M. and D. Moroder, 2009, “Buckling Modeling of Reinforcing Bars with Imperfections”, Engineering Structures, Vol. 31, No. 3, pp. 758-767.

MatLab M., 2012, The language of technical computing, The Mathworks, Inc., Massachusetts, USA.

Mau, S.T. and T.T.C. Hsu, 1986, “Shear Design and Analysis of Low-Rise Structural Walls”, ACI Structural Journal, Vol. 83, No.2, pp. 306-315.

Mau, S.T. and T.T.C. Hsu, 1987, “Shear Behavior of Reinforced Concrete Framed Wall Panels with Vertical Loads”, ACI Structural Journal, Vol. 84, No.3, pp. 228-234.

Menegotto, M. and E. Pinto, 1973, “Method of Analysis for Cyclically Loaded Reinforced Concrete Plane Frames Including Changes in Geometry and Non-Elastic Behavior of Elements under Combined Normal Force and Bending”, Proceedings, LABSE Symposium on Resistance and Ultimate Deformability of Structures Acted on by Well-Defined Repeated Loads, Lisbon, Portugal.

Mitchell, D. and M.P. Collins, 1974, “Diagonal Compression Field Theory – A Rational Model for Structural Concrete in Pure Tension”, ACI Structural Journal, Vol. 71, No. 8, pp. 396-408.

Mo, Y.L, J. Zhong, and T.T.C. Hsu, 2008, “Seismic simulation of RC wall-type structures”, Engineering Structures, Vol. 30, pp. 3167-3175.

Monti, G. and C. Nuti, 1992, “Nonlinear cyclic behavior of reinforcing bars including buckling”, ASCE Journal of Structural Engineering, Vol. 118, pp. 3268-3284.

Murray, Y.D., 2007, User Manual for LS-DYNA Concrete Material Model 159, No. FHWA-HRT-05-062, United States, Federal Highway Administration Office of Research, Development, and Technology.

Ohmori, N., T. Takahashi, N. Inoue, K. Kurihara, and S. Watanabe, 1989, “Experimental studies on nonlinear behaviors of reinforced concrete panels subjected to cyclic in-plane shear”, Proceedings of AIJ, Vol. 403, pp. 105-117.

Orakcal, K., 2004, Nonlinear Modeling and Analysis of Slender Reinforced Concrete Walls, PhD. Thesis, University of California, Los Angeles

Orakcal, K., L.M. Massone, and D. Ulugtekin, 2019, “A Hysteretic Constitutive Model for Reinforced Concrete Panel Elements”, International Journal of Concrete Structures and Materials, Vol. 13, No. 51, pp. 1-23.

Orakcal, K., D. Ulugtekin, and L.M. Massone, 2012, “Constitutive Modeling of Reinforced Concrete Panel Behavior under Cyclic Loading”, Proceedings, 15th World Conference on Earthquake Engineering, Lisbon, Portugal, No. 3573.

Palermo, D., and F.J. Vecchio, 2003, “Compression Field Modeling of Reinforced Concrete Subjected to Reversed Cyclic Loading: Formulation”, ACI Structural Journal, Vol. 100, No. 5, pp. 616-625.

Pang, D. and T.T.C. Hsu, 1995, “Behavior of Reinforced Concrete Membrane Elements in Shear”, ACI Structural Journal, Vol. 92, No. 6, pp. 665-677.

Pang, D. and T.T.C. Hsu, 1996, “Fixed Angle Softened Truss Model for Reinforced Concrete”, ACI Structural Journal, Vol. 93, No. 2, pp. 197-207.

Rojas, F., J.C. Anderson, and L.M. Massone, 2016, “A nonlinear quadrilateral layered membrane element with drilling degrees of freedom for the modeling of reinforced concrete walls”, Engineering Structures, Vol. 124, pp. 521-538.

Saatcioglu, M. and S. Razvi, 1992, “Strength and Ductility of Confined Concrete”, ASCE Journal of Structural Engineering, Vol. 118, No. 6, pp. 1560-1607.

Stevens, N.J., M. Uzumeri, and M.P. Collins, 1991, “Reinforced concrete subjected to reversed cyclic shear – Experiments and constitutive model”, ACI Structural Journal, Vol. 88, No. 2, pp. 135-146.

Suda, K., Y. Murayama, T. Ichinomiya, and H. Shimbo, 1996, “Buckling behavior of longitudinal reinforcing bars in concrete column subjected to reverse lateral loading”, Proceedings of the 11th World Conference on Earthquake Engineering, Acapulco, Mexico, No. 1753.

Tassios, T.P. and E.N. Vintzeleou, 1987, “Concrete-to-Concrete Friction”, ASCE Journal of Structural Engineering, Vol. 113, No. 4, pp. 832-849.

Thermou, G.E., V.K. Papanikolaou, and A.J. Kappos, 2014, “Flexural Behavior of Reinforced Concrete Jacketed Columns under Reversed Cyclic Loading”, Engineering Structures, Vol. 76, pp. 270-282.

Vassilopoulou, I., and T.P. Tassios, 2003, “Shear Transfer Capacity along a RC Crack under Cyclic Sliding”, Proceedings of fib Symposium: Concrete Structures in Seismic Regions, Athens, Greece.

Vecchio, F.J., 2000, “Disturbed Stress Field Model for Reinforced Concrete: Formulation”, ASCE Journal of Structural Engineering, Vol. 126, No. 9, pp. 1070-1077.

Vecchio, F.J. and M.P. Collins, 1993, “Compression Response of Cracked Reinforced Concrete”, ASCE Journal of Structural Engineering, Vol. 119, No. 12, pp. 3590-3610.

Vecchio, F.J. and M.P. Collins, 1986, “The Modified Compression-Field Theory for Reinforced Concrete Elements Subjected to Shear”, ACI Structural Journal, Vol. 83, No. 2, pp. 219-231.

Vintzeleou, E.N. and T.P. Tassios, 1986, “Mathematical Models for Dowel Action under Monotonic and Cyclic Conditions”, Magazine of Concrete Research, Vol. 38, No. 134, pp. 13-22.

Wong, P.S., F.J. Vecchio, and H. Trommels, VecTor2 & FormWorks user’s manual (2 ed), Toronto, Canada.

Yankelevsky, D.Z. and H.W. Reinhardt, 1987, “Response of Plain Concrete to Cyclic Tension”, ACI Material Journal, Vol. 84, No. 5, pp. 365-373.

# APPENDIX A: COPYRIGHT PERMISSIONS FOR THE FIGURES

This Agreement between Ms. Nihan Bilgin ("You") and Elsevier ("Elsevier") consists of your license details and the terms and conditions provided by Elsevier and Copyright Clearance Center.

| | |
|---|---|
| License Number | 5101741051467 |
| License date | Jul 04, 2021 |
| Licensed Content Publisher | Elsevier |
| Licensed Content Publication | Engineering Structures |
| Licensed Content Title | Seismic simulation of RC wall-type structures |
| Licensed Content Author | Y.L. Mo,Jianxia Zhong,Thomas T.C. Hsu |
| Licensed Content Date | Nov 1, 2008 |
| Licensed Content Volume | 30 |
| Licensed Content Issue | 11 |
| Licensed Content Pages | 9 |
| Start Page | 3167 |
| End Page | 3175 |
| Type of Use | reuse in a thesis/dissertation |
| Portion | figures/tables/illustrations |
| Number of figures/tables/illustrations | 1 |
| Format | both print and electronic |
| Are you the author of this Elsevier article? | No |
| Will you be translating? | No |
| Title | Finite Element Modeling of Nonrectangular Reinforced Concrete Structural Walls |
| Institution name | Bogazici University |
| Expected presentation date | Jul 2021 |
| Portions | Fig. 5 |
| Requestor Location | |
| Publisher Tax ID | GB 494 6272 12 |
| Total | **0.00 USD** |

Figure A.1. Copyrights of Figure 1.1.

This Agreement between Ms. Nihan Bilgin ("You") and Elsevier ("Elsevier") consists of your license details and the terms and conditions provided by Elsevier and Copyright Clearance Center.

| | |
|---|---|
| License Number | 5101741229997 |
| License date | Jul 04, 2021 |
| Licensed Content Publisher | Elsevier |
| Licensed Content Publication | Engineering Structures |
| Licensed Content Title | Development of CSMM-based shell element for reinforced concrete structures |
| Licensed Content Author | C.H. Luu,Y.L. Mo,Thomas T.C. Hsu |
| Licensed Content Date | Feb 1, 2017 |
| Licensed Content Volume | 132 |
| Licensed Content Issue | n/a |
| Licensed Content Pages | 13 |
| Start Page | 778 |
| End Page | 790 |
| Type of Use | reuse in a thesis/dissertation |
| Portion | figures/tables/illustrations |
| Number of figures/tables/illustrations | 1 |
| Format | both print and electronic |
| Are you the author of this Elsevier article? | No |
| Will you be translating? | No |
| Title | Finite Element Modeling of Nonrectangular Reinforced Concrete Structural Walls |
| Institution name | Bogazici University |
| Expected presentation date | Jul 2021 |
| Portions | Fig. 1 |
| Requestor Location | |
| Publisher Tax ID | GB 494 6272 12 |
| Total | **0.00 USD** |

Figure A.2. Copyrights of Figure 1.2.

This Agreement between Ms. Nihan Bilgin ("You") and Elsevier ("Elsevier") consists of your license details and the terms and conditions provided by Elsevier and Copyright Clearance Center.

| | |
|---|---|
| License Number | 5101741421933 |
| License date | Jul 04, 2021 |
| Licensed Content Publisher | Elsevier |
| Licensed Content Publication | Engineering Structures |
| Licensed Content Title | A nonlinear quadrilateral layered membrane element with drilling degrees of freedom for the modeling of reinforced concrete walls |
| Licensed Content Author | F. Rojas,J.C. Anderson,L.M. Massone |
| Licensed Content Date | Oct 1, 2016 |
| Licensed Content Volume | 124 |
| Licensed Content Issue | n/a |
| Licensed Content Pages | 18 |
| Start Page | 521 |
| End Page | 538 |
| Type of Use | reuse in a thesis/dissertation |
| Portion | figures/tables/illustrations |
| Number of figures/tables/illustrations | 2 |
| Format | both print and electronic |
| Are you the author of this Elsevier article? | No |
| Will you be translating? | No |
| Title | Finite Element Modeling of Nonrectangular Reinforced Concrete Structural Walls |
| Institution name | Bogazici University |
| Expected presentation date | Jul 2021 |
| Portions | Fig. 1, Fig. 2 |
| Requestor Location | |
| Publisher Tax ID | GB 494 6272 12 |
| Total | **0.00 USD** |

Figure A.3. Copyrights of Figure 1.3.

This Agreement between Ms. Nihan Bilgin ("You") and Elsevier ("Elsevier") consists of your license details and the terms and conditions provided by Elsevier and Copyright Clearance Center.

| | |
|---|---|
| License Number | 5101750067363 |
| License date | Jul 04, 2021 |
| Licensed Content Publisher | Elsevier |
| Licensed Content Publication | Engineering Structures |
| Licensed Content Title | Numerical modelling of reinforced concrete walls with minimum vertical reinforcement |
| Licensed Content Author | Yiqiu Lu,Richard S. Henry |
| Licensed Content Date | Jul 15, 2017 |
| Licensed Content Volume | 143 |
| Licensed Content Issue | n/a |
| Licensed Content Pages | 16 |
| Start Page | 330 |
| End Page | 345 |
| Type of Use | reuse in a thesis/dissertation |
| Portion | figures/tables/illustrations |
| Number of figures/tables/illustrations | 1 |
| Format | both print and electronic |
| Are you the author of this Elsevier article? | No |
| Will you be translating? | No |
| Title | Finite Element Modeling of Nonrectangular Reinforced Concrete Structural Walls |
| Institution name | Bogazici University |
| Expected presentation date | Jul 2021 |
| Portions | Fig. 1 |
| Requestor Location | |
| Publisher Tax ID | GB 494 6272 12 |
| Total | **0.00 USD** |

Figure A.4. Copyrights of Figure 1.4.

This Agreement between Ms. Nihan Bilgin ("You") and Elsevier ("Elsevier") consists of your license details and the terms and conditions provided by Elsevier and Copyright Clearance Center.

| | |
|---|---|
| License Number | 5101531385504 |
| License date | Jul 03, 2021 |
| Licensed Content Publisher | Elsevier |
| Licensed Content Publication | Engineering Structures |
| Licensed Content Title | State-of-the-art in nonlinear finite element modeling of isolated planar reinforced concrete walls |
| Licensed Content Author | Kristijan Kolozvari,Lauren Biscombe,Farhad Dashti,Rajesh P. Dhakal,Aysegul Gogus,M. Fethi Gullu,Richard S. Henry,Leonardo M. Massone,Kutay Orakcal,Fabian Rojas,Alex Shegay,John Wallace |
| Licensed Content Date | Sep 1, 2019 |
| Licensed Content Volume | 194 |
| Licensed Content Issue | n/a |
| Licensed Content Pages | 20 |
| Start Page | 46 |
| End Page | 65 |
| Type of Use | reuse in a thesis/dissertation |
| Portion | figures/tables/illustrations |
| Number of figures/tables/illustrations | 1 |
| Format | both print and electronic |
| Are you the author of this Elsevier article? | No |
| Will you be translating? | No |
| Title | Finite Element Modeling of Nonrectangular Reinforced Concrete Structural Walls |
| Institution name | Bogazici University |
| Expected presentation date | Jul 2021 |
| Portions | Fig. 2 |
| Requestor Location | |
| Publisher Tax ID | GB 494 6272 12 |
| Total | **0.00 USD** |

Figure A.5. Copyrights of Figure 1.5.




Figure A.6. Copyrights of Figure 2.1, Figure 2.2, Figure 2.3.

To Boğaziçi University Institute of Graduate Studies in Science and Engineering,

I grant permission for the reuse of Figure 4.1, Figure 4.13, Figure 4.15, Figure 4.21, and Figure 4.23 from my PhD dissertation (Orakcal, 2004) in Nihan Bilgin's master's thesis.

Figure A.7. Copyrights of Figure 2.4, Figure 2.5, Figure 2.6, Figure 2.9, and Figure 2.10.

To Boğaziçi University Institute of Graduate Studies in Science and Engineering.

I grant permission for the reuse of Figure 2.2, Figure 2.3, Figure 4.1, and Figure 4.2 from my PhD Thesis (Gullu, 2019) in Nihan Bilgin's master's thesis.

Figure A.8. Copyrights of Figure 2.11, Figure 2.12, Figure 3.1, and Figure 3.2.

## How may I reuse Taylor & Francis content?

A type of use describes what you may wish to do with copyrighted content and what the publisher permits. Taylor & Francis offers the following types of use either directly through RightsLink or after approval by Taylor & Francis. For Taylor & Francis terms and conditions regarding each of these types of use, please reference the Taylor & Francis terms and conditions offered during the order process. [NOTE: Any form of republication must be completed within six (6) months from the date of the license (although copies prepared before then may be distributed thereafter); and any electronic posting is limited to a period of one year.]

RightsLink can process your permission requests to reuse Taylor & Francis content in:

- **Reuse in a Dissertation/Thesis**: A dissertation/thesis license authorizes an advanced degree candidate to reproduce portions of the content in his/her doctoral thesis or dissertation. For full article/chapter content, please contact publisher directly to obtain approval. If your license is for use in a thesis or dissertation, your thesis may be submitted to your institution in either print or electronic format. If your thesis, or dissertation, is to be published commercially, then you must reapply for permission. If you are an author of the article/chapter wishing to reuse the content in full please refer to your Author Agreement for an explanation of your retained author rights.

https://s100.copyright.com/help/rightslinkhelppages/Frequently_Asked_Questions_tandf.htm

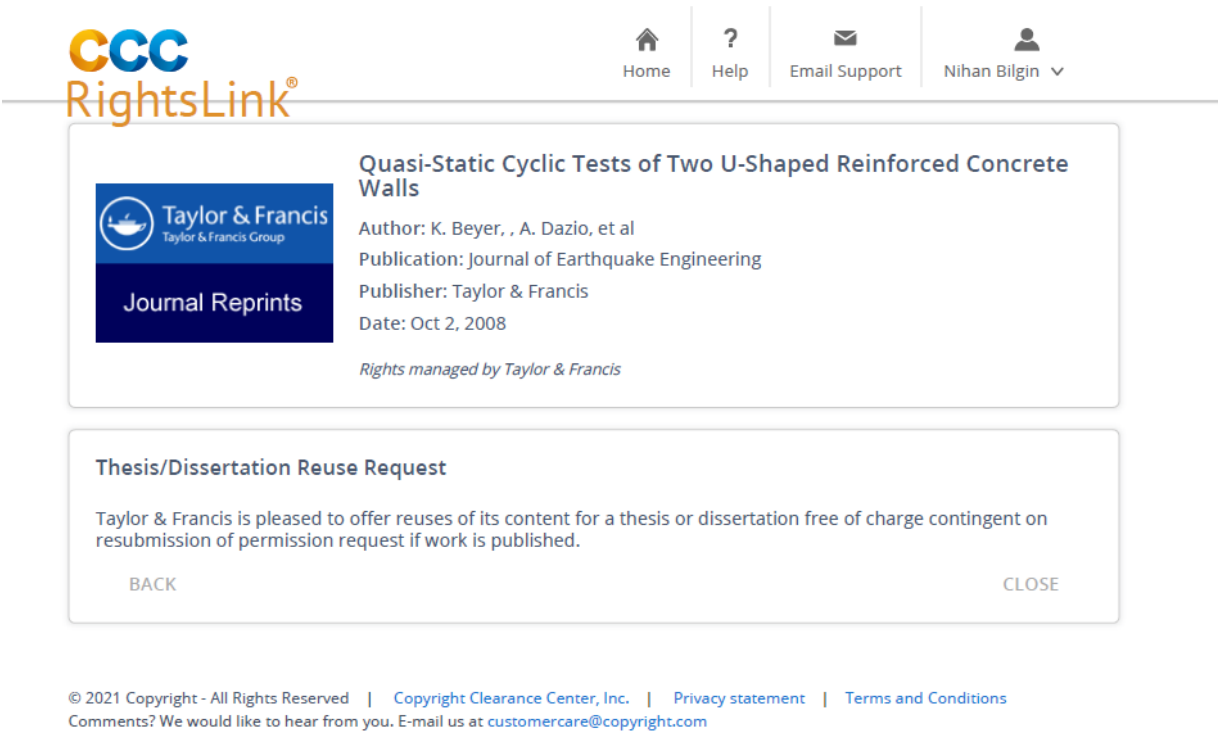


Figure A.9. Copyrights of Figure 4.1, Figure 4.2, Figure 4.3, and Figure 4.4.

This Agreement between Ms. Nihan Bilgin ("You") and Elsevier ("Elsevier") consists of your license details and the terms and conditions provided by Elsevier and Copyright Clearance Center.

| | |
|---|---|
| License Number | 5101750368360 |
| License date | Jul 04, 2021 |
| Licensed Content Publisher | Elsevier |
| Licensed Content Publication | Engineering Structures |
| Licensed Content Title | Behaviour of U-shaped RC walls under quasi-static cyclic diagonal loading |
| Licensed Content Author | Raluca Constantin,Katrin Beyer |
| Licensed Content Date | Jan 1, 2016 |
| Licensed Content Volume | 106 |
| Licensed Content Issue | n/a |
| Licensed Content Pages | 17 |
| Start Page | 36 |
| End Page | 52 |
| Type of Use | reuse in a thesis/dissertation |
| Portion | figures/tables/illustrations |
| Number of figures/tables/illustrations | 3 |
| Format | both print and electronic |
| Are you the author of this Elsevier article? | No |
| Will you be translating? | No |
| Title | Finite Element Modeling of Nonrectangular Reinforced Concrete Structural Walls |
| Institution name | Bogazici University |
| Expected presentation date | Jul 2021 |
| Portions | Fig. 1, Fig. 3, Fig. 4 |
| Requestor Location | |
| Publisher Tax ID | GB 494 6272 12 |
| Total | **0.00 USD** |

Figure A.10. Copyrights of Figure 4.5, Figure 4.6, and Figure 4.7.